Astronomy & Astrophysics manuscript no. ATLASGAL_TOP100_Tkin
September 10, 2018

ATLASGAL-selected massive clumps in the inner Galaxy:

VI. Kinetic temperature and spatial density measured with formaldehyde

X. D. Tang[1,2,3], C. Henkel[1,4], F. Wyrowski[1], A. Giannetti[1,5], K. M. Menten[1], T. Csengeri[1], S. Leurini[1,6], J. S. Urquhart[1,7], C. König[1], R. Güsten[1], Y. X. Lin[1], X. W. Zheng[8], J. Esimbek[2,3], and J. J. Zhou[2,3]

[1] Max-Planck-Institut für Radioastronomie, Auf dem Hügel 69, 53121 Bonn, Germany
e-mail: xdtang@mpifr-bonn.mpg.de
[2] Xinjiang Astronomical Observatory, Chinese Academy of Sciences, 830011 Urumqi, PR China
[3] Key Laboratory of Radio Astronomy, Chinese Academy of Sciences, 830011 Urumqi, PR China
[4] Astronomy Department, King Abdulaziz University, PO Box 80203, 21589 Jeddah, Saudi Arabia
[5] INAF–Istituto di Radioastronomia & Italian ALMA Regional Centre, Via P. Gobetti 101, I–40129 Bologna, Italy
[6] INAF–Osservatorio Astronomico di Cagliari, Via della Scienza 5, I–09047, Selargius (CA), Italy
[7] School of Physical Sciences, University of Kent, Ingram Building, Canterbury, Kent CT2 7NH, UK
[8] School of Astronomy and Space Science, Nanjing University, 210093 Nanjing, PR China

September 10, 2018

ABSTRACT

Formaldehyde (H_2CO) is a reliable tracer to accurately measure the physical parameters of dense gas in star forming regions. We aim to directly determine the kinetic temperature and spatial density with formaldehyde for the ∼100 brightest ATLASGAL-selected clumps (the TOP100 sample) at 870 μm representing various evolutionary stages of high-mass star formation. Ten transitions (J = 3–2 and 4–3) of ortho- and para-H_2CO near 211, 218, 225, and 291 GHz were observed with the Atacama Pathfinder EXperiment (APEX) 12 m telescope. Using non-LTE models with RADEX, we derive the gas kinetic temperature and spatial density using the measured para-H_2CO 3_{21}–2_{20}/3_{03}–2_{02}, 4_{22}–3_{21}/4_{04}–3_{03}, and 4_{04}–3_{03}/3_{03}–2_{02} ratios. The gas kinetic temperatures derived from the para-H_2CO 3_{21}–2_{20}/3_{03}–2_{02} and 4_{22}–3_{21}/4_{04}–3_{03} line ratios are high, ranging from 43 to >300 K with an unweighted average of 91 ± 4 K. Deduced $T_{\rm kin}$ values from the J = 3–2 and 4–3 transitions are similar. Spatial densities of the gas derived from the para-H_2CO 4_{04}–3_{03}/3_{03}–2_{02} line ratios yield 0.6–8.3 × 10^6 cm^{-3} with an unweighted average of 1.5 (±0.1) × 10^6 cm^{-3}. A comparison of kinetic temperatures derived from para-H_2CO, NH_3, and the dust emission indicates that para-H_2CO traces a distinctly higher temperature than the NH_3 (2,2)/(1,1) transitions and the dust, tracing heated gas more directly associated with the star formation process. The H_2CO linewidths are found to be correlated with bolometric luminosity and increase with the evolutionary stage of the clumps, which suggests that higher luminosities tend to be associated with a more turbulent molecular medium. It seems that the spatial densities measured with H_2CO do not vary significantly with the evolutionary stage of the clumps. However, averaged gas kinetic temperatures derived from H_2CO increase with time through the evolution of the clumps. The high temperature of the gas traced by H_2CO may be mainly caused by radiation from embedded young massive stars and the interaction of outflows with the ambient medium. For $L_{\rm bol}/M_{\rm clump} \gtrsim 10\,L_\odot/M_\odot$, we find a rough correlation between gas kinetic temperature and this ratio, which is indicative of the evolutionary stage of the individual clumps. The strong relationship between H_2CO line luminosities and clump masses is apparently linear during the late evolutionary stages of the clumps, indicating that $L_{\rm H_2CO}$ does reliably trace the mass of warm dense molecular gas. In our massive clumps H_2CO line luminosities are approximately linearly correlated with bolometric luminosities over about four orders of magnitude in $L_{\rm bol}$, which suggests that the mass of dense molecular gas traced by the H_2CO line luminosity is well correlated with star formation.

Key words. Stars: formation – Stars: massive – ISM: clouds – ISM: molecules – ISM: abundances – radio lines: ISM

1. Introduction

In the Galactic disk, star formation appears to occur only in dense regions (spatial density $n(H_2) \gtrsim 10^4$ cm^{-3}) composed of molecular gas (Lada et al. 2010; Ginsburg et al. 2015). High mass stars form in massive clumps with typical size of order ∼1 pc (e.g., Dunham et al. 2010, 2011; Rosolowsky et al. 2010; Urquhart et al. 2014; He et al. 2015; Wienen et al. 2015; König et al. 2017; Yuan et al. 2017). High-mass stars influence the surrounding environment and subsequent star formation through their feedback such as outflows, winds, as well as UV radiation. However, the details of the high mass star formation process and how their feedback may affect the initial conditions of high mass stars in their formation process are still far from being clear and require, as a basis, the precise determination of kinetic temperature and density.

The Atacama Pathfinder EXperiment (APEX) Telescope Large Area Survey of the GALaxy (ATLASGAL) (Schuller et al. 2009), presenting observations in a Galactic longitude and latitude range of ±60° and ±1.5°, respectively, introduces a global view on star formation at 870 μm and identifies ∼10,000 massive clumps in various stages of evolution undergoing high mass star formation in the inner Galaxy (Contreras et al. 2013; Urquhart et al. 2014, 2017; Csengeri et al. 2014). The most fundamental physical parameters, kinetic temperature and spatial density of the clumps, affect chemistry, star formation, and could also impact the stellar initial mass function. Accurate measurements of these physical

parameters are indispensable for a general understanding of the physical processes involved in these massive star-forming clumps.

Formaldehyde (H_2CO) is a ubiquitous molecule in interstellar clouds (Downes et al. 1980; Bieging et al. 1982; Henkel et al. 1991; Zylka et al. 1992; Mangum et al. 2008, 2013a; Ao et al. 2013; Tang et al. 2013; Ginsburg et al. 2015, 2016, 2017; Guo et al. 2016). As a slightly asymmetric rotor molecule, H_2CO exhibits a large number of millimeter and submillimeter transitions. It is a reliable tracer of physical conditions such as temperature and density (Henkel et al. 1980, 1983; Mangum & Wootten 1993; Mühle et al. 2007; Ginsburg et al. 2011, 2015, 2016; Ao et al. 2013). Since the relative populations of the K_a ladders of H_2CO are predominantly governed by collisions, ratios of H_2CO line fluxes involving different K_a ladders are good tracers of the kinetic temperature, such as para-H_2CO $J_{K_aK_c} = 3_{22}$–$2_{21}/3_{03}$–2_{02}, 4_{23}–$3_{22}/4_{04}$–3_{03}, and 5_{23}–$4_{22}/5_{05}$–4_{04} (Mangum & Wootten 1993). Once the kinetic temperature is known, line ratios involving the same K_a ladders yield estimates of the spatial density of the gas, such as $J_{K_aK_c} = 4_{04}$–$3_{03}/3_{03}$–2_{02}, 5_{05}–$4_{04}/3_{03}$–2_{02}, and 5_{24}–$4_{23}/3_{22}$–2_{21} (Mangum & Wootten 1993; Mühle et al. 2007; Immer et al. 2016). Transitions connecting the same rotational levels (e.g., $J = 3$–2 or 4–3) and belonging to either the para- or ortho-H_2CO subspecies, but being part of different K_a ladders (e.g., $K_a = 0$, 2) are particularly useful. They can be measured simultaneously with the same receiver system and their relative strengths (para-H_2CO 3_{22}–$2_{21}/3_{03}$–2_{02}, 3_{21}–$2_{20}/3_{03}$–2_{02}, 4_{23}–$3_{22}/4_{04}$–3_{03}, and 4_{22}–$3_{21}/4_{04}$–3_{03} provide sensitive thermometry. Para-H_2CO is therefore possibly the best of the very few molecular tracers that are available for such an analysis of the dense molecular gas. H_2CO line ratios have been used to measure physical parameters in our Galactic center clouds (Qin et al. 2008; Ao et al. 2013; Johnston et al. 2014; Ginsburg et al. 2016; Immer et al. 2016; Lu et al. 2017), star formation regions (Mangum & Wootten 1993; Hurt et al. 1996; Mangum et al. 1999; Mitchell et al. 2001; Watanabe & Mitchell 2008; Nagy et al. 2012; Lindberg et al. 2015; Tang et al. 2017a,c), as well as in external galaxies (Mühle et al. 2007; Tang et al. 2017b).

In this work, we aim to directly measure the kinetic temperature and spatial density toward massive star-forming clumps selected from the ATLASGAL survey making use of the rotational transitions of H_2CO ($J = 3$–2 and 4–3). Our main goals are (a) comparing kinetic temperatures from the gas to temperature estimates based on the dust, (b) searching for a correlation between kinetic temperature and linewidth, which is expected in the case of conversion of turbulent energy into heat, (c) seeking for links between kinetic temperature and star formation rate as well as evolutionary stage of the massive star forming regions, and (d) testing the star formation law by correlating the luminosity of the H_2CO lines to infrared luminosity.

In Sections 2 and 3, we describe the measured samples, our H_2CO observations and the data reduction, and introduce the main results. The discussion is presented in Section 4. Our main conclusions are summarized in Section 5.

2. Sample, observations and data reduction

We have selected the 110 brightest clumps from the ATLASGAL survey (the TOP100 sample) obeying simple IR criteria to cover a range in evolutionary stages as described in Giannetti et al. (2014) and König et al. (2017). They consist almost entirely of clumps that have the potential to form, or are forming, massive stars. Depending on their IR and radio continuum properties, the sample of potentially high-mass star forming clumps at various evolutionary stages can be separated into four categories: 70 μm weak sources (70w), infrared weak clumps (IRw), infrared bright objects (IRb), and sources containing compact H II regions (H II) (Giannetti et al. 2014; König et al. 2017). Previous work on this sample addressed SiO emission (for parts of the sample, Csengeri et al. 2016), dust continuum characterization (König et al. 2017), millimeter hydrogen recombination lines (for more evolved (i.e. H II regions) parts of the sample, Kim et al. 2017), and temperature structure (Giannetti et al. 2017). The TOP100 is an ideal sample to study the physical and chemical parameters of the potentially massive star-forming regions at various evolutionary stages.

Table 1. Observed H_2CO transition parameters.

Transition	Frequency GHz	E_u K	Receiver	Beam size arcsec
o-H_2CO 3_{13}–2_{12}	211.212	32.06	PI230	29.5
p-H_2CO 3_{03}–2_{02}	218.222	20.96	PI230	28.6
p-H_2CO 3_{22}–2_{21}	218.476	68.09	PI230	28.6
p-H_2CO 3_{21}–2_{20}	218.760	68.11	PI230	28.5
o-H_2CO 3_{12}–2_{11}	225.699	33.45	PI230	27.6
p-H_2CO 4_{04}–3_{03}	290.623	34.90	FLASH	21.5
p-H_2CO 4_{23}–3_{22}	291.238	82.07	FLASH	21.4
o-H_2CO 4_{32}–3_{31}	291.381	140.94	FLASH	21.4
o-H_2CO 4_{31}–3_{30}	291.384	140.94	FLASH	21.4
p-H_2CO 4_{22}–3_{21}	291.948	82.12	FLASH	21.4

Table 2. Observed H_2CO transitions and detection rates.

Transition	Observed	Detection	Detection rate
o-H_2CO 3_{13}–2_{12}	94	91	97%
p-H_2CO 3_{03}–2_{02}	94	92	98%
p-H_2CO 3_{22}–2_{21}	94	65	69%
p-H_2CO 3_{21}–2_{20}	94	66	70%
o-H_2CO 3_{12}–2_{11}	94	93	99%
p-H_2CO 4_{04}–3_{03}	98	97	99%
p-H_2CO 4_{23}–3_{22}	98	80	82%
o-H_2CO 4_{32}–3_{31}	98	83	85%
o-H_2CO 4_{31}–3_{30}	98	83	85%
p-H_2CO 4_{22}–3_{21}	98	83	85%

Sources observed are listed in Table A.1. Our observations were carried out on 2013 July and December, 2014 September and November, and 2015 April, June, July, and October with the Atacama Pathfinder EXperiment (APEX[1]) 12 m telescope located on Chajnantor (Chile). Specific observational details of the ten measured transitions of H_2CO are listed in Table 1. Five transitions of H_2CO ($J = 3$–2) were observed with the new MPIfR 1-mm receiver (PI230) with a beam size from 27.6″ to 29.5″ and integration times of 1 to 3 minutes. Five H_2CO ($J = 4$–3) transitions were observed with the FLASH receiver with a beam size ∼21.4″ and integration times of 2 to 4 minutes. For the PI230 receiver, we used a Fast Fourier Transform Spectrometer (FFTS4G) backend with two sidebands (Lower and Upper). Each sideband has two spectral windows of 4 GHz bandwidth, providing both orthogonal polarizations, and leading to a total bandwidth of 8 GHz. An eXtended bandwidth Fast Fourier Transform Spectrometer (XFFTS) backend with two spectral windows of 2.5 GHz bandwidth leading to a total

[1] This publication is based on data acquired with the Atacama Pathfinder EXperiment (APEX). APEX is a collaboration between the Max-Planck-Institut für Radioastronomie, the European Southern Observatory, and the Onsala Space Observatory.

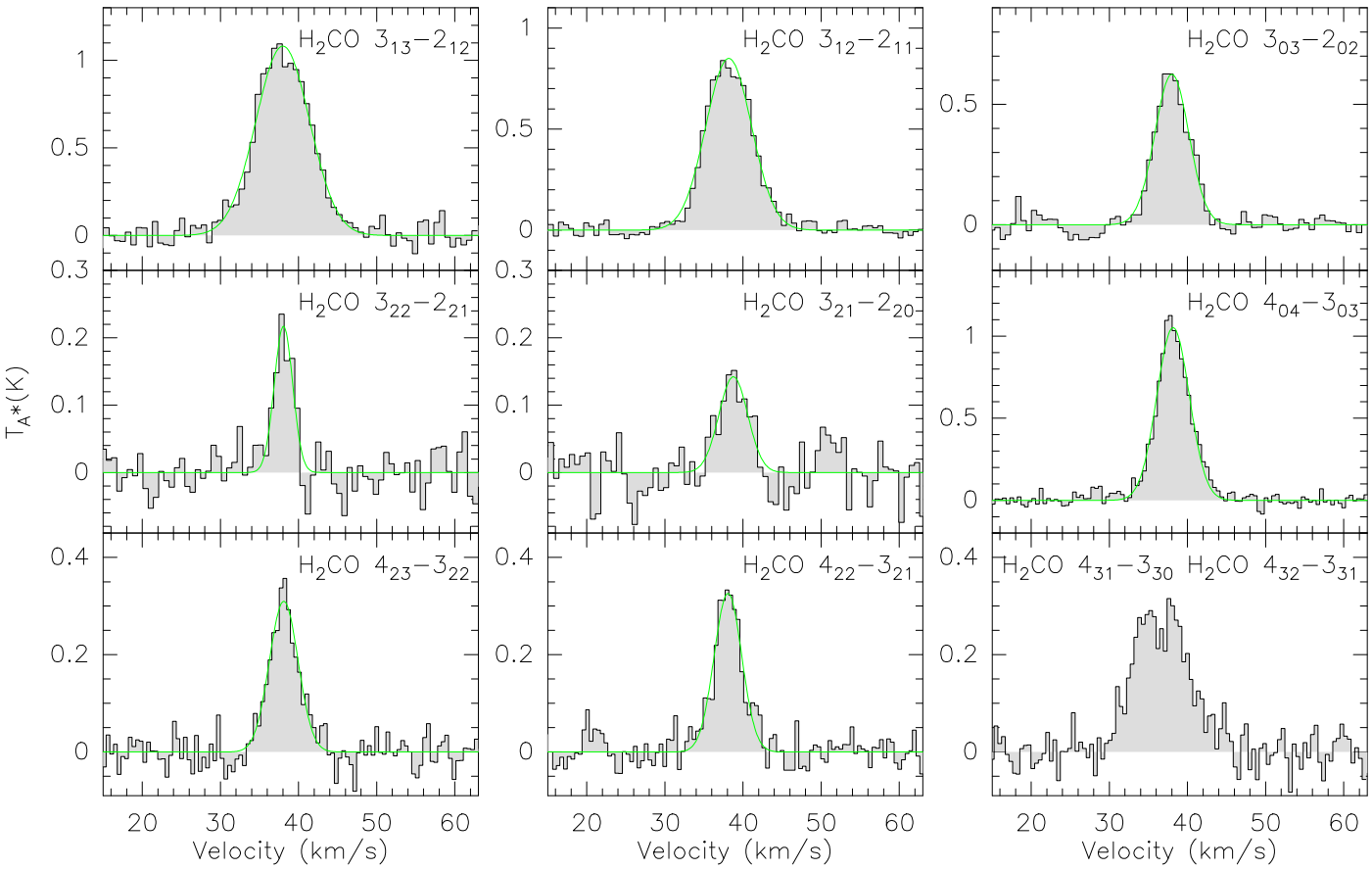

Fig. 1. Observed H_2CO spectra (in grey colour) toward AGAL008.684−00.367. Green lines indicate the Gaussian fit results.

bandwidth of 4 GHz was used for the FLASH receiver. These provide velocity resolutions of ~0.08 km s^{-1} for H_2CO (J = 3–2) and ~0.04 km s^{-1} for H_2CO (J = 4–3). The observations were performed in position-switching mode with off-positions offset from the on-position of the sources by (600″,±600″). We converted the antenna temperatures of the spectra into main beam brightness temperatures for both H_2CO J = 3–2 and 4–3 lines using a factor of 1/0.69. Observed continuum of Mars, Jupiter, and Saturn were used to calibrate the spectral line flux. The calibration uncertainty is about 20%.

Data reduction of spectral lines was performed using CLASS from the GILDAS package[2]. To enhance signal to noise ratios (S/N) in individual channels, we smoothed contiguous channels to a velocity resolution of ~0.6 km s^{-1}. The linewidths tend to be > few km s^{-1}, so the smoothing has no impact on our results. The typical noise level is ~0.06 K (T_{mb} scale) for both H_2CO (J = 3–2) and H_2CO (J = 4–3) at a velocity resolution of ~0.6 km s^{-1}.

3. Results

3.1. Overview

94 sources with H_2CO (J = 3–2) transitions and 98 sources with H_2CO (J = 4–3) transitions were observed. Toward the targeted massive clumps (see Tab. 2) nearly all H_2CO lines are detected (detection rate $\gtrsim$ 97%) for the upper energy above ground state, E_u, (<35 K). For high E_u (>82 K), the H_2CO detection rate ranges from 82% to 85%. Non-detections are associated with 70w and IRw sources (see Sect. 2 for the definitions) which are typically associated with the early cold evolutionary stages of massive clumps. Two para-H_2CO (3_{22}–2_{21} and 3_{21}–2_{20}) transitions (E_u ~ 68 K) show a lower detection rate (~70%), which is caused by the fact that para-H_2CO is the less-abundant of the two H_2CO symmetry species and the source of the weaker K = 2 transitions. High detection rates of H_2CO indicate that this species is commonly formed in massive star-forming clumps and is present during all their evolutionary stages.

Examples of H_2CO line spectra are presented in Figure 1. Line parameters are listed in Tables A.2, A.3, A.4, and A.5, where velocity-integrated intensity, $\int T_{mb} dv$, local standard of rest velocity, V_{lsr}, full width to half maximum linewidth, FWHM, and peak main beam brightness temperature, T_{mb}, were obtained from Gaussian fits. The rest frequencies of the ortho-H_2CO 4_{32}–3_{31} and 4_{31}–3_{30} transitions are nearby (see Tab. 1 and Fig. 1). These two lines are blended in all of our sources, so that Gaussian fits are of limited value and are not part of our tables.

3.2. Source size correction

The para-H_2CO J = 3–2 (beam size ~ 28.6″) and 4–3 (beam size ~ 21.5″) lines we observed were obtained by single pointing observations with different receivers, so the area covered by our J = 3–2 and 4–3 transitions is slightly different. We compare the integrated intensities of H_2CO, irrespective of the beam size, with 870 μm flux densities in Figure 2. It shows that the H_2CO integrated intensities follow the 870 μm intensity distribution. Apparently dense gas traced by H_2CO is associated

[2] http://www.iram.fr/IRAMFR/GILDAS

well with the dust traced by 870 μm emission in the massive star-forming clumps. Mapping observations of para-H_2CO (3_{03}–2_{02}, 3_{22}–2_{21}, and 3_{21}–2_{20}) towards the Orion molecular cloud 1 (OMC1) with the APEX telescope also show that para-H_2CO integrated intensity distributions agree well with the dust emission observed at 850 μm (Johnstone & Bally 1999; Tang et al. 2017c). Previous observations of H_2CO (4_{04}–3_{03}, 4_{23}–3_{22}, 4_{22}–3_{21}, 4_{32}–3_{31}, and 4_{31}–3_{30}) towards massive clumps in the W33 region with the APEX telescope (Immer et al. 2014) also indicate that H_2CO distributions are consistent with the dust emission traced by 870 μm. So here we assume that the source sizes of H_2CO are the same as the full width to half power source sizes of the 870 μm dust emission derived from Csengeri et al. (2014). We correct for beam dilution by calculating $T'_{\rm mb} = T_{\rm mb}/\eta_{\rm bf}$ with beam-filling factor $\eta_{\rm bf} = \theta_{\rm s}^2/(\theta_{\rm s}^2+\theta_{\rm beam}^2)$. Here $\theta_{\rm beam}$ and $\theta_{\rm s}$ denote beam and source size, respectively. The results of $\eta_{\rm bf}$ and the para-H_2CO 4_{04}–3_{03}/3_{03}–2_{02} integrated intensity ratio ($I'(4_{04}$–$3_{03})/I'(3_{03}$–$2_{02})$) corrected with $\eta_{\rm bf}$ are listed in Table A.6.

3.3. Opacities of H_2CO

To determine the gas kinetic temperatures, $T_{\rm kin}$, spatial densities, $n(H_2)$, and para-H_2CO column densities, $N(H_2CO)$, we use the RADEX non-LTE model (van der Tak et al. 2007) offline code[3] with collision rates from Wiesenfeld & Faure (2013). Uncertainties in the collisional excitation rates directly affect the derived volume densities, while kinetic temperature appears to be less affected by collisional excitation rate uncertainties (see Sect. 3.4). The RADEX code needs five input parameters: background temperature, kinetic temperature, H_2 density, H_2CO column density, and linewidth. For the background temperature, we adopted 2.73 K. Model grids for the H_2CO lines encompass 40 densities ($n(H_2) = 10^4$–10^8 cm^{-3}), 40 H_2CO column densities ($N(H_2CO) = 10^{12}$–10^{16} cm^{-2}), and 40 temperatures ranging from 10 to 400 K. For the linewidth, we use the observed linewidth value.

The value of N(para-H_2CO) depends on para-H_2CO 3_{03}–2_{02} and/or 4_{04}–3_{03} integrated intensities and the para-H_2CO 4_{04}–3_{03}/3_{03}–2_{02} ratio (Mangum & Wootten 1993; Tang et al. 2017a). If the para-H_2CO 3_{03}–2_{02} and 4_{04}–3_{03} lines are optically thick in our dense massive clumps, this would cause high para-H_2CO 4_{04}–3_{03}/3_{03}–2_{02}, 3_{21}–2_{20}/3_{03}–2_{02}, and 4_{22}–3_{21}/4_{04}–3_{03} ratios. Higher ratios will imply higher spatial densities and kinetic temperatures, respectively (Mangum & Wootten 1993; Ao et al. 2013; Ginsburg et al. 2016; Immer et al. 2016; Tang et al. 2017a,b,c). In order to understand the impact of the line optical depth, we modelled the optical depth of para-H_2CO 3_{03}–2_{02} and para-H_2CO 4_{04}–3_{03} integrated intensities, and the para-H_2CO 4_{04}–3_{03}/3_{03}–2_{02} ratio at a kinetic temperature of 55 K (see Sect. 3.4) in Figure 3 (or see Figure G.2 in Immer et al. 2016). Changing the kinetic temperature, weakly affects the optical depth of the para-H_2CO 3_{03}–2_{02} and para-H_2CO 4_{04}–3_{03} lines (less than by a factor of few). The para-H_2CO 4_{04}–3_{03}/3_{03}–2_{02} ratio is then also not greatly changed ($\lesssim$30%; not shown here). The figure demonstrates that para-H_2CO 3_{03}–2_{02} is optically thin ($\tau < 1$) at column density N(para-H_2CO) $< 1\times10^{14}$ cm^{-2} and spatial density 10^{4-8} cm^{-3}. At higher column density (N(para-H_2CO) $> 5\times10^{14}$ cm^{-2}), the para-H_2CO 3_{03}–2_{02} becomes optically thick ($\tau > 5$). The optical depth of para-H_2CO 4_{04}–3_{03} shows a similar behavior (slightly lower values) with respect to that of para-H_2CO 3_{03}–2_{02} (not shown here; or see Figure G.2 in Immer et al. 2016).

[3] http://var.sron.nl/radex/radex.php

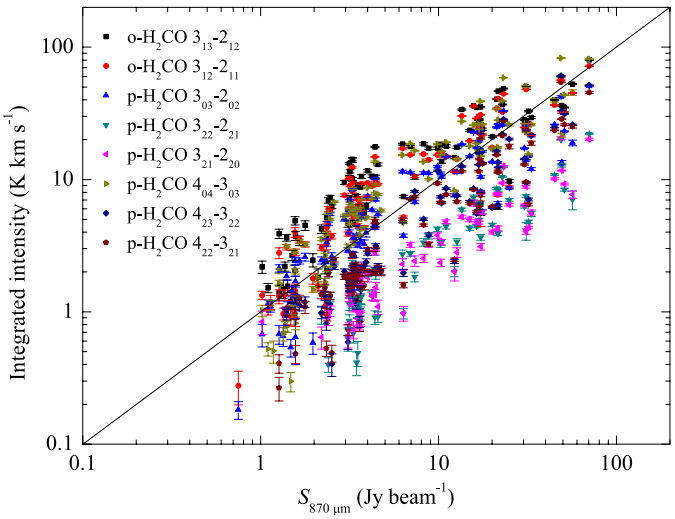

Fig. 2. Comparison of integrated intensities of H_2CO and 870 μm continuum flux densities. The solid line corresponds to Y = X in the given units.

Considering the observed ranges of integrated intensities of para-H_2CO 4_{04}–3_{03} (typical value $\sim$ 20 K km s^{-1}) and para-H_2CO 4_{04}–3_{03}/3_{03}–2_{02} ratios (typical value $\sim$ 1.0) accounting for relevant beam-filling factors from Section 3.2 (see Tabs. A.4 and A.6), the optical depths of para-H_2CO 3_{03}–2_{02} and 4_{04}–3_{03} range from $\sim$0.012 to $\sim$1 in our sample. Compared to the para-H_2CO 3_{03}–2_{02} and 4_{04}–3_{03} lines, para-H_2CO 3_{22}–2_{21}, 3_{21}–2_{20}, 4_{23}–3_{22}, and 4_{22}–3_{21} lines have higher upper energies above the ground state ($E_{\rm u} > 68$ K, see Tab. 1), so they have lower optical depths ($\tau \ll 1$). Therefore, the influence of the para-H_2CO 3_{03}–2_{02} and 4_{04}–3_{03} optical depths is weak for our determination of spatial density and kinetic temperature.

In our sample the observed $T_{\rm mb}(3_{12}$–$2_{11}/3_{03}$–$2_{02})$ ratios range from 0.74 to 1.83 with an unweighted average of 1.29 ± 0.02 (see Tabs. A.2 and A.3; errors given here and elsewhere are standard deviations of the mean). For the $T_{\rm mb}(3_{13}$–$2_{12}/3_{03}$–$2_{02})$ ratio, it ranges from 1.03 to 2.35 with an unweighted average of 1.56 ± 0.03 (see Tabs. A.2 and A.3). The relation between $T_{\rm mb}(3_{12}$–$2_{11}/3_{03}$–$2_{02})$ and H_2CO optical depth, indicated by Sasselov & Rucinski (1990) in their Figure 2, suggests that for at least 30% of our sample ($T_{\rm mb}(3_{12}$–$2_{11}/3_{03}$–$2_{02}) \lesssim 1.19$) the ortho-H_2CO 3_{12}–2_{11} and 3_{13}–2_{12} lines are optically thick ($\tau \gtrsim 5$).

3.4. Kinetic temperature

As discussed in Section 1, the intensity ratios of H_2CO lines involving different $K_{\rm a}$ ladders yield estimates of the kinetic temperature of the gas (Mangum & Wootten 1993). For our observed transitions of H_2CO, para-H_2CO 3_{21}–2_{20}/3_{03}–2_{02}, 3_{22}–2_{21}/3_{03}–2_{02}, 4_{22}–3_{21}/4_{04}–3_{03}, and 4_{23}–3_{22}/4_{04}–3_{03} ratios can be useful thermometers to derive the kinetic temperature. Para-H_2CO 3_{22}–2_{21}/3_{03}–2_{02} and 3_{21}–2_{20}/3_{03}–2_{02} ratios trace the kinetic temperature with an uncertainty of $\lesssim$25% below 50 K (Mangum & Wootten 1993). Para-H_2CO 4_{22}–3_{21}/4_{04}–3_{03} and 4_{23}–3_{22}/4_{04}–3_{03} ratios trace the kinetic temperature with an uncertainty of $\lesssim$25% below 75 K (Mangum & Wootten 1993). The para-H_2CO 3_{22}–2_{21}/3_{03}–2_{02} and 4_{23}–3_{22}/4_{04}–3_{03} line ratios are slightly affected by the spatial density (not shown here; for para-H_2CO 3_{22}–2_{21}/3_{03}–2_{02} see Lindberg et al. 2015 and Tang et al. 2017a). So in this work we use the para-H_2CO 3_{21}–2_{20}/3_{03}–2_{02}

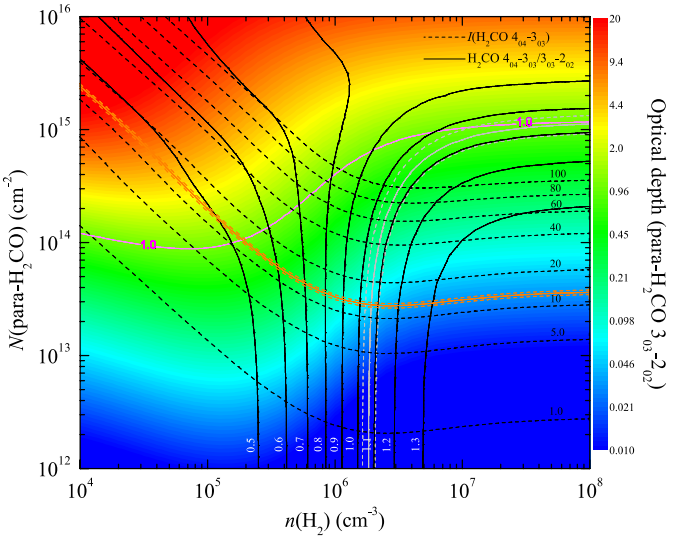

Fig. 3. Example of RADEX non-LTE modeling of the $N(H_2CO)$–$n(H_2)$ relation for AGAL008.684−00.367 at a kinetic temperature of 55 K (see Sect. 3.4). Black dashed and solid lines are para-H_2CO 4_{04}–3_{03} integrated intensities and para-H_2CO 4_{04}–$3_{03}/3_{03}$–2_{02} integrated intensity ratios, respectively. To the measured parameters, para-H_2CO 4_{04}–3_{03} integrated intensity (orange solid and dashed lines represent observed value and uncertainty) and para-H_2CO 4_{04}–$3_{03}/3_{03}$–2_{02} integrated intensity ratio (white solid and dashed lines) corrected by the relevant beam-filling factors (see Tab. A.6). The colour map shows the optical depth of the para-H_2CO 3_{03}–2_{02} line. The purple line in the upper green area corresponds to optical depth τ(para-H_2CO 3_{03}–2_{02}) = 1.0.

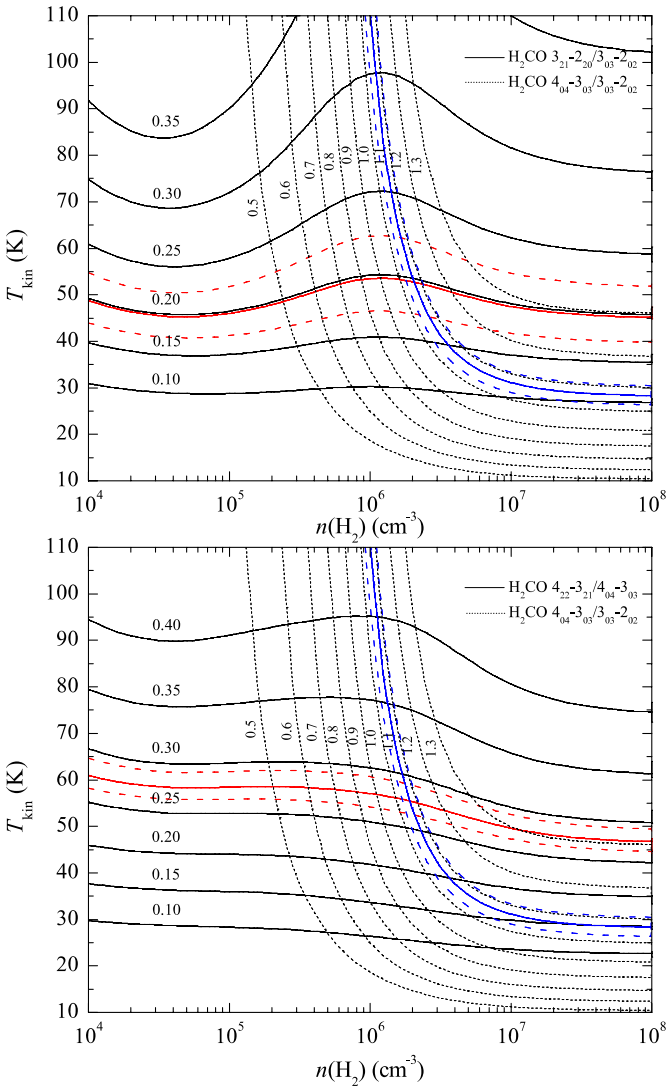

Fig. 4. Example of RADEX non-LTE modeling of the para-H_2CO kinetic temperature for AGAL008.684−00.367. Black solid and dashed lines are para-H_2CO integrated intensity ratios. Para-H_2CO 4_{04}–$3_{03}/3_{03}$–2_{02} (blue solid and dashed lines represent observed value and uncertainty, accounting for different beam-filling factors), 3_{21}–$2_{20}/3_{03}$–2_{02} and 4_{22}–$3_{21}/4_{04}$–3_{03} integrated intensity ratios (top and bottom, red solid and dashed lines) for a para-H_2CO column density 2.8×10^{13} cm^{-2} derived from the para-H_2CO 4_{04}–3_{03} integrated intensity and para-H_2CO 4_{04}–$3_{03}/3_{03}$–2_{02} ratio (see Sect. 3.3).

and 4_{22}–$3_{21}/4_{04}$–3_{03} integrated intensity ratios to derive the kinetic temperature, which also have been used for the Galactic central molecular zone (CMZ) clouds (Ginsburg et al. 2016; Immer et al. 2016).

We ran RADEX to calculate the observed para-H_2CO 3_{21}–$2_{20}/3_{03}$–2_{02}, 4_{22}–$3_{21}/4_{04}$–3_{03}, and 4_{04}–$3_{03}/3_{03}$–2_{02} integrated intensity ratios corrected by the relevant beam-filling factors assuming these transitions of para-H_2CO are optically thin (see Sect. 3.3). In Figure 4, an example is presented to show how the parameters are constrained by the line ratio distribution of para-H_2CO, accounting for different beam-filling factors in the T_{kin}–$n(H_2)$ parameter space. We used the column density derived from the para-H_2CO 4_{04}–3_{03} integrated intensity and para-H_2CO 4_{04}–$3_{03}/3_{03}$–2_{02} ratio accounting for the beam-filling factors derived in Section 3.2 to constrain the kinetic temperature. It shows that para-H_2CO 3_{21}–$2_{20}/3_{03}$–2_{02} and 4_{22}–$3_{21}/4_{04}$–3_{03} line ratios are sensitive to the gas kinetic temperature (see the black solid lines in Fig. 4), while being relatively independent of spatial density. The integrated intensity ratio $I'(4_{04}$–$3_{03})/I'(3_{03}$–$2_{02})$ is sensitive to the gas spatial density at high temperature ($T_{kin} > 40$ K), where the $I'(4_{04}$–$3_{03})/I'(3_{03}$–$2_{02})$ ratio becomes relatively independent of kinetic temperature. At low temperature ($T_{kin} < 40$ K), this ratio is influenced almost entirely by the gas kinetic temperature, because T_{kin} becomes lower than the excitation difference of the involved states. Therefore, para-H_2CO 3_{21}–$2_{20}/3_{03}$–2_{02} and 4_{22}–$3_{21}/4_{04}$–3_{03} ratios combined with the para-H_2CO 4_{04}–$3_{03}/3_{03}$–2_{02} ratio are good tracers to constrain kinetic temperature and spatial density of dense gas in warm regions (gas temperature >30 K, for lower T_{kin} the levels of the $J = 3$–2 and 4–3 $K_a > 0$ lines are too far above the ground state) of massive star-forming clumps. With the two $J = 4$, $K_a = 2$ levels being located 80–90 K above the ground state (see Tab. 1), the radiative transfer models start to become insensitive to temperatures in excess of 150 K. So temperatures >150 K have to be considered sceptically and should cautiously be interpreted as ≳150 K (Mangum & Wootten 1993; Ginsburg et al. 2016; Immer et al. 2016). The derived kinetic temperatures are listed in Table A.6.

We note a para-H_2CO 3_{21}–$2_{20}/3_{03}$–2_{02} ratio "bump" at kinetic temperature >50 K and spatial density $10^{5.5-7.0}$ cm^{-3} in Figure 4 (or see Figure 13 in Mangum & Wootten (1993) and Figure F.1 in Lindberg et al. (2015)), because the excitation temperature of the para-H_2CO 3_{21}–2_{20} line rises much faster than that of the para-H_2CO 3_{03}–2_{02} line with increasing spatial density and/or kinetic temperature (Mangum & Wootten 1993). Kinetic temperatures obtained for a given para-H_2CO 3_{21}–$2_{20}/3_{03}$–2_{02} ratio vary more than by ≳20% at kinetic temperature >60 K

and spatial density $10^{5.0-7.0}$ cm^{-3}. This large "bump" in the para-H_2CO 3_{21}–2_{20}/3_{03}–2_{02} contour (see Fig. 4 upper panel) probably leads to an overestimate of the kinetic temperature from the para-H_2CO 3_{21}–2_{20}/3_{03}–2_{02} ratio. Para-H_2CO 4_{22}–3_{21}/4_{04}–3_{03} is also influenced by a "bump", this time at kinetic temperature >100 K and spatial density $10^{5.5-7.0}$ cm^{-3} (see Fig. 4 lower panel or Figure 13 in Mangum & Wootten 1993). Kinetic temperatures derived from the para-H_2CO 4_{22}–3_{21}/4_{04}–3_{03} ratio vary less than $\lesssim$20% for $T_{\rm kin} < 150$ K and spatial density $10^{5.0-7.0}$ cm^{-3}. It appears that the para-H_2CO 4_{22}–3_{21}/4_{04}–3_{03} ratio is more stable and accurate to trace gas kinetic temperature than the para-H_2CO 3_{21}–2_{20}/3_{03}–2_{02} ratio at $T_{\rm kin} < 150$ K and spatial density $10^{5.0-7.0}$ cm^{-3}.

A comparison of kinetic temperatures derived from both para-H_2CO 3_{21}–2_{20}/3_{03}–2_{02} and 4_{22}–3_{21}/4_{04}–3_{03} ratios suggests that the two ratios trace similar temperatures (see Fig. 5). It might have been expected, for example by analogy to NH_3 (e.g., Henkel et al. 1987; Mangum et al. 2013a; Gong et al. 2015a,b), that higher excited H_2CO transitions lead to higher $T_{\rm kin}$ values. Some of the similar kinetic temperatures derived from the para-H_2CO 3_{21}–2_{20}/3_{03}–2_{02} and 4_{22}–3_{21}/4_{04}–3_{03} ratios (Fig. 5) might be caused by the para-H_2CO 3_{21}–2_{20}/3_{03}–2_{02} ratio "bump" (Fig. 4, top panel). This excitation effect in the para-H_2CO 3_{21}–2_{20}/3_{03}–2_{02} ratio may result in an overestimate of the kinetic temperature derived from this ratio with large uncertainty ($\gtrsim$20% at kinetic temperature >60 K) at spatial density $10^{5.5-7.0}$ cm^{-3}.

The para-H_2CO line intensity ratios 3_{22}–2_{21}/3_{03}–2_{02}, 3_{21}–2_{20}/3_{03}–2_{02}, 4_{23}–3_{22}/4_{04}–3_{03} and 4_{22}–3_{21}/4_{04}–3_{03} can also provide a measurement of the kinetic temperature of the gas assuming local thermodynamic equilibrium (LTE). The kinetic temperature can be calculated from these para-H_2CO transition ratios if the lines are optically thin (see Sect. 3.3), and originate from a high density region (Mangum & Wootten 1993). Following the method applied by Mangum & Wootten (1993) in their Appendix A,

$$T_{\rm LTE} = \frac{47.1}{ln(0.556\frac{I(3_{03}-2_{02})}{I(3_{21}-2_{20})})}\ {\rm K} \quad (1)$$

and

$$T_{\rm LTE} = \frac{47.2}{ln(0.750\frac{I(4_{04}-3_{03})}{I(4_{22}-3_{21})})}\ {\rm K}, \quad (2)$$

where $I(3_{03}–2_{02})/I(3_{21}–2_{20})$ and $I(4_{04}–3_{03})/I(4_{22}–3_{21})$ are the para-H_2CO integrated intensity ratios. The results of the kinetic temperature calculations from the para-H_2CO 3_{03}–2_{02}/3_{21}–2_{20} and 4_{04}–3_{03}/4_{22}–3_{21} integrated intensity ratios are listed in Table A.6. If the assumption of optically thin emission is correct, the kinetic temperatures derived from this method have an uncertainty of $\lesssim$30% (Mangum & Wootten 1993). We also compared the kinetic temperatures derived from LTE and RADEX non-LTE calculations (see Fig. 5). It appears that $T_{\rm non-LTE}$ is consistently higher than $T_{\rm LTE}$ by $\lesssim$25%. This might be caused by the fact that at densities of $10^{6.5}$ cm^{-3} (see Sect. 3.5) thermalization is not yet reached (Mangum & Wootten 1993). Therefore higher $T_{\rm kin}$ values are need to compensate for this effect leading to lower excitation temperatures, and to reproduce data.

3.5. Spatial density and column density

As described in Section 1, with the kinetic temperature approximately known, the relative intensity ratio of H_2CO lines involving the same K_a ladders yields estimates of the spatial density of the gas (Henkel et al. 1980, 1983; Mangum & Wootten 1993). For our observed transitions of H_2CO, para-H_2CO 4_{04}–3_{03}/3_{03}–2_{02}, 4_{22}–3_{21}/3_{21}–2_{20} (or 4_{22}–3_{21}/3_{22}–2_{21}), and 4_{23}–3_{22}/3_{22}–2_{21} (or 4_{23}–3_{22}/3_{21}–2_{20}) ratios are good densitometers to derive the spatial density. The para-H_2CO 3_{03}-2_{02} and 4_{04}–3_{03} lines are the strongest of the 218 GHz and 291 GHz transitions, respectively, and they are nearly all detected in our sample (see Tab. 2). So in this work, we use the para-H_2CO 4_{04}–3_{03}/3_{03}–2_{02} integrated intensity ratio to derive the spatial density, which has also been

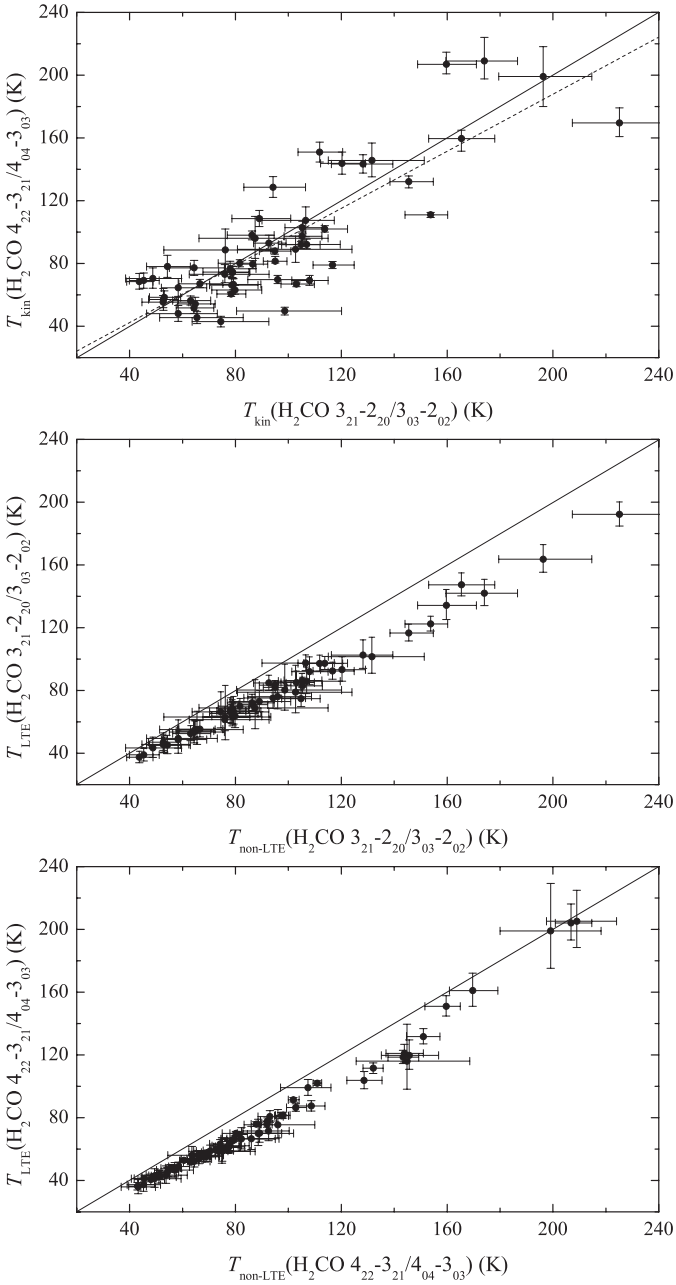

Fig. 5. Top panel: Comparison of kinetic temperatures derived from para-H_2CO 3_{21}–2_{20}/3_{03}–2_{02} and 4_{22}–3_{21}/4_{04}–3_{03} ratios. The dashed line is the result from an unweighed linear fit, $T_{\rm kin}(4_{22}–3_{21}/4_{04}–3_{03}) = (0.9 \pm 0.1) \times T_{\rm kin}(3_{21}–2_{20}/3_{03}–2_{02}) + (5.8 \pm 7.8)$, with a correlation coefficient, R, of 0.85. Middle and bottom panels: Comparisons of kinetic temperatures derived from LTE and RADEX non-LTE calculations for para-H_2CO 3_{21}–2_{20}/3_{03}–2_{02} and 4_{22}–3_{21}/4_{04}–3_{03} ratios, respectively. The temperature uncertainties are obtained from observed para-H_2CO line ratio errors. Solid lines indicate equal temperatures.

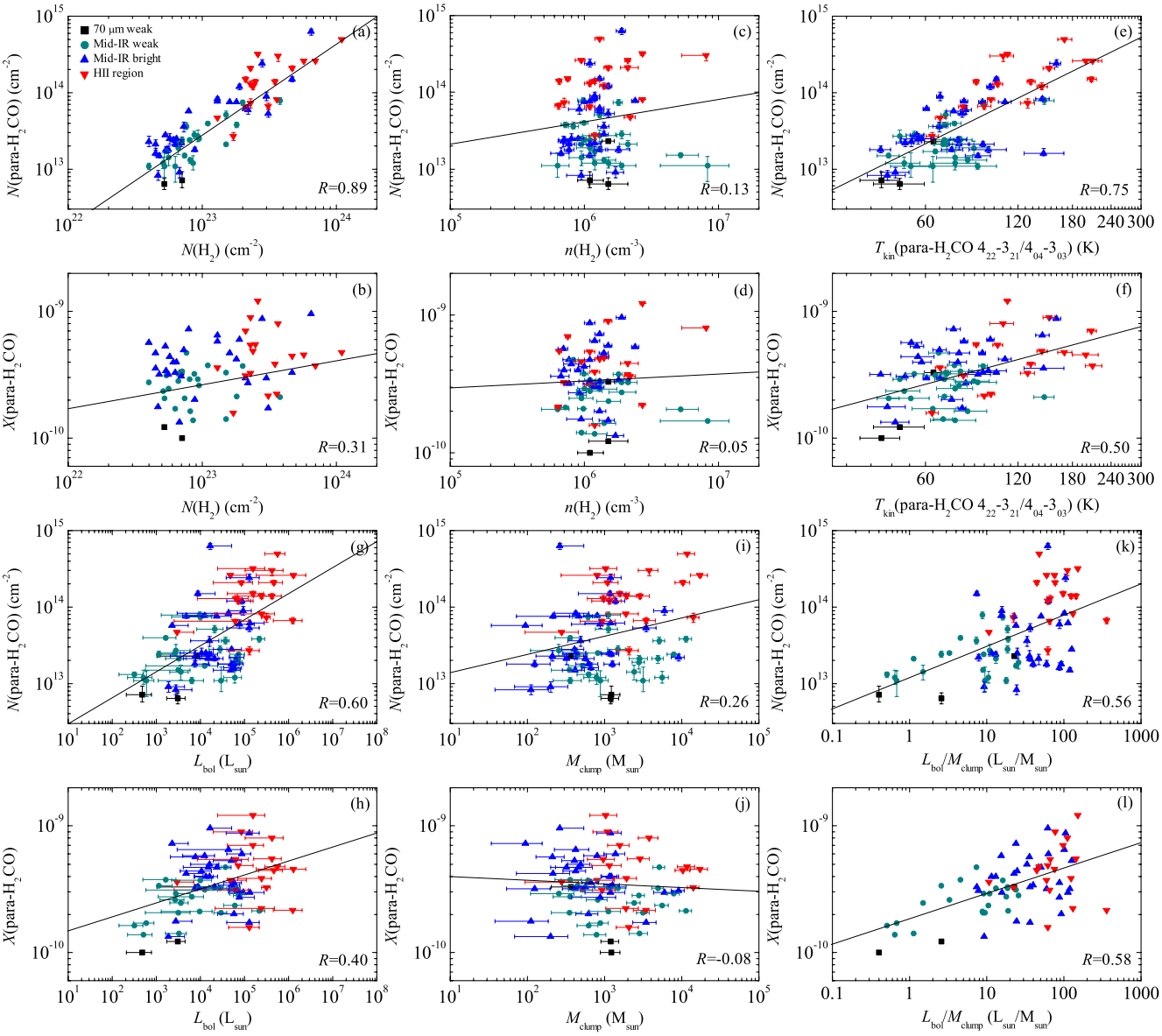

Fig. 6. Column density N(para-H_2CO) and fractional abundance X(para-H_2CO) vs. column density $N(H_2)$ (a, b), spatial density $n(H_2)$ (c, d), kinetic temperature T_{kin}(para-H_2CO 4_{22}–3_{21}/4_{04}–3_{03}) (e, f), bolometric luminosity (g, h), mass of clump (i, j), and luminosity-to-mass L_{bol}/M_{clump} ratio (k, l). The column density and spatial density uncertainties are obtained from observed para-H_2CO line brightness temperature and line ratio errors. The straight lines are the results from unweighed linear fits yielding the given correlation coefficients, R, in the lower right corner of each panel.

Table 3. Averaged parameters in different stages of the massive clumps.

Stage	T_{kin} K	$n(H_2)$ $\times10^6$ cm^{-3}	N(para-H_2CO) $\times10^{13}$ cm^{-2}	X(para-H_2CO) $\times10^{-10}$	Δv(para-H_2CO 4_{04}–3_{03}) km s^{-1}
70w	52 ± 6	1.2 ± 0.2	1.2 ± 0.6	1.8 ± 0.7	3.9 ± 0.4
IRw	73 ± 4	1.7 ± 0.4	2.7 ± 0.4	2.7 ± 0.2	4.8 ± 0.2
IRb	81 ± 6	1.2 ± 0.1	7.2 ± 2.1	4.3 ± 0.4	4.9 ± 0.3
H II region	110 ± 8	1.8 ± 0.4	16.9 ± 0.3	4.9 ± 0.6	7.4 ± 0.4
average	91 ± 4	1.5 ± 0.1	8.0 ± 1.3	3.9 ± 0.2	5.3 ± 0.2

used in molecular clouds of the Galactic CMZ (Immer et al. 2016).

We ran RADEX to obtain para-H_2CO column densities and spatial density, and calculated the observed para-H_2CO 3_{03}–2_{02} and 4_{04}–3_{03} integrated intensities in K km s^{-1} units corrected by the relevant beam-filling factors ($I \rightarrow I'$). In Figure 3, an example is presented to show how the parameters are constrained by the corrected integrated line intensity and integrated line intensity ratio distribution of para-H_2CO in the N(para-H_2CO)–$n(H_2)$ parameter space. This figure shows that at low column

density (N(para-H_2CO) $< 5\times10^{14}$ cm^{-2}) the $I'(4_{04}–3_{03})/I'(3_{03}–2_{02})$ ratio accounting for different beam-filling factors (see the black solid lines) is sensitive to the gas spatial density and becomes relatively independent of the para-H_2CO column density, while the kinetic temperature is kept constant at ~55 K (which is close to the actual temperature, see above). At high column density (N(para-H_2CO) $> 5\times10^{14}$ cm^{-2}) the $I'(4_{04}–3_{03})/I'(3_{03}–2_{02})$ ratio appears to be not sensitive to the gas spatial density and becomes dependent on the column density, because the para-H_2CO $3_{03}–2_{02}$ transition starts to become optically thick (Mangum & Wootten 1993). The derived results of N(para-H_2CO) and spatial density are listed in Table A.6. We use the same method to obtain ortho-H_2CO column densities with the observed ortho-H_2CO ($3_{12}–2_{11}$ and $3_{13}–2_{12}$) integrated intensities adopting kinetic temperature and spatial density derived from para-H_2CO line ratios (see Sect. 3.4 and above) and assuming ortho- and para-H_2CO originate from the same region. The obtained results of N(ortho-H_2CO) are listed in Table A.6.

As mentioned in Section 3.3, the para-H_2CO $3_{22}–2_{21}$, $3_{21}–2_{20}$, $4_{23}–3_{22}$, and $4_{22}–3_{21}$ lines are optically thin, so the para-H_2CO $4_{22}–3_{21}/3_{21}–2_{20}$ (or $4_{23}–3_{22}/3_{22}–2_{21}$) ratio is weakly affected by optical depths. To further check how optical depths influence the para-H_2CO $4_{04}–3_{03}/3_{03}–2_{02}$ ratio, we use the above method also with the para-H_2CO $4_{22}–3_{21}/3_{21}–2_{20}$ ratio to constrain spatial density. The spatial densities obtained both from para-H_2CO $4_{04}–3_{03}/3_{03}–2_{02}$ (typical value ~ 1.0) and $4_{22}–3_{21}/3_{21}–2_{20}$ (typical value ~ 1.5) ratios yield similar values ($n(H_2) \sim 2\times10^6$ cm^{-3}), which confirms that para-H_2CO $3_{03}–2_{02}$ and $4_{04}–3_{03}$ lines are not strongly affected by saturation effects when trying to constrain spatial density and kinetic temperature in our sample. However, the ortho-H_2CO $3_{12}–2_{11}$ and $3_{13}–2_{12}$ lines are affected by opacities $\gtrsim 1$ in parts of our sample (see Sect. 3.3), so the N(ortho-H_2CO) may be underestimated in these sources.

The 870 μm continuum source angular sizes range from 22″ to 42″ with an average of 29″ in our sample. If the sizes of H_2CO are much smaller than those of the 870 μm continuum (and/or our beam size; see Tab. 1), the beam-filling factor is overestimated. If we assume that the H_2CO to 870 μm emission size ratio ($\theta_{H_2CO}/\theta_{870\,\mu m}$) is 90%, 80%, and 70%, for AGAL008.684−00.367 as an example (see Fig. 3), $n(H_2)$ decreases by 6%, 17%, and 23%. Mapping observations of massive clumps in CS (7-6) (Wu et al. 2010) and 350 μm continuum emission (Mueller et al. 2002) show that the median ratio of CS (7-6) emission size to the 350 μm continuum emission size is ~0.87 (Liu et al. 2016). Also considering the slightly different beam sizes for para-H_2CO $3_{03}–2_{02}$ and $4_{04}–3_{03}$ lines (see Sect. 3.2), we conclude that the beam-filling factor is not strongly influencing our results for $n(H_2)$ constrained from para-H_2CO $4_{04}–3_{03}/3_{03}–2_{02}$ line ratios.

The statistical weight ratio of ortho- and para-H_2CO and previous H_2CO observations in other star-forming regions suggest that the ortho-to-para H_2CO abundance ratio is $\lesssim 3$ (Kahane et al. 1984; Mangum & Wootten 1993; Dickens & Irvine 1999; Jørgensen et al. 2005; Guzmán et al. 2011). In most of our sample (~95%) the obtained ortho-to-para H_2CO abundance ratios (N(ortho-H_2CO)/N(para-H_2CO)) range from 1.0 to 3.0 with an unweighted average of 2.0 ± 0.1. Assuming that H_2CO is formed in and expelled from dust grain mantles, this ratio corresponds to a dust temperature of $\lesssim 20$ K (Kahane et al. 1984; Dickens & Irvine 1999).

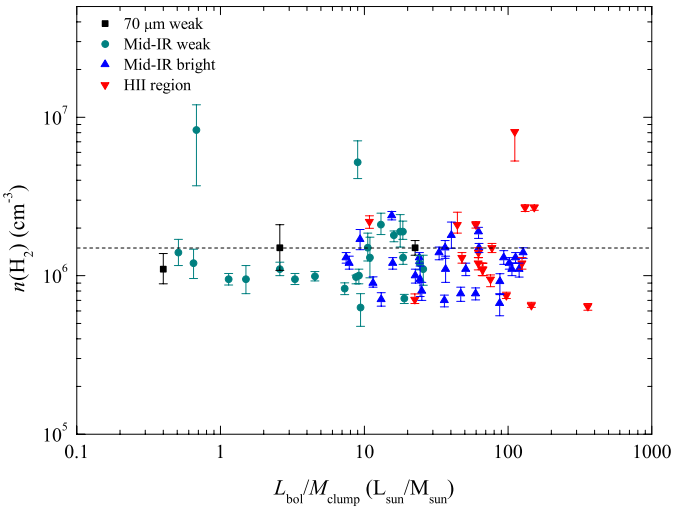

Fig. 7. The spatial density derived from para-H_2CO ($4_{04}–3_{03}/3_{03}–2_{02}$) vs. luminosity-to-mass ratio L_{bol}/M_{clump}. The dashed line indicates the average spatial density.

4. Discussion

4.1. Variations of spatial density and H_2CO abundance

The gas spatial densities, $n(H_2)$, derived from para-H_2CO $4_{04}–3_{03}/3_{03}–2_{02}$ ratios range from 6.3×10^5 to 8.3×10^6 cm^{-3} with an unweighted average of $1.5\,(\pm0.1)\times10^6$ cm^{-3} (Tab. A.6), which agrees with the results determined with para-H_2CO ($5_{05}–4_{04}/3_{03}–2_{02}$ and $5_{24}–4_{23}/3_{22}–2_{21}$) and ortho-$H_2CO$ ($4_{13}–4_{14}/3_{12}–3_{13}$) ratios from other star-forming regions (Mangum & Wootten 1993; Hurt et al. 1996; McCauley et al. 2011; Lindberg et al. 2015). Mapping the same para-H_2CO transitions toward the Galactic CMZ clouds shows that the spatial density of the widespread warm gas is constrained to 10^4–10^6 cm^{-3} (Immer et al. 2016). The spatial densities derived from para-H_2CO line ratios in our massive clumps overlap with the values found for high density regions in the Galactic CMZ clouds (see Table A.6 or Figure 6, and Figure 3 in Immer et al. 2016). The spatial density deduced from the dust indicates 10^3–10^6 cm^{-3} in our sample (Giannetti et al. 2017), which is lower than the spatial densities we obtain. This suggests that H_2CO ($J = 3$–2 and 4–3) traces denser gas than the dust emission.

We derive unweighted averaged spatial densities obtained from para-H_2CO ratios in sources representing four evolutionary stages consisting of 70 μm weak (70w), mid-infrared weak (IRw), and mid-infrared bright (IRb), sources as well as star-forming clouds with ultracompact H II regions. The unweighted averaged spatial densities $n(H_2)$ are $1.2\,(\pm0.2)\times10^6$, $1.7\,(\pm0.4)\times10^6$, $1.2\,(\pm0.1)\times10^6$ cm^{-3}, and $1.8\,(\pm0.4)\times10^6$ cm^{-3} in 70w, IRw, IRb, and H II regions, respectively (see Tab. 3 or Fig. 7). It seems that the averaged spatial densities traced by the para-H_2CO $4_{04}–3_{03}/3_{03}–2_{02}$ ratios do not vary significantly with the evolutionary stage of clumps. This may indicate that the density structure does not evolve significantly as the star formation proceeds. It also suggests that the para-H_2CO $4_{04}–3_{03}/3_{03}–2_{02}$ ratio may be a good densitometer to trace the dense gas at various stages of massive star formation.

N(para-H_2CO) derived from the para-H_2CO $4_{04}–3_{03}/3_{03}–2_{02}$ ratio ranges from 6.4×10^{12} to 6.1×10^{14} cm^{-2} with an unweighted average of $8.0\,(\pm1.3)\times10^{13}$ cm^{-2} (Tab. 3), which

agrees with the results from other protostellar cores and star-forming regions (Mangum & Wootten 1993; Hurt et al. 1996; Watanabe & Mitchell 2008; Tang et al. 2017a). We also derive averaged column densities of para-H_2CO for the four evolutionary stages mentioned above. The unweighted average column densities N(para-H_2CO) are $1.2\,(\pm0.6)\times10^{13}$, $2.7\,(\pm0.4)\times10^{13}$, $7.2\,(\pm2.1)\times10^{13}$, and $16.9\,(\pm0.3)\times10^{13}$ cm^{-2} in 70w, IRw, IRb, and H II regions, respectively (see Tab. 3). The fractional abundance X(para-H_2CO) = N(para-H_2CO)/$N(H_2)$ becomes 1.0×10^{-10}–1.2×10^{-9} with an average of $3.9\,(\pm0.2)\times10^{-10}$, where $N(H_2)$ is derived from the 870 μm continuum emission assuming a dust absorption coefficient $\kappa_{870} = 1.85$ cm^2 g^{-1} at 870 μm and adopting the temperature obtained from the dust (König et al. 2017). Therefore the abundance also agrees with the values found in other star formation regions, Galactic center clouds, and external galaxies (Güsten & Henkel 1983; Zylka et al. 1992; Ao et al. 2013; Gerner et al. 2014; Tang et al. 2017a,b). The unweighted average fractional abundances X(para-H_2CO) are $1.8\,(\pm0.7)\times10^{-10}$, $2.7\,(\pm0.2)\times10^{-10}$, $4.3\,(\pm0.4)\times10^{-10}$, and $4.9\,(\pm0.6)\times10^{-10}$ in 70w, IRw, IRb, and H II regions, respectively (see Tab. 3). Averaged variations of fractional abundances of X(para-H_2CO) in different stages of star formation amount to nearly a factor of 3, which agrees with observed results in other massive star formation regions (van der Tak et al. 2000a,b; Gerner et al. 2014; Tang et al. 2017a). Therefore, we confirm that H_2CO can be widely used as a probe to trace the dense gas without drastic changes in abundance during various stages of star formation.

The column densities of para-H_2CO and the fractional abundances of X(para-H_2CO) with corresponding H_2 column density, spatial density $n(H_2)$, kinetic temperature T_{kin}(para-H_2CO 4_{22}–3_{21}/4_{04}–3_{03}), bolometric luminosity, clump mass, and luminosity-to-mass (L_{bol}/M_{clump}) ratio are shown in Figure 6. It is apparent that the para-H_2CO column density increases proportionally to the H_2 column density, gas kinetic temperature, bolometric luminosity, and L_{bol}/M_{clump} ratio in the massive clumps. The fractional abundance of X(para-H_2CO) remains stable with increasing H_2 column density, spatial density, and mass of clump (Fig. 6). Nevertheless, the scatter in X(para-H_2CO) amounts to 0.1–1.2×10^{-9}, i.e. to a factor of ~10. The stable (relative to other molecular species; e.g., Tang et al. 2017b) para-H_2CO fractional abundances as a function of $N(H_2)$ indicate that H_2CO is a reliable tracer of the H_2 column density.

The luminosity-to-mass ratio is a good evolutionary tracer for massive and dense cluster-progenitor clumps (Molinari et al. 2008, 2016; Liu et al. 2013; Ma et al. 2013; Giannetti et al. 2017). The fractional abundance of X(para-H_2CO) shows a weak increasing trend with kinetic temperature, bolometric luminosity, and L_{bol}/M_{clump} ratio (see Fig. 6). The H_2CO abundances seem to increase with the evolutionary stage of massive clumps. Similar trends were seen in the massive star formation regions studied by Gerner et al. (2014) and Immer et al. (2014). This indicates that H_2CO abundances may be enhanced by high temperature, infrared radiation, and clump evolution, which would support a scenario in which H_2CO is increasingly released from dust grains into the gas phase during the evolution of the star-forming region.

4.2. Comparison of kinetic temperatures derived from the gas and the dust

The gas kinetic temperatures derived from the para-H_2CO (3_{21}–2_{20}/3_{03}–2_{02} and 4_{22}–3_{21}/4_{04}–3_{03}) line ratios are rather warm, ranging from 43 to >300 K with an unweighted average of

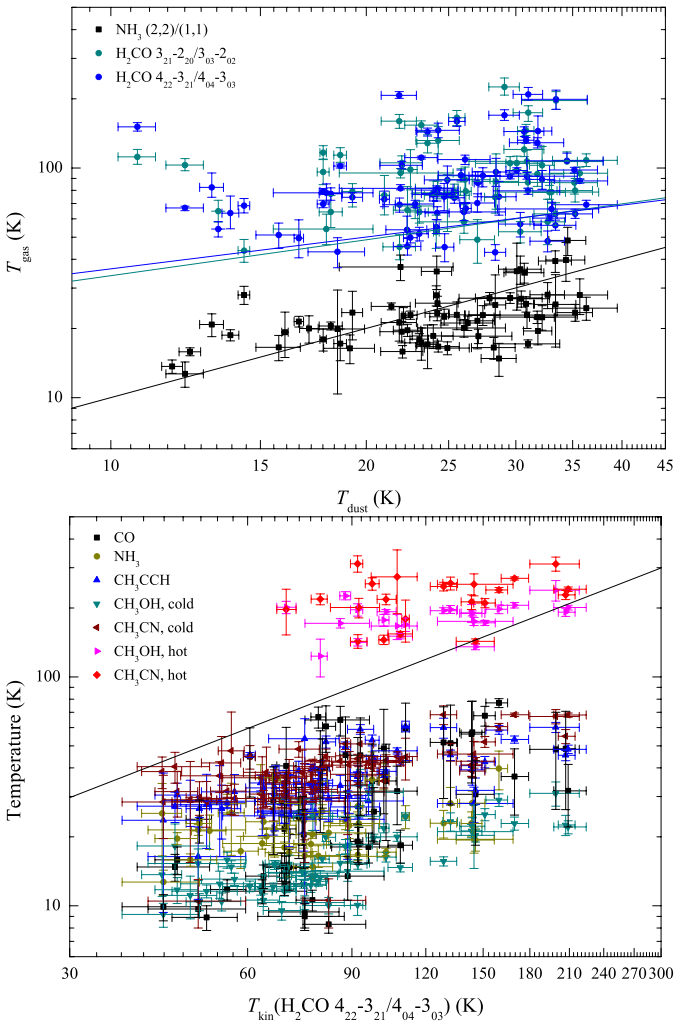

Fig. 8. Top panel: Comparison of kinetic temperatures derived from para-H_2CO (3_{21}–2_{20}/3_{03}–2_{02} and 4_{22}–3_{21}/4_{04}–3_{03}, cyan and blue points) and NH_3 (2,2)/(1,1) (black squares) ratios against the dust temperatures. NH_3 kinetic temperatures are selected from Wienen et al. (2012). The cyan and blue straight lines are the results from unweighed linear fits for gas temperatures derived from para-H_2CO (3_{21}–2_{20}/3_{03}–2_{02} and 4_{22}–3_{21}/4_{04}–3_{03}, repectively. Bottom panel: Comparisons of gas temperatures derived from para-H_2CO (4_{22}–3_{21}/4_{04}–3_{03}), CO, NH_3 (2,2)/(1,1), CH_3OH, CH_3CN, and CH_3CCH. Temperatures of CO, CH_3OH, CH_3CN, and CH_3CCH are taken from Giannetti et al. (2017). The black straight lines in both panels indicate equal temperatures.

91 ± 4 K, which agrees with the results measured with H_2CO in other massive star-forming regions and Galactic center clouds (Mangum & Wootten 1993; Hurt et al. 1996; Mangum et al. 1999; Watanabe & Mitchell 2008; Nagy et al. 2012; Ao et al. 2013; Ginsburg et al. 2016; Immer et al. 2016; Lu et al. 2017). Most of our clumps, including the detected 70 μm weak clumps, are very warm indicating that there is likely massive star formation on-going in most of our sample. The average kinetic temperatures T_{kin} are high in early evolutionary stages of the clumps (70w and IRw) (see Tab. 3), which is consistent with previous observational results measured with para-H_2CO (3–2) in star-forming regions with outflows (Tang et al. 2017a). 16 sources of our sample in early evolutionary stages have been observed in SiO (2–1) and (5–4) (Csengeri et al. 2016), SiO emission is detected in all these sources. This indicates that the dense gas

probed by H_2CO may be heated by an outflow/shock. Therefore, in early evolutionary stages of the clumps, para-H_2CO traces higher temperature gas which may be related to gas excited by star formation activities (e.g., ourflows, shocks) (Tang et al. 2017a).

Parts of our sample have been measured in NH_3 (2,2)/(1,1) by Wienen et al. (2012). We compare gas kinetic temperatures derived from para-H_2CO and NH_3 (2,2)/(1,1) against dust temperatures in Figure 8. This comparison shows that the gas temperatures determined from NH_3 (2,2)/(1,1) agree with the dust temperatures (also see Giannetti et al. 2017), but are lower than those derived from para-H_2CO (3_{21}–2_{20}/3_{03}–2_{02} and 4_{22}–3_{21}/4_{04}–3_{03}). Previous observations toward the Galactic CMZ, dense massive clumps, and star formation regions indicate that in many cases para-H_2CO (3_{21}–2_{20}/3_{03}–2_{02} and 4_{22}–3_{21}/4_{04}–3_{03}) traces a higher kinetic temperature than the NH_3 (2,2)/(1,1) transitions and the dust (Ao et al. 2013; Ott et al. 2014; Ginsburg et al. 2016; Immer et al. 2016; Tang et al. 2017a,c). The difference is likely due to the fact that the derived kinetic temperatures from NH_3 (2,2)/(1,1) may reflect an average temperature of cooler and more diffuse gas (Henkel et al. 1987; Ginsburg et al. 2016), while para-H_2CO (J = 3–2 and 4–3) ratios trace denser and hotter regions more directly associated with star formation activity (Tang et al. 2017a,c).

Temperatures toward our selected massive clumps have been measured with CO, CH_3OH, CH_3CN, and CH_3CCH (Giannetti et al. 2017). We compare gas kinetic temperatures derived from para-H_2CO (4_{22}–3_{21}/4_{04}–3_{03}), CO, CH_3OH, CH_3CN, and CH_3CCH in Figure 8. It shows that the gas temperatures determined from para-H_2CO are higher than those derived from CO, CH_3OH (cold component), CH_3CN (cold component), and CH_3CCH, but are lower than those obtained from the CH_3OH and CH_3CN hot components. This indicates that para-H_2CO (J = 3–2 and 4–3) ratios may trace dense gas in layers intermediate between those of CH_3CCH and CH_3CN (hot component), with the latter likely most closely related to recently formed massive stars.

The dust temperatures of our sample are obtained from SED fitting to Herschel HiGal data at 70, 160, 250, 350, and 500 μm and ATLASGAL data at 870 μm by König et al. (2017). The results are listed in Table A.1. The derived dust temperature range in our observed sources is 11–41 K with an unweighted average of 25 ± 7 K. Previous observations show that the temperatures derived from gas and dust are often in agreement in the active dense clumps of Galactic disk clouds (Dunham et al. 2010; Giannetti et al. 2013; Battersby et al. 2014), but do not agree in the Galactic CMZ (Güsten et al. 1981; Ao et al. 2013; Ott et al. 2014; Ginsburg et al. 2016; Immer et al. 2016; Lu et al. 2017). As in the CMZ, the gas kinetic temperatures derived from para-H_2CO show higher values than the dust temperature with no apparent correlation (correlation coefficient $R \sim 0.2$) between T_{dust} and T_{gas} (see Fig. 8).

Commonly it is expected that the gas and dust are thermally coupled in the densest regions ($n(H_2) > 10^{4.5}$ cm^{-3}) (Goldsmith 2001), because at such densities interactions between dust and gas become sufficiently frequent. The dust emission at mid-infrared (MIR) emission traces primarily warm dust components (Helou 1986). Dust temperatures derived from MIR multi-filter data agree with gas temperatures derived from multi-inversion transitions of NH_3 in external galaxies (Melo et al. 2002; Tomono et al. 2006; Ao et al. 2011; Mauersberger et al. 2003). Combining the MIR data for our sample, the fit of the warm gas emission in the SED shows a cold and a warm component (see König et al. 2017). Our dust temperatures are taken from the cold component of the SED fitted results. Dust emission at far-infrared (FIR) emission originates primarily from colder dust components that may not be directly associated with star formation activity (Schnee et al. 2009; Bendo et al. 2012; Mangum et al. 2013a), so the dust temperatures derived from FIR measurements rarely exceed 50 K in star formation regions of our Galaxy and external galaxies (e.g., Henkel et al. 1986; Gao & Solomon 2004a; Bernard et al. 2010; Mangum et al. 2013a; Guzmán et al. 2015; Merello et al. 2015; He et al. 2016; Lin et al. 2016; König et al. 2017; Yu & Xu 2016; Tang et al. 2017a; Elia et al. 2017). This suggests that the HiGal dust emission may trace colder dust components that may not be used as a proxy for dust and gas kinetic temperatures (at least traced by H_2CO) in dense regions with massive star formation activity.

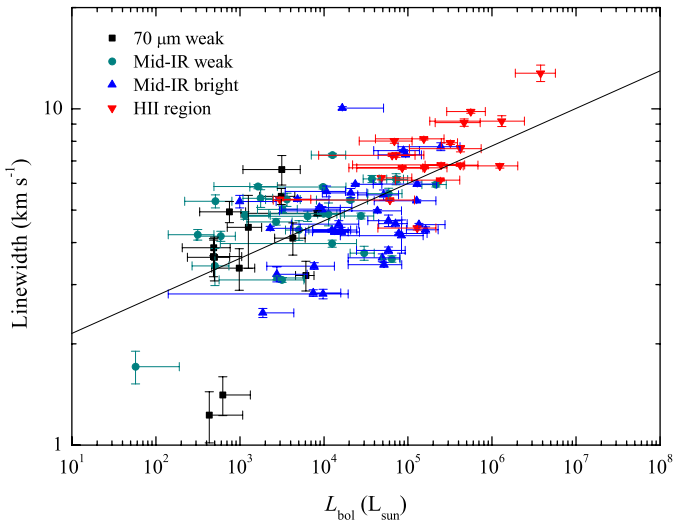

Fig. 9. The linewidth of the para-H_2CO (4_{04}–3_{03}) transition vs. bolometric luminosity of the measured sources. The straight line is the result from an unweighed linear fit.

4.3. The linewidth-luminosity relation

The observed linewidths of para-H_2CO (4_{04}–3_{03}) range from 1.2 to 12.8 km s^{-1} with an unweighted average of 5.3 ± 0.2 km s^{-1}. Using a mean unweighted kinetic temperature $T_{kin} \sim 91$ K and averaged linewidths of H_2CO, the thermal and non-thermal linewidths ($\sigma_T = \sqrt{\frac{kT_{kin}}{m_{H_2CO}}}$ and $\sigma_{NT} = \sqrt{\frac{\Delta v^2}{8\ln 2} - \sigma_T^2}$, where k is the Boltzmann constant, T_{kin} is the kinetic temperature of the gas, m_{H_2CO} is the mass of the formaldehyde molecule, and Δv is the measured FWHM linewidth of H_2CO) are 0.15 and 2.25 km s^{-1}, respectively. The thermal linewidth is significantly lower than the non-thermal linewidth. The sound speed ($a_s = \sqrt{\frac{kT_{kin}}{\mu m_H}}$, where $\mu = 2.37$ is the mean molecular weight for molecular clouds and m_H is the mass of the hydrogen atom) is ~0.54 km s^{-1} at temperature 91 K, so the Mach number (given as $M = \sigma_{NT}/a_s$) is 4.2 which agrees with the results of the high-mass clumps (mean value ~ 3.5 derived from NH_3; Wienen et al. 2012) and the Bolocam Galactic Plane Survey (BGPS) sources (mean value ~ 3.2 derived from NH_3; Dunham et al. 2011). This indicates that these massive clumps are turbulent and H_2CO linewidths are influenced strongly by supersonic non-thermal motions in our samples.

Previous observations of NH_3 (Wouterloot et al. 1988; Myers et al. 1991; Harju et al. 1993; Ladd et al. 1994; Molinari et al. 1996; Jijina et al. 1999; Wu et al. 2006; Urquhart et al. 2011, 2015), $C^{18}O$ (Saito et al. 2001; Ridge et al. 2003; Maud et al. 2015), and ^{13}CO (Wang et al. 2009; Lundquist et al. 2015) suggest that the linewidth is correlated with luminosity, which indicates the presence of a link between the formed stars and the velocity dispersion. We investigate the linewidth-luminosity relation in the case of the dense gas tracer H_2CO. We plot the linewidth-luminosity relation in Figure 9. For the linewidth of para-H_2CO (4_{04}–3_{03}) and bolometric luminosity, the least squares linear fit result is

$$\log\Delta v(\mathrm{H_2CO}\ 4_{04}\text{–}3_{03}) = (0.11 \pm 0.01) \times \log L_{\rm bol} + (0.23 \pm 0.06). \quad (3)$$

The correlation coefficient, R, is 0.64. Other transitions of H_2CO show similar $\Delta v(H_2CO)$-$L_{\rm bol}$ correlations (not shown here). The slope (0.11 ± 0.01) of the $\Delta v(H_2CO)$-$L_{\rm bol}$ correlation agrees with previous results found with $C^{18}O$ (Saito et al. 2001) and ^{13}CO (Wang et al. 2009), but is lower than that found with NH_3 (Wouterloot et al. 1988; Myers et al. 1991; Jijina et al. 1999; Wu et al. 2006; Urquhart et al. 2011, 2015). The correlation appears consistent with the idea that the internal velocity dispersion of the dense clumps can be used to determine the mass of the formed stars (Saito et al. 2001).

We also derived averaged linewidths of para-H_2CO (4_{04}–3_{03}) discriminating between the four evolutionary stages introduced in Section 2. The unweighted averaged linewidths are 3.9 ± 0.4, 4.8 ± 0.2, 4.9 ± 0.3, and 7.4 ± 0.4 km s^{-1} in 70w, IRw, IRb, and H II regions, respectively (see Tab. 3). It seems that the velocity dispersion slightly increases with the first three evolutionary stages, 70w, IRw, and IRb. A significant change appears to occur between the first three and the fourth (H II) evolutionary stage. This suggests that the more evolved and more luminous objects tend to be associated with more turbulent molecular cloud structures (Wang et al. 2009).

4.4. The non-thermal velocity dispersion-temperature relation

Previous observations of NH_3 and H_2CO (e.g., Wouterloot et al. 1988; Molinari et al. 1996; Jijina et al. 1999; Wu et al. 2006; Urquhart et al. 2011, 2015; Wienen et al. 2012; Lu et al. 2014; Immer et al. 2016; Tang et al. 2017c) suggest that the linewidth is correlated with kinetic temperature. It is suggested that the correlation between kinetic temperature and linewidth is due to a conversion of turbulent energy into heat in the Galactic central clouds (e.g., Güsten et al. 1985; Ginsburg et al. 2016; Immer et al. 2016).

Here we examine whether there is a relationship between turbulence and temperature in our massive clumps. We adopt the non-thermal velocity dispersion ($\sigma_{\rm NT}$) of para-H_2CO in good approximation as proxy for the turbulence, and the kinetic temperatures of para-H_2CO (3_{21}–2_{20}/3_{03}–2_{02} and 4_{22}–3_{21}/4_{04}–3_{03}) as the gas kinetic temperature (see Fig. 10). For the non-thermal velocity dispersion of para-H_2CO and kinetic temperature, the least squares linear fit results are listed in Table 4. The non-thermal velocity dispersion of para-H_2CO is significantly positively correlated with the gas kinetic temperature by a power-law of the form $T_{\rm kin} \propto \sigma_{\rm NT}^{0.66-1.06}$, which is consistent with results found with NH_3 and H_2CO in other star formation regions (Wouterloot et al. 1988; Molinari et al. 1996; Jijina et al. 1999; Wu et al. 2006; Urquhart et al. 2011, 2015; Wienen et al. 2012; Lu et al. 2014; Tang et al. 2017c). The gas is heated by turbulent energy according to the approximate relation $T_{\rm kin} \propto \Delta v^{0.8-1.0}$ (gas kinetic temperature measured with NH_3 and H_2CO) in molecular clouds of the Galactic center (Güsten et al. 1985; Mauersberger et al. 1987; Immer et al. 2016), which is consistent with our result (only in terms of slope, not of intercept and absolute value). All this implies that the gas may be heated by turbulent motions in our massive clumps on scales of ~0.1–1.8 pc.

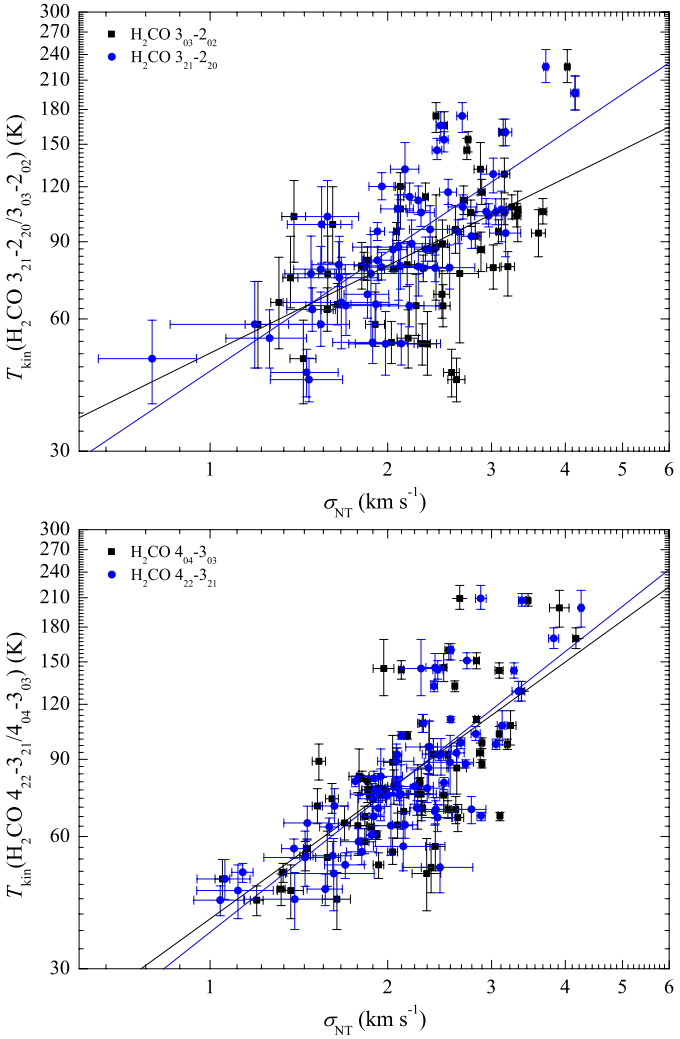

Fig. 10. Non-thermal velocity dispersion ($\sigma_{\rm NT}$) vs. gas kinetic temperature for para-H_2CO. For the top panel, gas kinetic temperatures were derived from para-H_2CO 3_{21}–2_{20}/3_{03}–2_{02} line ratios. For the bottom panel, the gas kinetic temperatures were derived from para-H_2CO 4_{22}–3_{21}/4_{04}–3_{03} line ratios. The straight lines are results from unweighed linear fits.

Table 4. Kinetic temperature vs. H_2CO non-thermal velocity dispersion.

Transition	$T_{\rm kin}$–$\sigma_{\rm NT}(H_2CO)$		
	Slope	Intercept	R
p-H_2CO 3_{03}–2_{02}	0.66 (0.15)	1.70 (0.06)	0.52
p-H_2CO 3_{21}–2_{20}	0.90 (0.11)	1.66 (0.04)	0.73
p-H_2CO 4_{04}–3_{03}	0.97 (0.12)	1.59 (0.04)	0.70
p-H_2CO 4_{22}–3_{21}	1.06 (0.10)	1.56 (0.04)	0.78

Notes. The format of the regression fits is $\log T_{\rm kin}$ = Slope × $\log\sigma_{\rm NT}(H_2CO)$ + Intercept. R is the correlation coefficient for the linear fit.

Recent para-H_2CO mapping observations of molecular clouds in the Galactic CMZ show that the warm dense gas is heated most likely by turbulence (Ao et al. 2013; Ginsburg et al. 2016; Immer et al. 2016). Following the method applied by Tang et al. (2017c) in their Equation (2),

$$3.3\times10^{-27}\, n\, \sigma_{\rm NT}^{3}\, L^{-1} = 4\times10^{-33}\, n^{2}\, T_{\rm turb}^{1/2}(T_{\rm turb}-T_{\rm dust}) + 6\times10^{-29}\, n^{1/2}\, T_{\rm turb}^{3}\, {\rm d}v/{\rm d}r, \quad (4)$$

where the gas density n is in units of cm^{-3}, the velocity gradient dv/dr is in units of $km\,s^{-1}pc^{-1}$, the one-dimensional non-thermal velocity dispersion $\sigma_{\rm NT}$ is in units of $km\,s^{-1}$, and the cloud size L is in units of pc, we determine the gas kinetic temperature caused by turbulent energy. We computed the gas kinetic temperature assuming turbulent heating dominates the heating process. We have assumed a cloud size of ~1 pc (e.g., Dunham et al. 2010, 2011; Rosolowsky et al. 2010; Urquhart et al. 2014; He et al. 2015; Wienen et al. 2015; König et al. 2017; Yuan et al. 2017), a velocity gradient dv/dr = 1 $km\,s^{-1}pc^{-1}$, the above mentioned (Sect. 4.3) averaged non-thermal velocity dispersion of 2.25 $km\,s^{-1}$ measured with H_2CO, and an averaged gas spatial density ~10^6 cm^{-3} derived from H_2CO line intensity ratios (Sect. 3.5). If the averaged dust temperature ($T_{\rm dust}$ ~ 25 K; derived from HiGal and ATLASGAL data; see Sect. 4.2) and averaged gas temperature ($T_{\rm kin}$ ~ 91 K; derived from the para-H_2CO line ratios; see Sect. 4.2) are adopted as the dust temperatures, the gas kinetic temperatures due to turbulence motions $T_{\rm turb}$, are 55 and 88 K, respectively. The obtained $T_{\rm turb}$ values are slightly lower than the averaged gas kinetic temperature ($T_{\rm kin}$ ~ 91 K) derived from the para-H_2CO line ratios. This indicates that turbulent heating significantly contributes to gas temperature in these massive clumps on scales of ~0.1–1.8 pc, which agrees with previous observational results with H_2CO in the Orion molecular cloud 1 (OMC-1; Tang et al. 2017c). Apparently, turbulent heating plays an important role in heating the dense gas in massive star-forming clumps (Pan & Padoan 2009).

4.5. Correlation of gas temperature with luminosity

Previous observations of our selected massive clump temperatures determined from CO, NH_3, CH_3CN, CH_3CCH, and CH_3OH (Wienen et al. 2012; Giannetti et al. 2014, 2017) suggest that these clumps are heated by radiation from internal massive stars. The comparison between the kinetic temperature and luminosity further helps us to understand the internal heating of embedded infrared sources upon their surrounding dense gas.

To investigate how the kinetic temperatures traced by para-H_2CO correlate with luminosity in these massive clumps, we compared the gas kinetic temperature to the bolometric luminosity obtained from MSX, WISE, Herschel HiGal and ATLASGAL data (König et al. 2017). A comparison between gas kinetic temperatures derived from para-H_2CO (3_{21}–2_{20}/3_{03}–2_{02} and 4_{22}–3_{21}/4_{04}–3_{03}) and the bolometric luminosity is shown in Figure 11. The least squares linear fit results are

$$\log L_{\rm bol} = (2.53\pm0.54)\times\log T_{\rm kin}(3_{21}-2_{20}/3_{03}-2_{02}) - (0.39\pm1.06) \quad (5)$$

and

$$\log L_{\rm bol} = (2.46\pm0.52)\times\log T_{\rm kin}(4_{22}-3_{21}/4_{04}-3_{03}) - (0.32\pm0.99), \quad (6)$$

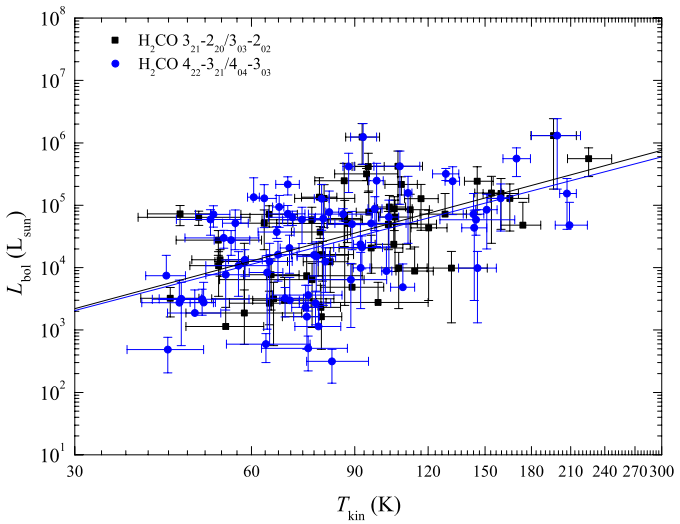

Fig. 11. The kinetic temperatures derived from para-H_2CO (3_{21}–2_{20}/3_{03}–2_{02} and 4_{22}–3_{21}/4_{04}–3_{03}, black squares and blue points) vs. bolometric luminosity. The straight lines are the results from unweighed linear fits.

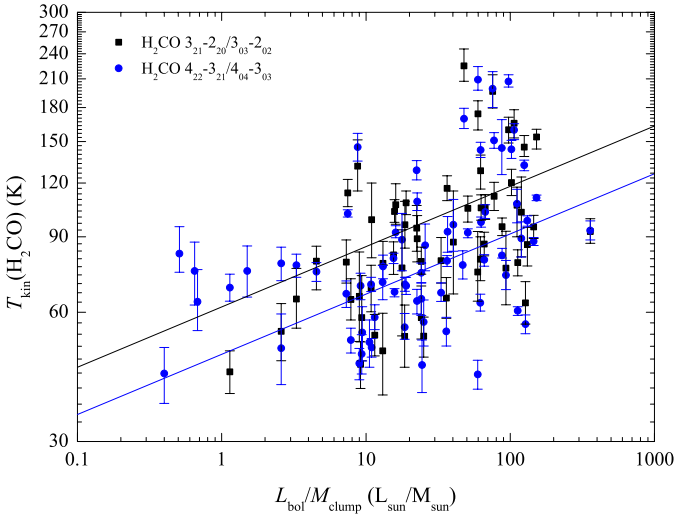

Fig. 12. The kinetic temperatures derived from para-H_2CO (3_{21}–2_{20}/3_{03}–2_{02} and 4_{22}–3_{21}/4_{04}–3_{03}, black squares and blue points) vs. luminosity-to-mass ratio $L_{\rm bol}/M_{\rm clump}$. The straight lines are the results from unweighed linear fits for clumps with $L_{\rm bol}/M_{\rm clump} \gtrsim 10$ $L_\odot/M_\odot$.

with correlation coefficients, R, of 0.53 and 0.50, respectively. It shows that higher temperatures traced by H_2CO are associated with more luminous sources. This result is expected if dense gas probed by H_2CO is illuminated or heated by massive stars inside or adjacent to the clouds. The correlations between gas temperature and bolometric luminosity are weak. The bolometric luminosity and the gas temperature derived from para-H_2CO are related by a power-law of the form $L_{\rm bol} \propto T_{\rm kin}^{2.5\pm0.5}$, where the power-law index is not very far from that of the Stefan-Boltzmann law ($L \propto T_{\rm kin}^4$). This also suggests that the dense gas is heated most likely by activity from associated massive stars.

Mapping NH_3 observations of massive star formation regions (Lu et al. 2014; Urquhart et al. 2015) shows that in some cases the gas is heated by radiation from external sources. Due to a lack of H_2CO source structure information for our sample, we cannot exclude that external heating is contributing in

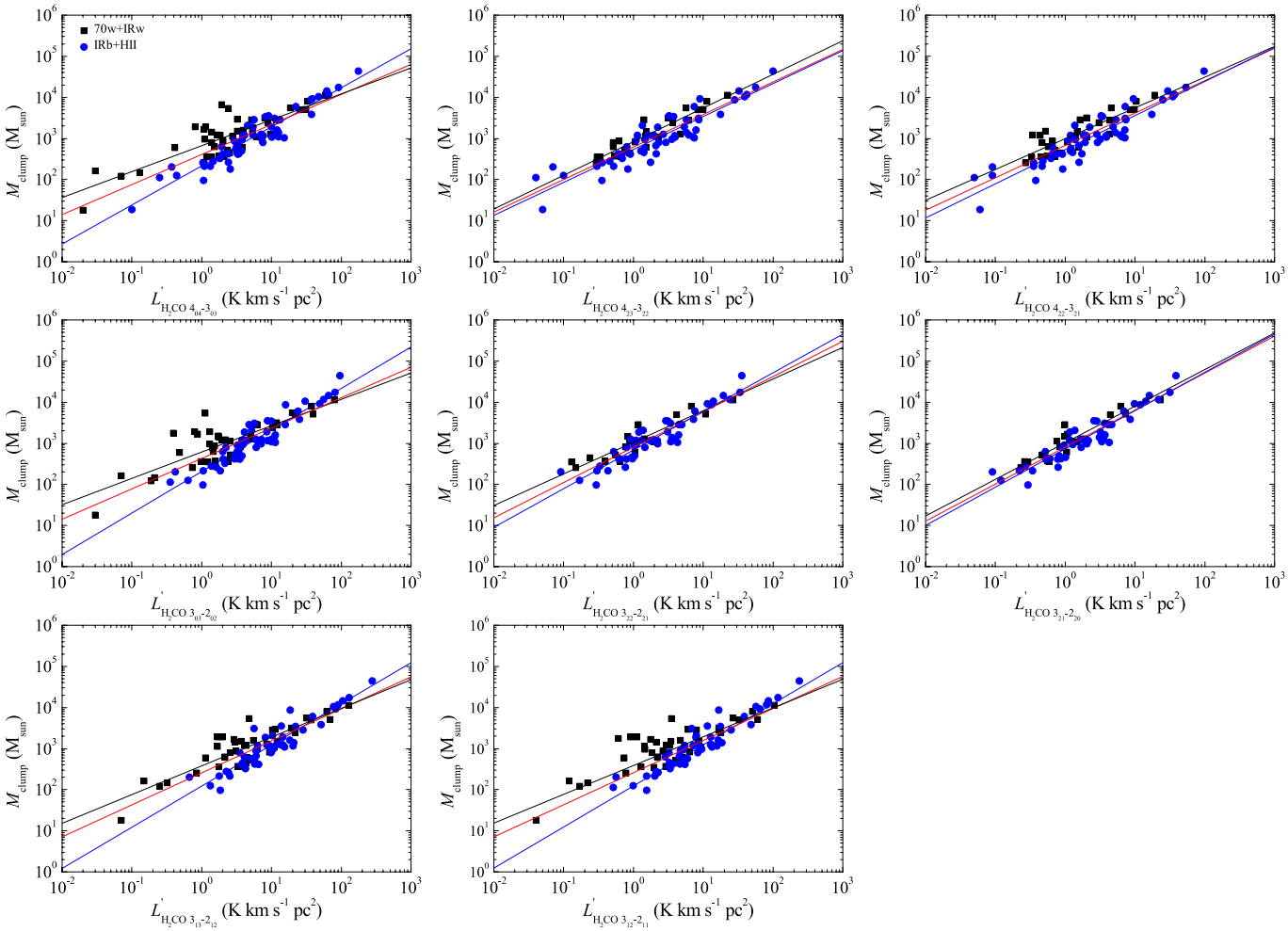

Fig. 13. M_{clump} vs. L'_{H_2CO} for eight transition lines of H_2CO. Black squares indicate clumps classified as early stage (70w and IRw) and blue circles indicate clumps classified as late stage (IRb and H II regions) (see Sect. 2 for an introduction to these sources). The black, blue, and red lines are the results from linear fits for early stage, late stage, and all sources, respectively.

some sources of our sample. Therefore, a detailed mapping study of our sample's temperature structure using formaldehyde is needed. We intend to map a part of our sample with formaldehyde to reveal details of the gas heating mechanism in the future.

4.6. Gas temperature and clump evolution

To investigate whether the kinetic temperatures traced by para-H_2CO are influenced by massive young stellar objects (YSOs) at different evolutionary stages, we derive averaged kinetic temperatures obtained from the para-H_2CO (4_{22}–3_{21}/4_{04}–3_{03}) ratios for the four evolutionary stages outlined in Section 2. The unweighted average kinetic temperatures T_{kin} are 52 ± 6, 73 ± 4, 81 ± 6, and 110 ± 8 K in 70w, IRw, IRb, and H II regions, respectively (see Tab. 3). From this it is clear that the averaged gas kinetic temperature increases with the evolutionary stage, which confirms the trends measured with CO, NH_3, CH_3CN, CH_3CCH, CH_3OH, and dust emission in our and other massive star-forming clumps (Giannetti et al. 2014, 2017; Guzmán et al. 2015; Molinari et al. 2016; He et al. 2016; Yu & Xu 2016; König et al. 2017; Yuan et al. 2017; Elia et al. 2017). It indicates that the gas temperature probed by para-H_2CO is related to the evolution of the clumps.

As mentioned in Section 4.1, the luminosity-to-mass ratio, L_{bol}/M_{clump}, is a good evolutionary tracer for massive and dense cluster-progenitor clumps, which defines a continuous evolutionary sequence in time. We plot the relation between kinetic temperature derived from para-H_2CO (3_{21}–2_{20}/3_{03}–2_{02} and 4_{22}–3_{21}/4_{04}–3_{03}) ratios and L_{bol}/M_{clump} ratios in Figure 12. The plot shows that the kinetic temperature traced by para-H_2CO is indeed a rising function of the luminosity-to-mass ratio, which is consistent with results found from CH_3CN, CH_3CCH, and CH_3OH in massive star-forming clumps (Molinari et al. 2016; Giannetti et al. 2017).

It seems that massive stars reach the main sequence above a threshold of $L_{bol}/M_{clump} \sim 10\,L_\odot/M_\odot$ (Giannetti et al. 2017), thus strongly increasing their energy output. $L_{bol}/M_{clump} \gtrsim 10\,L_\odot/M_\odot$ clumps are associated with IRb and H II regions in our sample (also see Giannetti et al. 2017), indicating late evolutionary stages (see Tab. A.1). For $L_{bol}/M_{clump} \gtrsim 10\,L_\odot/M_\odot$, the gas temperature and the luminosity-to-mass ratio are related by power-laws of the form

$$\log T_{kin}(3_{21}-2_{20}/3_{03}-2_{02}) = (0.14 \pm 0.05) \times \log(L_{bol}/M_{clump}) + (1.79 \pm 0.09) \quad (7)$$

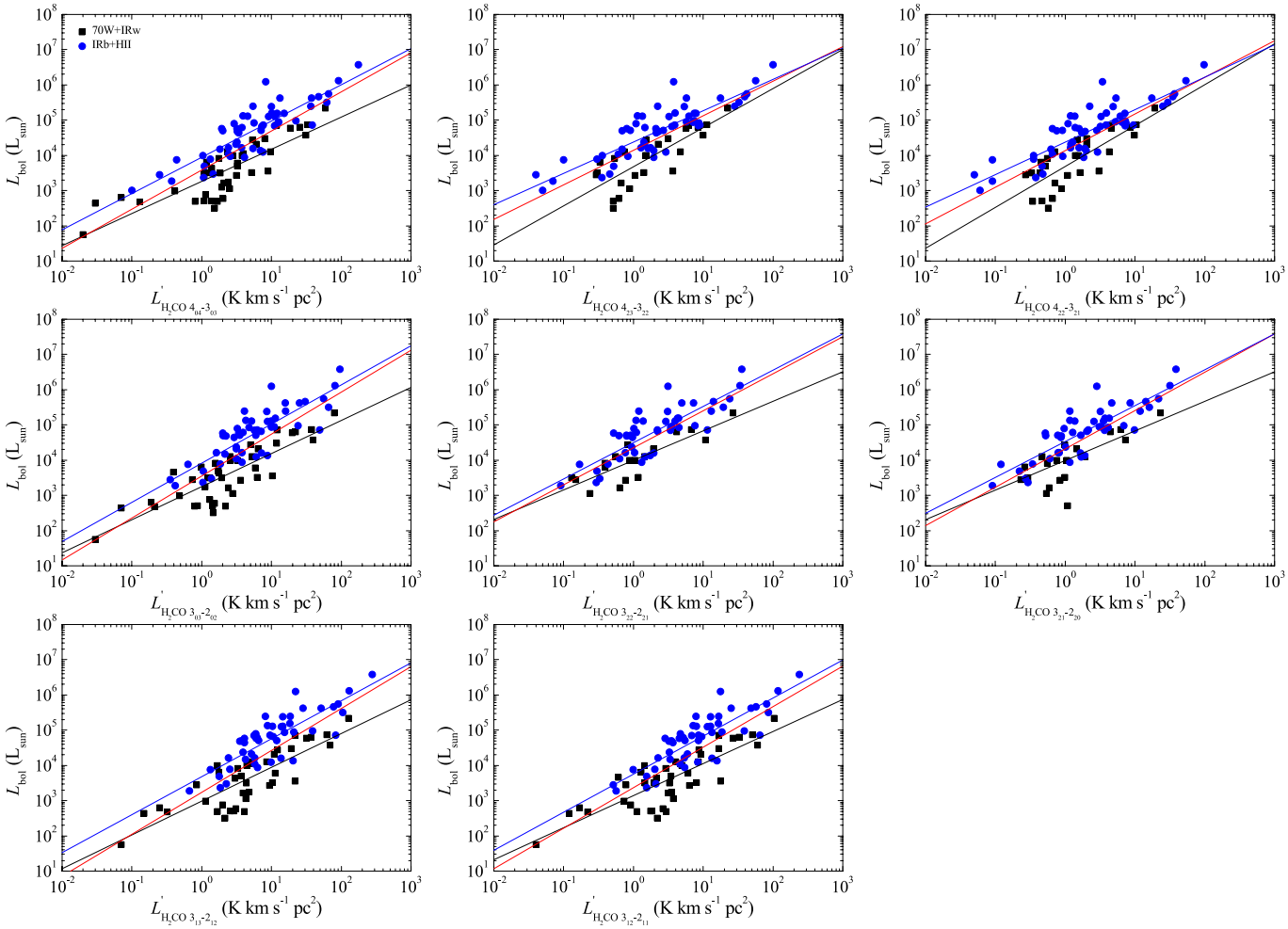

Fig. 14. L_{bol} vs. L'_{H_2CO} for eight transition lines of H_2CO. Black squares indicate clumps classified as early stage (70w and IRw) and blue circles indicate clumps classified as late stage (IRb and H II regions). The black, blue, and red lines are the results from linear fits for early stage, late stage, and all sources, respectively.

and

$$\log T_{kin}(4_{22}-3_{21}/4_{04}-3_{03}) = (0.16 \pm 0.04) \times \log(L_{bol}/M_{clump}) + (1.68 \pm 0.08), \quad (8)$$

with correlation coefficients, R, of 0.37 and 0.45, respectively. The power-law indices are consistent with those derived from CH_3CN, CH_3CCH, and CH_3OH in our and other massive clumps ($T \propto (L_{bol}/M_{clump})^{0.12-0.22}$, Molinari et al. 2016; Giannetti et al. 2017). A correlation between gas temperature and L_{bol}/M_{clump} ratio indicates that the dense gas appears to be heated by the newly formed massive stars during the late evolutionary stages of clumps. $L_{bol}/M_{clump} < 10\,L_\odot/M_\odot$ clumps are well associated with 70w and IRw indicating earlier evolutionary stages. For these sources the relation of gas temperature with the L_{bol}/M_{clump} ratio does not follow the above trend. The temperature in these sources may not yet be greatly affected by the gas which is heated by internal power sources (Molinari et al. 2016). Instead it may be related to gas excited by star formation activities e.g., outflows and shocks (Tang et al. 2017a).

4.7. Comparisons of H_2CO luminosity, bolometric luminosity, and clump mass

The line luminosities of dense molecular gas tracers (e.g., HCN, CS, and HCO^+) are found to be approximately linearly correlated with far infrared luminosities ($L_{FIR} \propto L_{molecule}$) in both Galactic dense clumps and galaxies (Gao & Solomon 2004a,b; Wu et al. 2005, 2010; Schenck et al. 2011; Ma et al. 2013; Zhang et al. 2014; Liu et al. 2016; Stephens et al. 2016), which indicates a link between star formation rate (SFR) represented by infrared luminosities and dense molecular gas mass indicated by molecular line luminosities. Line luminosities of dense molecular gas (e.g., HCN, CS, HCO^+, N_2H^+, SO) appear to be linearly related to the mass of dense gas most relevant to star formation (Wu et al. 2010; Reiter et al. 2011; Liu et al. 2016).

Observations of H_2CO K-doublet transitions ($\Delta J = 0$, $\Delta K_a = 0$, $\Delta K_c = \pm 1$) in our Galaxy and external galaxies show that H_2CO traces a denser, more compact, component of molecular clouds than low-excitation transitions of CO or HCN (Mangum et al. 1993, 2008, 2013b). Our selected H_2CO transitions may have similar characteristics. The critical densities of H_2CO 3_{13}-2_{12}, 3_{12}-2_{11}, 3_{03}–2_{02}, and 4_{04}–3_{03} transitions are $\sim 4\times10^5$, $\sim 6\times10^5$, $\sim 6\times10^5$, and $\sim 1\times10^6$ cm^{-3} (at kinetic temperature 50 K; Shirley 2015), respectively. Following Wu et al.

Table 5. Clump mass and bolometric luminosity vs. H_2CO line luminosity.

Transition	Sample	M_{clump}-L'_{H_2CO}			L_{bol}-L'_{H_2CO}		
		Slope	Intercept	R	Slope	Intercept	R
o-H_2CO 3_{13}–2_{12}	70w+IRw	0.70 (0.06)	2.57 (0.06)	0.88	0.96 (0.11)	2.98 (0.10)	0.82
	IRb+H II	0.99 (0.05)	2.09 (0.06)	0.93	1.10 (0.10)	3.66 (0.12)	0.84
	all	0.78 (0.05)	2.40 (0.05)	0.88	1.19 (0.09)	3.24 (0.10)	0.80
o-H_2CO 3_{12}–2_{11}	70w+IRw	0.63 (0.07)	2.71 (0.06)	0.83	0.91 (0.10)	3.14 (0.09)	0.82
	IRb+H II	0.98 (0.05)	2.17 (0.06)	0.94	1.08 (0.10)	3.75 (0.11)	0.84
	all	0.72 (0.05)	2.53 (0.05)	0.84	1.16 (0.09)	3.37 (0.09)	0.81
p-H_2CO 3_{03}–2_{02}	70w+IRw	0.64 (0.07)	2.79 (0.06)	0.82	0.94 (0.10)	3.25 (0.08)	0.83
	IRb+H II	1.01 (0.06)	2.32 (0.05)	0.93	1.11 (0.11)	3.92 (0.10)	0.83
	all	0.74 (0.05)	2.63 (0.04)	0.84	1.19 (0.09)	3.55 (0.08)	0.81
p-H_2CO 3_{22}–2_{21}	70w+IRw	0.77 (0.07)	3.02 (0.05)	0.93	0.84 (0.13)	3.99 (0.08)	0.85
	IRb+H II	0.94 (0.05)	2.84 (0.03)	0.94	1.03 (0.10)	4.49 (0.07)	0.83
	all	0.86 (0.04)	2.91 (0.03)	0.93	1.05 (0.09)	4.35 (0.06)	0.82
p-H_2CO 3_{21}–2_{20}	70w+IRw	0.89 (0.08)	3.01 (0.04)	0.93	0.95 (0.20)	3.90 (0.11)	0.75
	IRb+H II	0.93 (0.05)	2.86 (0.03)	0.94	1.02 (0.10)	4.51 (0.06)	0.84
	all	0.90 (0.04)	2.91 (0.03)	0.93	1.09 (0.11)	4.32 (0.07)	0.79
p-H_2CO 4_{04}–3_{03}	70w+IRw	0.63 (0.07)	2.82 (0.05)	0.83	0.91 (0.10)	3.26 (0.08)	0.83
	IRb+H II	0.95 (0.05)	2.33 (0.04)	0.94	1.03 (0.08)	3.95 (0.08)	0.86
	all	0.73 (0.05)	2.61 (0.04)	0.85	1.11 (0.08)	3.59 (0.07)	0.82
p-H_2CO 4_{23}–3_{22}	70w+IRw	0.82 (0.07)	2.92 (0.04)	0.93	1.11 (0.17)	3.67 (0.10)	0.80
	IRb+H II	0.80 (0.05)	2.73 (0.04)	0.92	0.89 (0.07)	4.38 (0.06)	0.86
	all	0.79 (0.04)	2.79 (0.03)	0.91	0.98 (0.09)	4.15 (0.06)	0.79
p-H_2CO 4_{22}–3_{21}	70w+IRw	0.75 (0.09)	2.99 (0.05)	0.86	1.16 (0.17)	3.68 (0.09)	0.80
	IRb+H II	0.83 (0.05)	2.73 (0.04)	0.92	0.92 (0.08)	4.38 (0.06)	0.86
	all	0.79 (0.05)	2.83 (0.03)	0.89	1.04 (0.09)	4.13 (0.06)	0.80

Notes. The format of the regression fits is $\log L_{bol}$ (or $\log M_{clump}$) = Slope × $\log L'_{H_2CO}$ + Intercept. R is the correlation coefficient for the linear fit.

(2005) and assuming Gaussian brightness distributions for the sources and a Gaussian beam, H_2CO line luminosities L'_{H_2CO} can be derived with

$$L'_{H_2CO} = 23.5 \times 10^{-6} \times D^2 \times \left(\frac{\pi \times \theta_s^2}{4\ln 2}\right) \times \left(\frac{\theta_s^2 + \theta_{beam}^2}{\theta_s^2}\right) \times \int T_{mb} dV. \quad (9)$$

Here D is the distance in kpc from König et al. (2017), and θ_s and θ_{beam} are the sizes of the line emission source and of the beam in arcsecond. As described in Section 3.5, we assume that the extent of the H_2CO emission is the same as that of the 870 μm dust emission derived from Csengeri et al. (2014). The resulting L'_{H_2CO} values are listed in Table A.7.

We present the correlations between clump masses and H_2CO luminosities in Figure 13. The power-law fitted results are listed in Table 5. These show that the M_{clump}-L'_{H_2CO} relations are strongly correlated, with correlation coefficients ranging from 0.84 to 0.93 for different H_2CO transitions. The power-law correlations of M_{clump}-L'_{H_2CO} are found to be slightly sublinear, and are consistent with results of e.g., HCN, CS, HCO^+, N_2H^+, and SO found in massive dense clumps (Wu et al. 2010; Reiter et al. 2011; Liu et al. 2016). This indicates that L'_{H_2CO} of our observed eight transitions provides good tracers for the mass of dense gas and confirms that $L'_{molecule}$ of dense molecular tracers does reliably probe the mass of dense molecular gas.

The L_{bol}-L'_{H_2CO} relations are plotted in Figure 14. We fit power-law relations of L_{bol}-L'_{H_2CO} for eight different H_2CO transitions. The fitted results are listed in Table 5. The bolometric luminosities and the H_2CO luminosities are related with a slope range of 0.98–1.19 and correlation coefficients ranging from 0.79 to 0.82 for different H_2CO transitions. Considering the uncertainties, the correlations are nearly linear. The correlations of L_{bol}-L'_{H_2CO} for different H_2CO transitions are consistent with previous observational results of e.g., HCN, CS, HCO^+, SiO, HC_3N, C_2H in massive dense clumps (Wu et al. 2005, 2010; Ma et al. 2013; Liu et al. 2016; Stephens et al. 2016). This indicates that the mass of dense molecular gas traced by the H_2CO line luminosity is well correlated with star formation.

Observations of dense clumps show that their evolutionary stage impacts the L_{IR}-$L'_{molecule}$ relation (Liu et al. 2016; Stephens et al. 2016). We distinguish two evolutionary classes of clumps in their early stage (70w and IRb) and late stage (IRb and H II regions), respectively, in Figure 14, and the power-law fitted results are listed in Table 5. Considering uncertainties of the fitted slopes of L_{bol}-L'_{H_2CO} correlations, we find approximately similar linear correlations of L_{bol}-L'_{H_2CO} for different transitions in both evolutionary stages of the clumps. This suggests that the L_{IR}-L'_{H_2CO} relations are only weakly influenced by the evolutionary stage of the clumps in our sample. We also compared the M_{clump}-L'_{H_2CO} relations in the two evolutionary stages in Figure 13, and the power-law fitted results are listed in Table 5. Apparently, clumps in an early stage are closer to sublinear (slopes of 0.63–0.89) and clumps in a late stage tend to exhibit more linear slopes (0.80 to 1.01). For the early stage, the M_{clump}-L'_{H_2CO} data show a larger scatter (see Fig. 13). This may be due to some clumps with lower luminosity ($<10^3$ $L_\odot$) which are likely in an early evolutionary stage with large derived uncertainties of the mass of the clump. The M_{clump}-L'_{H_2CO} is found to be strongly correlated, with correlation coefficients ranging from 0.92 to 0.94 in the late stages of clumps. This indicates that L'_{H_2CO} (J = 3–2 and 4–3) traces well the mass of warm dense

molecular gas associated with bright infrared emission and H II regions in massive star-forming clumps.

5. Summary

We have measured the kinetic temperature and spatial density with H_2CO ($J = 4$–3) and (3–2) rotational transitions and compare the derived temperatures with values obtained from NH_3, with dust emission, and with linewidth and bolometric luminosity for the ATLASGAL TOP100 massive star-forming clumps at various evolutionary stages using the 12-m APEX telescope. The main results are the following:

1. Using the RADEX non-LTE model, we derive the gas kinetic temperature and spatial density, modeling the measured para-H_2CO 3_{21}–2_{20}/3_{03}–2_{02}, 4_{22}–3_{21}/4_{04}–3_{03}, and 4_{04}–3_{03}/3_{03}–2_{02} ratios. The gas kinetic temperatures derived from the para-H_2CO 4_{22}–3_{21}/4_{04}–3_{03} and 3_{21}–2_{20}/3_{03}–2_{02} line ratios are very warm, ranging from 43 to >300 K with an unweighted average of 91 ± 4 K. Spatial densities of molecular gas derived from the para-H_2CO 4_{04}–3_{03}/3_{03}–2_{02} line ratios yield 0.6–8.3×10^6 cm^{-3} with an unweighted average of $1.5\,(\pm0.1) \times 10^6$ cm^{-3}.
2. The fractional abundance X(para-H_2CO) does not vary considerably during the various stages of massive star formation, ranging from 1.0×10^{-10} to 1.2×10^{-9} with an average of $3.9\,(\pm0.2) \times 10^{-10}$, confirming that H_2CO does reliably trace the H_2 column density.
3. The spatial densities traced by H_2CO do not vary significantly with the evolutionary stage of massive clumps. This may indicate that the density structure does not evolve significantly as the star formation proceeds.
4. A comparison of kinetic temperatures derived from para-H_2CO, NH_3 (2,2)/(1,1), and the dust emission indicates that para-H_2CO traces a distinctly higher temperature than the NH_3 (2,2)/(1,1) transitions and the dust.
5. The H_2CO linewidths correlate with the bolometric luminosities and increase with the evolutionary stage of the clumps, which suggests that high luminosities tend to be associated with more turbulent molecular cloud structures.
6. The non-thermal velocity dispersion of H_2CO is positively correlated with the gas kinetic temperature, which indicates that the dense gas may be heated by dissipation of turbulent energy in those massive clumps.
7. A weak positive correlation between gas temperature and bolometric luminosity suggests that the gas might be heated by the activity of the embedded young massive stars.
8. The average gas kinetic temperature clearly increases with the evolutionary stage of the massive clumps. For $L_{\rm bol}/M_{\rm clump} \gtrsim 10\,{\rm L}_\odot/{\rm M}_\odot$, we find a rough correlation between gas kinetic temperature and $L_{\rm bol}/M_{\rm clump}$ ratio, which traces the evolutionary stage of the massive clumps (Molinari et al. 2016; Giannetti et al. 2017).
9. The strong correlations between H_2CO line luminosities and clump masses are approximately linear during the late evolutionary stages of clumps, which indicates that $L_{\rm H_2CO}$ ($J = 3$–2) and (4–3) reliably trace the mass of warm dense molecular gas associated with bright infrared emission and H II regions. During the earlier stages of evolutionary, the correlation may be slightly sublinear. The $M_{\rm clump}$-$L'_{\rm H_2CO}$ correlation appears to be influenced by the evolutionary stage of the clumps.
10. H_2CO line luminosities are nearly linearly correlated with bolometric luminosities over about four orders of magnitude in $L_{\rm bol}$ of our massive clumps, suggesting that the mass of dense molecular gas traced by the H_2CO line luminosity is well correlated with star formation. The $L_{\rm bol}$-$L'_{\rm H_2CO}$ relation seems to be weakly affected by the evolutionary stage of the clumps.

Acknowledgements. The authors are grateful for the valuable comments of the referee Jeff Mangum. We thank the staff of the APEX telescope for their assistance in observations. We also thank Nina Brinkmann for her help of data calibration. This work acknowledges support by The National Natural Science Foundation of China under grant 11433008, The Program of the Light in China's Western Region (LCRW) under grant XBBS201424, and The National Natural Science Foundation of China under grant 11373062. This work was partially carried out within the Collaborative Research Council 956, subproject A6, funded by the Deutsche Forschungsgemeinschaft (DFG). C.H. acknowledges support by a Chinese Academy of Sciences President's International Fellowship Initiative for visiting scientists (2017VMA0005). This research has used NASA's Astrophysical Data System (ADS).

References

Ao, Y., Henkel, C., Braatz, J. A., et al. 2011, A&A, 529, 154
Ao, Y., Henkel, C., Menten, K. M., et al. 2013, A&A, 550, 135
Battersby, C., Bally, J., Dunham, M., Ginsburg, A., et al. 2014, ApJ, 786, 116
Bendo, G. J., Boselli, A., Dariush, A., et al. 2012, MNRAS, 419, 1833
Bernard, J.-Ph., Paradis, D., Marshall, D. J., et al. 2010, A&A, 518, 88
Bieging, J. H., Wilson, T. L., & Downes, D. 1982, A&AS, 49, 607
Contreras, Y., Schuller, F., Urquhart, J. S., et al. 2013, A&A, 549, 45
Csengeri, T., Leurini, S., Wyrowski, F., et al. 2016, A&A, 586, 149 (Paper II)
Csengeri, T., Urquhart, J. S., Schuller, F., et al. 2014, A&A, 565, 75.
Dickens, J. E., & Irvine, W. M. 1999, ApJ, 518, 733
Downes, D., Wilson, T. L., Bieging, J., & Wink, J. 1980, A&AS, 40, 379
Dunham, M. K., Rosolowsky, E., Evans, N. J. II., et al. 2010, ApJ, 717, 1157
Dunham, M. K., Rosolowsky, E., Evans, N. J. II., et al. 2011, ApJ, 741, 110
Elia, D., Molinari, S., Schisano, E., et al. 2017, MNRAS, 471, 100
Gao, Y., & Solomon, P. M. 2004a, ApJ, 606, 271
Gao, Y., & Solomon, P. M. 2004b, ApJS, 152, 63
Gerner, T., Beuther, H., Semenov, D., et al. 2014, A&A, 563, 97
Giannetti, A., Brand, J., Sánchez-Monge, Á., et al. 2013, A&A, 556, 16
Giannetti, A., Leurini, S., Wyrowski, F., et al. 2017, A&A, 603, 33 (Paper V)
Giannetti, A., Wyrowski, F., Brand, J., et al. 2014, A&A, 570, 65 (Paper I)
Ginsburg, A., Bally, J., Battersby, ., Youngblood, A., et al. 2015, A&A, 573, 106
Ginsburg, A., Darling, J., Battersby, et al. 2011, ApJ, 736, 149
Ginsburg, A., Goddi, C., Kruijssen, J. D., et al. 2017, ApJ, 842, 92
Ginsburg, A., Henkel, C., Ao, Y., Riquelme, D., et al. 2016, A&A, 586, 50
Goldsmith, P. F. 2001, ApJ, 557, 736
Gong, Y., Henkel, C., Spezzano, S., et al. 2015a, A&A, 574, 56
Gong, Y., Henkel, C., Thorwirth, S., et al. 2015b, A&A, 581, 48
Guo, W. H., Esimbek, J., Tang, X. D., et al. 2016, Ap&SS, 361, 264
Güsten, R., & Henkel, C. 1983, A&A, 125, 136
Güsten, R., Walmsley, C. M., & Pauls, T. 1981, A&A, 103, 197
Güsten, R., Walmsley, C. M., Ungerechts, H., et al. 1985, A&A, 142, 381
Guzmán, A. E., Sanhueza, P., Contreras, Y., et al. 2015, ApJ, 815, 130
Guzmán, V., Pety, J., Goicoechea, J. R., et al. 2011, A&A, 534, 49
Harju, J., Walmsley, C. M., & Wouterloot, J. G. A. 1993, A&AS, 98, 51
He, Y. X., Zhou, J. J., Esimbek, J., et al. 2015, MNRAS, 450, 1926
He, Y. X., Zhou, J. J., Esimbek, J., et al. 2016, MNRAS, 461, 2288
Helou, G. 1986, ApJL, 311, L33
Henkel, C., Baan, W. A., & Mauersberger, R. 1991, A&ARv, 3, 47
Henkel, C., Walmsley, C. M., & Wilson, T. L. 1980, A&A, 82, 41
Henkel, C., Wilson, T. L., & Mauersberger, R. 1987, A&A, 182, 137
Henkel, C., Wilson, T. L., Walmsley, C. M., & Pauls, T. 1983, A&A, 127, 388
Henkel, C., Wouterloot, J. G. A., & Bally, J. 1986, A&A, 155, 193
Hurt, R., Barsony, M., & Wootten, A. 1996, ApJ, 456, 686
Immer, K., Galván-Madrid, R., König, C., et al. 2014, A&A, 572, 63
Immer. K, Kauffmann. J., Pillai. T., et al. 2016, A&A, 595, 94
Jijina, J., Myers, P. C., & Adams, Fred C. 1999, ApJS, 125, 161
Johnston, K. G., Beuther, H., Linz, H., et al. 2014, A&A, 568, 56
Johnstone, D., & Bally, J., 1999, ApJ, 510L, 49
Jørgensen, J. K., Schöier, F. L., & van Dishoeck, E. F. 2005, A&A, 437, 501
Kahane, C., Lucas, R., Frerking, M. A., et al. 1984, A&A, 137, 211
Kim, W. J., Wyrowski, F., Urquhart, J. S., et al. 2017, A&A, 602, 37 (Paper IV)
König, C., Urquhart, J. S., Csengeri, T., et al. 2017, A&A, 599, 139 (Paper III)
Lada, C. J., Lombardi, M., & Alves, J. F. 2010, ApJ, 724, 687
Ladd, E. F., Myers, P. C., & Goodman, A. A. 1994, ApJ, 433, 117
Lin, Y. X, Liu, H. B., Li, D., et al., 2016, ApJ, 828, 32
Lindberg, J. E., Jørgensen, J. K., Watanabe, Y., et al. 2015, A&A, 584, 28
Liu, T., Kim, K., Yoo, H., et al. 2016, ApJ, 829, 59

Liu, T., Wu, Y., & Zhang, H. 2013, ApJ, 775L, 2
Lu, X., Zhang, Q., Kauffmann, J., et al. 2017, ApJ, 839, 1
Lu, X., Zhang, Q., Liu, H. B., Wang, J., & Gu, Q., 2014, ApJ, 790, 84
Lundquist, M. J., Kobulnicky, H. A., Kerton, C. R., et al. 2015, ApJ, 806, 40
Ma, B., Tan, J. C., & Barnes, P. J. 2013, ApJ, 779, 79
Mangum, J. G., Darling, J., Henkel, C., et al. 2013a, ApJ, 779, 33
Mangum, J. G., Darling, J., Henkel, C., & Menten, K. M. 2013b, ApJ, 766, 108
Mangum, J. G., Darling, J., Menten, K. M., & Henkel, C. 2008, ApJ, 673, 832
Mangum, J. G., & Wootten, A. 1993, ApJS, 89, 123
Mangum, J. G., Wootten, A., & Barsony, M. 1999, ApJ, 526, 845
Mangum, J. G., Wootten, A., & Plambeck, R. L. 1993, ApJ, 409, 282
Maud, L. T., Lumsden, S. L., Moore, T. J., et al. 2015, MNRAS, 452, 637
Mauersberger, R., Henkel, C., Weiß, A., et al. 2003, A&A, 403, 561
Mauersberger, R., Henkel, C., & Wilson, T. L. 1987, A&A, 173, 352
Mauersberger, R., Henkel, C., Wilson, T. L., et al. 1986, A&A, 162, 199
Melo, V. P., Pérez García, A. M., Acosta-Pulido, et al. 2002, ApJ, 574, 709
Merello, M., Evans, N. J. II., Shirley, Y. L. et al. 2015, ApJS, 218, 1
McCauley, P., Mangum, J. G., & Wootten, A. 2011, ApJ, 742, 58
Mitchell, G. F., Johnstone, D., Moriarty-Schieven, G., et al. 2001, ApJ, 556, 215
Molinari, S., Brand, J., Cesaroni, R., & Palla, F. 1996, A&A, 308, 573
Molinari, S., Merello, M., Elia, D., et al. 2016, ApJ, 826, 8
Molinari, S., Pezzuto, S., Cesaroni, R., et al. 2008, A&A, 481, 345
Mueller, K. E., Shirley, Y. L., Evans, N. J., II, et al. 2002, ApJS, 143, 469
Mühle, S., Seaquist, E. R., & Henkel, C. 2007, ApJ, 671, 1579
Myers, P. C., Ladd, E. F., & Fuller, G. A. 1991, ApJ, 372, L95
Nagy, Z., van der Tak, F. F. S., Fuller, G. A., et al. 2012, A&A, 542, 6
Ott, J., Weiß, A., Staveley-Smith, L., et al. 2014, ApJ, 785, 16
Pan, L., & Padoan, P. 2009, ApJ, 692, 594
Qin, S. L., Zhao, J. H., Moran, J. M., et al. 2008, ApJ, 677, 353
Reiter, M., Shirley, Y. L., Wu, J., et al. 2011, ApJS, 195, 1
Ridge, N. A., Wilson, T. L., Megeath, S. T., et al. 2003, AJ, 126, 286
Rosolowsky, E., Dunham, M. K., Ginsburg, A. et al. 2010, ApJS, 188, 123
Saito, H., Mizuno, N., Moriguchi, Y., et al. 2001, PASJ, 53, 1037
Sasselov, D. D., & Rucinski, S. M. 1990, ApJ, 351, 578
Schenck, D. E., Shirley, Y. L., Reiter, M., & Juneau, S. 2011, AJ, 142, 94
Schnee, S., Rosolowsky, E., Foster, et al. 2009, ApJ, 691, 1754
Schuller, F., Menten, K. M., Contreras, Y., et al. 2009, A&A, 504, 415
Shirley, Y. L. 2015, PASP, 127, 299
Stephens, I. W., Jackson, J. M., Whitaker, J. S., et al. 2016, ApJ, 824, 29
Tang, X. D., Esimbek, J., Zhou, J. J., et al. 2013, A&A, 551, 28
Tang, X. D., Henkel, C., Chen, C. -H. R., et al. 2017b, A&A, 600, 16
Tang, X. D., Henkel, C., Menten, K. M., et al. 2017a, A&A, 598, 30
Tang, X. D., Henkel, C., Menten, K. M., et al. 2017c, A&A (DOI: 10.1051/0004-6361/201731849)
Tomono, D., Terada, H., & Kobayashi, N. 2006, ApJ, 646, 774
Urquhart, J. S., Figura, C. C., Moore, T. J. T., et al. 2015, MNRAS, 452, 4029
Urquhart, J. S., König, C., Giannetti, A., et al. 2017, arXiv, 1709, 00392
Urquhart, J. S., Moore, T. J. T., Csengeri, T., et al. 2014, MNRAS, 443, 1555
Urquhart, J. S., Morgan, L. K., Figura, C. C., et al. 2011, MNRAS, 418, 1689
van der Tak, F. F. S., Black, J. H., Schöier, F. L., et al. 2007, A&A, 468, 627
van der Tak, F. F. S., van Dishoeck, E. F., & Caselli, P. 2000a, A&A, 361, 327
van der Tak, F. F. S., van Dishoeck, E. F., Evans, N. J. II., & Blake, G. A. 2000b, ApJ, 537, 283
Wang, K., Wu, Y. F., Ran, L., Yu, W. T., & Miller, M. 2009, A&A, 507, 369
Watanabe, T., & Mitchell, G. 2008, AJ, 136, 1947
Wienen, M., Wyrowski, F., Menten, K. M., et al. 2015, A&A, 579, 91
Wienen, M., Wyrowski, F., Schuller, F., et al. 2012, A&A, 544, 146
Wiesenfeld, L., & Faure, A. 2013, MNRAS, 432, 2573
Wouterloot, J. G. A., Walmsley, C. M., & Henkel, C. 1988, A&A, 203, 367
Wu, J., Evans, N. J., II, Gao, Y., et al. 2005, ApJ, 635, L173
Wu, J., Evans, N. J., II, Shirley, Y. L., et al. 2010, ApJS, 188, 313
Wu, Y., Zhang, Q., Yu, W., et al. 2006, A&A, 450, 607
Yu, N., & Xu, J. 2016, ApJ, 833, 248
Yuan, J. H., Wu, Y. F., Ellingsen, S. P., et al. 2017, ApJS, 231, 11
Zhang, Z. Y., Gao, Y., Henkel, C., et al. 2014, ApJ, 784L, 31
Zylka, R., Güsten, R., Henkel, C., & Batrla, W. 1992, A&AS, 96, 525

Appendix A: Source and H_2CO parameters

Table A.1. Source parameters.

Sources	RA(J2000)	DEC(J2000)	Distance	Size	$S_{870\mu m}$	$N(H_2)$	M_{clump}	L_{bol}	T_{dust}	Note
	$h\ m\ s$	$^\circ\ '\ ''$	kpc	arcsec	Jy beam^{-1}	cm^{-2}	$M_\odot$	$L_\odot$	K	
AGAL008.684−00.367	18:06:23.03	−21:37:10.8	4.8	26	4.56	8.7×10^{22}	1.5×10^{3}	2.8×10^{4}	24.2	IRw
AGAL008.706−00.414	18:06:36.65	−21:37:16.3	4.8	36	1.02	6.1×10^{22}	1.7×10^{3}	5.0×10^{2}	11.8	IRw
AGAL010.444−00.017	18:08:44.72	−19:54:32.8	8.6	26	2.10	5.0×10^{22}	1.6×10^{3}	1.1×10^{4}	20.7	IRw
AGAL010.472+00.027	18:08:37.99	−19:51:47.7	8.6	22	33.22	4.7×10^{23}	1.0×10^{4}	4.7×10^{5}	30.5	HII
AGAL010.624−00.384	18:10:28.62	−19:55:45.5	5.0	26	31.06	3.7×10^{23}	3.8×10^{3}	4.2×10^{5}	34.5	HII
AGAL012.804−00.199	18:14:13.55	−17:55:32.0	2.4	33	31.05	3.6×10^{23}	1.9×10^{3}	2.5×10^{5}	35.1	HII
AGAL013.178+00.059	18:14:00.59	−17:28:38.5	2.4	34	3.69	7.0×10^{22}	3.7×10^{2}	8.3×10^{3}	24.2	70w
AGAL013.658−00.599	18:17:24.09	−17:22:10.2	4.5	26	3.92	6.3×10^{22}	5.7×10^{2}	2.1×10^{4}	27.4	IRb
AGAL014.114−00.574	18:18:13.03	−16:57:18.6	2.6	32	3.46	7.4×10^{22}	3.5×10^{2}	3.2×10^{3}	22.4	IRw
AGAL014.194−00.194	18:16:58.63	−16:42:16.3	3.9	28	3.29	9.5×10^{22}	8.2×10^{2}	2.7×10^{3}	18.2	IRw
AGAL014.492−00.139	18:17:22.01	−16:25:01.1	3.9	35	2.30	1.3×10^{23}	1.9×10^{3}	7.5×10^{2}	12.4	70w
AGAL014.632−00.577	18:19:14.65	−16:30:02.7	1.8	33	4.40	9.3×10^{22}	2.5×10^{2}	2.8×10^{3}	22.5	IRw
AGAL015.029−00.669	18:20:22.45	−16:11:43.8	2.0	39	16.36	2.1×10^{23}	1.2×10^{3}	1.3×10^{5}	32.9	IRb
AGAL018.606−00.074	18:25:08.22	−12:45:23.8	4.3	29	1.40	6.3×10^{22}	8.8×10^{2}	5.9×10^{2}	13.8	IRw
AGAL018.734−00.226	18:25:56.02	−12:42:49.6	12.5	29	3.64	8.0×10^{22}	7.9×10^{3}	7.3×10^{4}	21.9	IRw
AGAL018.888−00.474	18:27:07.41	−12:41:39.8	4.7	32	3.50	1.5×10^{23}	2.8×10^{3}	3.2×10^{3}	14.4	IRw
AGAL019.882−00.534	18:29:14.54	−11:50:26.0	3.7	26	6.95	1.3×10^{23}	8.0×10^{2}	1.2×10^{4}	24.2	IRb
AGAL022.376+00.447	18:30:24.06	−09:10:39.6	4.0	25	1.65	8.1×10^{22}	6.2×10^{2}	3.2×10^{2}	13.1	IRw
AGAL023.206−00.377	18:34:54.90	−08:49:19.1	4.6	24	7.35	1.6×10^{23}	1.3×10^{3}	1.3×10^{4}	22.1	IRw
AGAL024.629+00.172	18:35:35.54	−07:18:09.5	7.7	28	1.27	3.7×10^{22}	1.5×10^{3}	5.0×10^{3}	18.1	IRw
AGAL028.564−00.236	18:44:17.74	−03:59:42.5	5.5	40	1.97	1.2×10^{23}	5.4×10^{3}	1.8×10^{3}	11.7	IRw
AGAL028.861+00.066	18:43:46.04	−03:35:29.9	7.4	27	3.40	4.1×10^{22}	1.1×10^{3}	1.6×10^{5}	34.5	IRb
AGAL030.848−00.081	18:47:55.40	−01:53:35.9	4.9	31	1.57	5.2×10^{22}	1.2×10^{3}	3.1×10^{3}	16.7	70w
AGAL030.893+00.139	18:47:13.50	−01:45:07.7	4.9	33	1.57	9.9×10^{22}	1.9×10^{3}	5.0×10^{2}	11.4	70w
AGAL031.412+00.307	18:47:34.29	−01:12:44.6	4.9	23	21.55	3.7×10^{23}	3.1×10^{3}	6.9×10^{4}	26.3	HII
AGAL034.258+00.154	18:53:18.53	+01:14:57.9	1.6	26	51.03	7.0×10^{23}	8.1×10^{2}	4.8×10^{4}	31.0	HII
AGAL034.401+00.226	18:53:18.62	+01:24:40.4	1.6	32	6.27	1.3×10^{23}	2.8×10^{2}	3.0×10^{3}	22.8	HII
AGAL034.411+00.234	18:53:18.14	+01:25:23.8	1.6	25	10.26	1.8×10^{23}	2.1×10^{2}	4.8×10^{3}	26.1	IRb
AGAL034.821+00.351	18:53:38.11	+01:50:27.9	1.6	35	2.51	4.7×10^{22}	1.1×10^{2}	2.7×10^{3}	24.7	IRb
AGAL035.197−00.742	18:58:12.93	+01:40:40.6	2.2	29	11.03	1.6×10^{23}	4.6×10^{2}	2.4×10^{4}	29.5	IRb
AGAL037.554+00.201	18:59:09.90	+04:12:17.6	6.7	27	3.52	5.4×10^{22}	1.3×10^{3}	5.1×10^{4}	28.4	IRb
AGAL043.166+00.011	19:10:13.44	+09:06:15.8	11.1	27	56.59	...	4.3×10^{4}	3.8×10^{6}	34.0	HII
AGAL049.489−00.389	19:23:43.69	+14:30:31.9	5.4	24	70.24	1.1×10^{24}	1.2×10^{4}	5.6×10^{5}	29.1	HII
AGAL053.141+00.069	19:29:17.35	+17:56:21.4	1.6	26	4.39	7.9×10^{22}	9.5×10^{1}	2.3×10^{3}	25.4	IRb
AGAL059.782+00.066	19:43:10.90	+23:44:04.4	2.2	31	4.76	7.4×10^{22}	2.5×10^{2}	9.8×10^{3}	28.2	IRb
AGAL305.192−00.006	13:11:14.54	−62:47:27.0	3.8	29	3.15	5.4×10^{22}	5.2×10^{2}	1.3×10^{4}	26.1	IRw
AGAL305.209+00.206	13:11:13.34	−62:34:38.6	3.8	27	13.51	1.9×10^{23}	1.4×10^{3}	8.8×10^{4}	30.1	IRb
AGAL305.562+00.014	13:14:26.41	−62:44:25.0	3.8	27	4.23	5.3×10^{22}	4.1×10^{2}	5.2×10^{4}	33.4	IRb
AGAL305.794−00.096	13:16:34.36	−62:49:43.4	3.8	33	1.34	4.7×10^{22}	5.9×10^{2}	9.8×10^{2}	16.0	70w
AGAL309.384−00.134	13:47:22.66	−62:18:07.5	5.3	29	3.16	6.1×10^{22}	1.2×10^{3}	1.6×10^{4}	24.0	IRb
AGAL310.014+00.387	13:51:38.06	−61:39:15.1	3.6	30	3.65	4.8×10^{22}	4.2×10^{2}	5.0×10^{4}	32.2	IRb
AGAL313.576+00.324	14:20:08.33	−60:42:04.9	3.8	23	2.59	3.9×10^{22}	1.8×10^{2}	9.4×10^{3}	29.2	IRb
AGAL316.641−00.087	14:44:18.34	−59:55:15.5	1.2	24	2.30	3.2×10^{22}	1.8×10^{1}	9.9×10^{2}	30.6	IRb
AGAL317.867−00.151	14:53:16.66	−59:26:34.7	3.0	24	4.00	1.1×10^{23}	3.6×10^{2}	1.6×10^{3}	19.3	IRw
AGAL318.779−00.137	14:59:33.19	−59:00:36.8	2.8	34	2.20	4.0×10^{22}	3.6×10^{2}	6.4×10^{3}	24.9	IRw
AGAL320.881−00.397	15:14:33.14	−58:11:32.6	10.0	27	1.50	4.9×10^{22}	2.9×10^{3}	6.1×10^{3}	16.8	70w
AGAL326.661+00.519	15:45:02.80	−54:09:11.5	1.8	29	3.60	5.6×10^{22}	1.3×10^{2}	7.4×10^{3}	28.4	IRb
AGAL326.987−00.032	15:49:07.96	−54:23:05.1	4.0	25	2.40	7.1×10^{22}	4.4×10^{2}	1.1×10^{3}	17.9	IRw
AGAL327.119+00.509	15:47:33.16	−53:52:39.7	5.5	27	3.36	4.5×10^{22}	6.7×10^{2}	5.9×10^{4}	31.8	IRb
AGAL327.293−00.579	15:53:07.80	−54:37:06.4	3.1	23	49.21	7.8×10^{23}	2.8×10^{3}	8.3×10^{4}	27.9	IRb
AGAL327.393+00.199	15:50:19.15	−53:57:04.9	5.9	28	3.15	6.4×10^{22}	1.2×10^{3}	1.3×10^{4}	23.2	IRb
AGAL328.809+00.632	15:55:48.56	−52:43:07.8	3.0	25	23.19	2.6×10^{23}	1.0×10^{3}	1.6×10^{5}	36.3	HII
AGAL329.029−00.206	16:00:31.18	−53:12:39.1	11.5	35	8.82	1.8×10^{23}	1.1×10^{4}	2.2×10^{5}	23.1	IRw
AGAL329.066−00.307	16:01:09.70	−53:16:06.0	11.6	34	3.18	7.0×10^{22}	9.1×10^{3}	7.1×10^{4}	21.9	IRb
AGAL330.879−00.367	16:10:20.31	−52:06:11.2	4.2	25	16.94	2.1×10^{23}	1.6×10^{3}	1.5×10^{5}	33.4	HII
AGAL330.954−00.182	16:09:53.01	−51:54:55.0	9.3	23	45.01	5.7×10^{23}	1.7×10^{4}	1.3×10^{6}	33.0	HII
AGAL331.709+00.582	16:10:05.84	−50:50:29.0	10.5	28	3.27	7.6×10^{22}	5.1×10^{3}	3.7×10^{4}	21.0	IRw
AGAL332.094−00.421	16:16:16.56	−51:18:26.2	3.6	27	6.35	8.8×10^{22}	6.3×10^{2}	5.9×10^{4}	30.8	IRb

Table A.1. continued.

Sources	RA(J2000)	DEC(J2000)	Distance	Size	$S_{870\mu m}$	$N(H_2)$	Mass	L_{bol}	T_{dust}	Note
	h m s	° ′ ″	kpc	arcsec	Jy beam^{-1}	cm^{-2}	$M_\odot$	$L_\odot$	K	
AGAL332.826−00.549	16:20:10.65	−50:53:17.5	3.6	25	30.44	3.5×10^{23}	1.9×10^{3}	2.4×10^{5}	35.7	HII
AGAL333.134−00.431	16:21:01.89	−50:35:12.8	3.6	30	21.68	2.5×10^{23}	2.9×10^{3}	4.2×10^{5}	35.2	HII
AGAL333.284−00.387	16:21:30.34	−50:26:54.5	3.6	34	12.31	1.7×10^{23}	2.1×10^{3}	1.3×10^{5}	30.4	HII
AGAL333.314+00.106	16:19:28.52	−50:04:43.1	3.6	28	3.28	5.7×10^{22}	4.3×10^{2}	1.1×10^{4}	25.9	IRb
AGAL333.604−00.212	16:22:09.31	−50:06:02.4	3.6	33	32.08	3.1×10^{23}	3.5×10^{3}	1.2×10^{6}	41.1	HII
AGAL333.656+00.059	16:21:11.56	−49:52:16.7	5.3	33	1.56	4.7×10^{22}	1.4×10^{3}	4.3×10^{3}	17.8	70w
AGAL335.789+00.174	16:29:47.27	−48:15:51.7	3.7	28	8.25	1.5×10^{23}	1.1×10^{3}	2.1×10^{4}	24.7	IRw
AGAL336.958−00.224	16:36:17.03	−47:40:49.6	10.9	23	1.56	5.6×10^{22}	2.4×10^{3}	3.6×10^{3}	15.8	IRw
AGAL337.176−00.032	16:36:18.42	−47:23:24.9	11.0	32	2.36	5.1×10^{22}	5.6×10^{3}	5.9×10^{4}	22.3	IRw
AGAL337.258−00.101	16:36:56.41	−47:22:27.2	11.0	27	2.34	5.2×10^{22}	3.2×10^{3}	3.0×10^{4}	21.7	IRw
AGAL337.286+00.007	16:36:34.33	−47:16:48.5	9.4	34	1.18	8.4×10^{22}	6.6×10^{3}	1.3×10^{3}	10.7	70w
AGAL337.406−00.402	16:38:50.72	−47:27:59.3	3.3	26	17.21	2.3×10^{23}	1.1×10^{3}	8.5×10^{4}	31.8	HII
AGAL337.704−00.054	16:38:29.41	−47:00:38.6	12.3	25	12.71	2.3×10^{23}	1.4×10^{4}	3.2×10^{5}	25.6	HII
AGAL337.916−00.477	16:41:10.42	−47:08:04.4	3.2	24	22.86	2.8×10^{23}	1.2×10^{3}	1.3×10^{5}	34.4	IRb
AGAL338.066+00.044	16:39:28.54	−46:40:30.9	4.7	35	1.14	3.2×10^{22}	9.6×10^{2}	3.1×10^{3}	18.5	70w
AGAL338.786+00.476	16:40:21.98	−45:51:05.8	4.5	33	1.27	7.1×10^{22}	1.2×10^{3}	4.9×10^{2}	12.2	70w
AGAL338.926+00.554	16:40:34.17	−45:41:47.0	4.4	35	15.76	3.0×10^{23}	6.0×10^{3}	9.4×10^{4}	24.2	IRb
AGAL339.623−00.122	16:46:06.13	−45:36:47.6	3.0	31	2.95	4.5×10^{22}	3.2×10^{2}	1.5×10^{4}	28.7	IRb
AGAL340.374−00.391	16:50:02.57	−45:12:45.6	3.6	28	1.78	8.5×10^{22}	7.9×10^{2}	5.1×10^{2}	13.4	IRw
AGAL340.746−01.001	16:54:03.74	−45:18:46.9	2.8	29	2.46	4.0×10^{22}	2.1×10^{2}	7.7×10^{3}	27.1	IRb
AGAL340.784−00.097	16:50:15.10	−44:42:30.5	10.0	24	3.82	6.6×10^{22}	2.8×10^{3}	7.2×10^{4}	26.2	IRw
AGAL341.217−00.212	16:52:17.92	−44:26:53.5	3.7	26	4.44	7.3×10^{22}	4.9×10^{2}	1.6×10^{4}	27.0	IRb
AGAL342.484+00.182	16:55:02.06	−43:12:59.7	12.6	25	3.32	6.6×10^{22}	4.9×10^{3}	6.4×10^{4}	23.6	IRw
AGAL343.128−00.062	16:58:17.29	−42:52:08.2	3.0	27	17.67	2.4×10^{23}	1.2×10^{3}	7.2×10^{4}	30.9	HII
AGAL343.756−00.164	17:00:49.94	−42:26:12.8	2.9	24	10.39	2.0×10^{23}	6.2×10^{2}	9.9×10^{3}	24.3	IRw
AGAL344.227−00.569	17:04:07.46	−42:18:41.7	2.5	25	17.26	3.8×10^{23}	1.1×10^{3}	9.8×10^{3}	22.0	IRw
AGAL345.003−00.224	17:05:11.17	−41:29:05.1	3.0	26	16.86	2.3×10^{23}	9.7×10^{2}	6.5×10^{4}	31.0	HII
AGAL345.488+00.314	17:04:28.06	−40:46:24.4	2.2	34	14.97	2.1×10^{23}	9.3×10^{2}	6.1×10^{4}	30.7	HII
AGAL345.504+00.347	17:04:23.00	−40:44:21.6	2.3	30	9.89	1.3×10^{23}	4.2×10^{2}	4.3×10^{4}	32.7	IRb
AGAL345.718+00.817	17:03:06.23	−40:17:05.0	1.6	37	3.10	6.8×10^{22}	2.0×10^{2}	1.9×10^{3}	22.1	IRb
AGAL351.131+00.771	17:19:34.56	−35:56:46.1	1.8	32	1.10	3.1×10^{22}	1.2×10^{2}	6.3×10^{2}	18.6	70w
AGAL351.161+00.697	17:19:56.68	−35:57:52.9	1.8	30	21.23	4.7×10^{23}	1.2×10^{3}	8.8×10^{3}	21.9	IRb
AGAL351.244+00.669	17:20:18.86	−35:54:42.4	1.8	39	16.92	2.2×10^{23}	8.9×10^{2}	7.8×10^{4}	32.5	IRb
AGAL351.571+00.762	17:20:51.03	−35:35:23.2	1.3	42	1.48	4.7×10^{22}	1.6×10^{2}	4.3×10^{2}	17.0	70w
AGAL351.581−00.352	17:25:25.03	−36:12:45.4	6.8	26	24.96	4.1×10^{23}	8.7×10^{3}	2.5×10^{5}	27.1	IRb
AGAL351.774−00.537	17:26:42.55	−36:09:20.0	1.0	25	48.81	6.5×10^{23}	2.6×10^{2}	1.6×10^{4}	31.8	IRb
AGAL353.066+00.452	17:26:13.57	−34:31:55.7	0.9	28	1.37	4.1×10^{22}	1.8×10^{1}	5.7×10^{1}	17.8	IRw
AGAL353.409−00.361	17:30:26.24	−34:41:48.5	3.4	35	20.03	3.1×10^{23}	3.5×10^{3}	1.3×10^{5}	28.3	IRb
AGAL353.417−00.079	17:29:19.10	−34:32:13.1	6.1	37	0.75	2.4×10^{22}	1.8×10^{3}	4.5×10^{3}	17.1	70w
AGAL354.944−00.537	17:35:12.03	−33:30:28.9	1.9	35	1.42	3.8×10^{22}	1.5×10^{2}	4.8×10^{2}	19.1	70w

Notes. Parameters related to distance, H_2 column density, clump mass, bolometric luminosity, and dust temperature are taken from König et al. (2017). Source size representing full width to half power values of the 870 μm continuum and $S_{870\mu m}$ are selected from Csengeri et al. (2014). Last column notes are taken from König et al. (2017): 70w = 70 μm weak, IRw = mid-infrared weak, IRb = mid-infrared bright, and HII = H II region.

Table A.2. Ortho-H_2CO 3_{13}-2_{12} and 3_{12}-2_{11} spectral parameters.

Sources	ortho-H_2CO 3_{13}–2_{12}				ortho-H_2CO 3_{12}–2_{11}			
	$\int T_{mb} dv$	V_{lsr}	FWHM	T_{mb}	$\int T_{mb} dv$	V_{lsr}	FWHM	T_{mb}
	K km s^{-1}	km s^{-1}	km s^{-1}	K	K km s^{-1}	km s^{-1}	km s^{-1}	K
AGAL008.684−00.367	13.03 (0.34)	37.96 (0.10)	7.92 (0.24)	1.55	9.21 (0.12)	38.17 (0.05)	6.96 (0.10)	1.24
AGAL008.706−00.414	2.19 (0.23)	38.21 (0.27)	5.53 (0.73)	0.37	1.34 (0.10)	38.68 (0.12)	3.43 (0.29)	0.37
AGAL010.444−00.017	1.83 (0.28)	74.67 (0.44)	6.22 (1.22)	0.28	1.56 (0.13)	74.73 (0.19)	4.67 (0.46)	0.31
AGAL010.472+00.027	29.39 (0.51)	66.13 (0.08)	9.07 (0.18)	3.04	21.68 (0.24)	65.80 (0.05)	8.98 (0.11)	2.28
AGAL010.624−00.384	50.59 (0.39)	-3.49 (0.03)	7.74 (0.08)	6.14	47.96 (0.19)	-3.65 (0.01)	7.98 (0.04)	5.65
AGAL012.804−00.199	27.20 (0.34)	36.20 (0.05)	7.87 (0.11)	3.25	26.30 (0.18)	36.06 (0.03)	7.94 (0.06)	3.12
AGAL013.178+00.059	10.53 (0.32)	49.34 (0.08)	5.93 (0.22)	1.67	9.30 (0.16)	49.23 (0.05)	5.74 (0.12)	1.52
AGAL013.658−00.599	6.31 (0.34)	47.85 (0.15)	5.98 (0.40)	0.99	7.22 (0.27)	47.54 (0.13)	7.25 (0.37)	0.93
AGAL014.114−00.574	7.54 (0.17)	19.49 (0.03)	3.13 (0.09)	2.26	5.84 (0.14)	19.58 (0.03)	3.02 (0.09)	1.83
AGAL014.194−00.194	14.05 (0.57)	40.17 (0.14)	7.59 (0.40)	1.74	9.47 (0.18)	40.04 (0.05)	6.14 (0.14)	1.45
AGAL014.492−00.139	2.41 (0.47)	40.53 (0.47)	4.79 (1.42)	0.47	1.10 (0.15)	41.14 (0.18)	2.70 (0.48)	0.38
AGAL014.632−00.577	4.80 (0.39)	17.16 (0.07)	2.05 (0.18)	2.20	4.47 (0.17)	17.19 (0.04)	2.35 (0.10)	1.80
AGAL015.029−00.669	35.06 (0.30)	19.49 (0.02)	5.94 (0.06)	5.54	28.96 (0.20)	19.32 (0.02)	5.90 (0.05)	4.61
AGAL018.606−00.074	3.62 (0.21)	45.28 (0.11)	3.89 (0.28)	0.88	3.08 (0.15)	45.19 (0.10)	4.37 (0.27)	0.66
AGAL018.734−00.226	8.78 (0.26)	40.76 (0.08)	6.00 (0.22)	1.37	7.16 (0.16)	40.70 (0.07)	6.01 (0.17)	1.12
AGAL018.888−00.474	9.14 (0.24)	66.04 (0.08)	6.46 (0.20)	1.33	7.12 (0.18)	66.09 (0.07)	6.23 (0.19)	1.07
AGAL019.882−00.534	17.78 (0.26)	44.11 (0.04)	5.11 (0.10)	3.28	15.33 (0.01)	43.97 (0.02)	4.53 (0.05)	3.17
AGAL022.376+00.447	3.45 (0.29)	53.04 (0.19)	5.26 (0.65)	0.62	3.51 (0.19)	52.80 (0.15)	6.03 (0.44)	0.55
AGAL023.206−00.377	10.45 (0.37)	77.55 (0.18)	11.09 (0.50)	0.88	10.56 (0.23)	77.63 (0.12)	10.91 (0.29)	0.91
AGAL024.629+00.172	1.40 (0.19)	115.50 (0.23)	3.40 (0.49)	0.39	1.31 (0.16)	115.00 (0.27)	5.18 (0.86)	0.24
AGAL028.564−00.236	2.46 (0.29)	87.25 (0.47)	8.16 (1.04)	0.28	1.79 (0.17)	86.90 (0.36)	7.58 (0.75)	0.22
AGAL028.861+00.066	N				N			
AGAL030.848−00.081	3.74 (0.29)	96.10 (0.27)	7.03 (0.68)	0.50	2.82 (0.16)	96.16 (0.17)	6.14 (0.41)	0.43
AGAL030.893+00.139	1.33 (0.25)	106.90 (0.44)	4.90 (1.08)	0.26	0.90 (0.12)	106.80 (0.36)	5.08 (0.80)	0.17
AGAL031.412+00.307	6.23 (0.28)	95.27 (0.12)	5.82 (0.33)	1.01	7.70 (0.22)	95.23 (0.09)	6.83 (0.25)	1.06
AGAL034.258+00.154	34.96 (0.30)	57.13 (0.02)	5.46 (0.06)	6.01	32.39 (0.18)	57.15 (0.01)	5.57 (0.04)	5.46
AGAL034.401+00.226	18.52 (0.27)	57.62 (0.04)	6.36 (0.12)	2.74	17.13 (0.19)	57.76 (0.03)	6.42 (0.09)	2.51
AGAL034.411+00.234	18.46 (0.34)	58.01 (0.05)	6.49 (0.16)	2.67	15.97 (0.17)	57.83 (0.03)	6.29 (0.08)	2.39
AGAL034.821+00.351	6.23 (0.19)	57.00 (0.06)	3.99 (0.16)	1.46	3.73 (0.18)	57.15 (0.09)	3.70 (0.22)	0.95
AGAL035.197−00.742	17.91 (0.38)	36.22 (0.04)	4.82 (0.13)	3.49	14.96 (0.29)	35.81 (0.04)	4.99 (0.12)	2.81
AGAL037.554+00.201	6.17 (0.28)	85.49 (0.16)	7.45 (0.39)	0.78	4.46 (0.16)	85.48 (0.11)	6.17 (0.25)	0.68
AGAL043.166+00.011	52.65 (0.26)	6.02 (0.04)	14.95 (0.09)	3.30	45.12 (0.21)	5.57 (0.03)	14.24 (0.08)	2.97
AGAL049.489−00.389	80.07 (0.41)	56.02 (0.03)	10.41 (0.06)	7.23	71.94 (0.26)	55.95 (0.02)	10.43 (0.04)	6.48
AGAL053.141+00.069	17.59 (0.17)	21.59 (0.02)	4.71 (0.06)	3.51	14.83 (0.11)	21.55 (0.02)	4.62 (0.04)	3.01
AGAL059.782+00.066	N				N			
AGAL305.192−00.006	7.28 (0.24)	-34.12 (0.07)	4.33 (0.18)	1.58	6.09 (0.10)	-34.16 (0.04)	4.65 (0.10)	1.23
AGAL305.209+00.206	33.80 (0.35)	-41.21 (0.04)	8.09 (0.10)	3.93	30.19 (0.17)	-41.35 (0.02)	7.97 (0.05)	3.55
AGAL305.562+00.014	10.60 (0.23)	-39.33 (0.04)	4.05 (0.11)	2.46	8.94 (0.10)	-39.43 (0.02)	3.94 (0.05)	2.13
AGAL305.794−00.096	1.50 (0.24)	-41.40 (0.28)	3.67 (0.77)	0.38	0.97 (0.10)	-41.12 (0.19)	3.89 (0.51)	0.23
AGAL309.384−00.134	10.41 (0.33)	-51.17 (0.08)	5.60 (0.22)	1.74	10.32 (0.17)	-51.06 (0.05)	5.94 (0.12)	1.64
AGAL310.014+00.387	6.10 (0.24)	-41.13 (0.07)	3.58 (0.18)	1.59	5.71 (0.11)	-41.05 (0.03)	3.76 (0.09)	1.43
AGAL313.576+00.324	N				N			
AGAL316.641−00.087	N				N			
AGAL317.867−00.151	11.66 (0.28)	-39.98 (0.10)	8.31 (0.23)	1.32	9.39 (0.17)	-40.11 (0.07)	8.29 (0.17)	1.06
AGAL318.779−00.137	4.22 (0.30)	-39.15 (0.26)	8.02 (0.74)	0.49	3.07 (0.15)	-39.02 (0.17)	7.15 (0.45)	0.40
AGAL320.881−00.397	2.67 (0.23)	-45.78 (0.16)	4.12 (0.47)	0.61	1.43 (0.11)	-45.65 (0.13)	3.36 (0.28)	0.40
AGAL326.661+00.519	8.80 (0.20)	-39.18 (0.04)	3.31 (0.09)	2.51	6.51 (0.12)	-39.41 (0.03)	3.09 (0.07)	1.97
AGAL326.987−00.032	6.95 (0.34)	-57.82 (0.16)	6.89 (0.43)	0.95	5.98 (0.26)	-57.59 (0.13)	6.47 (0.37)	0.87
AGAL327.119+00.509	4.68 (0.25)	-83.54 (0.14)	5.21 (0.34)	0.84	3.55 (0.21)	-83.59 (0.14)	4.99 (0.36)	0.67
AGAL327.293−00.579	36.31 (0.52)	-44.29 (0.06)	8.94 (0.14)	3.82	32.32 (0.52)	-44.45 (0.08)	9.53 (0.17)	3.19
AGAL327.393+00.199	13.19 (0.20)	-88.68 (0.04)	4.97 (0.09)	2.49	10.14 (0.10)	-88.81 (0.02)	5.20 (0.06)	1.83
AGAL328.809+00.632	48.67 (0.34)	-42.05 (0.02)	6.60 (0.06)	6.93	44.47 (0.30)	-42.03 (0.02)	6.96 (0.06)	6.00
AGAL329.029−00.206	17.22 (0.38)	-43.68 (0.11)	10.63 (0.28)	1.52	14.13 (0.21)	-43.63 (0.07)	9.77 (0.17)	1.36
AGAL329.066−00.307	11.53 (0.31)	-42.08 (0.09)	6.91 (0.24)	1.57	8.99 (0.16)	-42.00 (0.05)	6.43 (0.15)	1.31
AGAL330.879−00.367	26.61 (0.32)	-62.59 (0.05)	8.27 (0.12)	3.03	24.04 (0.19)	-62.41 (0.03)	8.44 (0.08)	2.68
AGAL330.954−00.182	39.93 (0.35)	-92.47 (0.04)	9.86 (0.11)	3.80	36.57 (0.30)	-92.63 (0.04)	9.86 (0.10)	3.49
AGAL331.709+00.582	14.20 (0.32)	-66.19 (0.08)	7.84 (0.23)	1.70	12.37 (0.19)	-66.14 (0.06)	8.51 (0.16)	1.37
AGAL332.094−00.421	7.44 (0.16)	-56.47 (0.04)	3.87 (0.11)	1.81	5.19 (0.12)	-56.66 (0.04)	3.72 (0.11)	1.31

Table A.2. continued.

Sources	ortho-H_2CO 3_{13}–2_{12}				ortho-H_2CO 3_{12}–2_{11}			
	$\int T_{mb} dv$	V_{lsr}	FWHM	T_{mb}	$\int T_{mb} dv$	V_{lsr}	FWHM	T_{mb}
	K km s^{-1}	km s^{-1}	km s^{-1}	K	K km s^{-1}	km s^{-1}	km s^{-1}	K
AGAL332.826−00.549	28.19 (0.30)	-56.18 (0.04)	7.01 (0.09)	3.78	24.74 (0.17)	-56.35 (0.02)	6.85 (0.06)	3.39
AGAL333.134−00.431	46.54 (0.36)	-52.73 (0.03)	8.11 (0.08)	5.39	40.91 (0.18)	-52.87 (0.02)	7.99 (0.04)	4.81
AGAL333.284−00.387	14.65 (0.30)	-52.06 (0.06)	5.77 (0.13)	2.39	11.42 (0.13)	-52.11 (0.03)	5.60 (0.07)	1.91
AGAL333.314+00.106	10.09 (0.29)	-46.08 (0.08)	5.78 (0.21)	1.64	8.12 (0.22)	-46.15 (0.07)	5.51 (0.19)	1.38
AGAL333.604−00.212	32.84 (0.36)	-46.94 (0.04)	7.36 (0.11)	4.19	26.38 (0.28)	-46.94 (0.04)	7.23 (0.10)	3.42
AGAL333.656+00.059	2.06 (0.21)	-84.44 (0.24)	4.59 (0.53)	0.42	1.44 (0.18)	-85.00 (0.27)	4.39 (0.60)	0.31
AGAL335.789+00.174	18.59 (0.38)	-50.07 (0.07)	7.25 (0.19)	2.41	15.55 (0.21)	-50.16 (0.04)	6.99 (0.13)	2.09
AGAL336.958−00.224	4.88 (0.35)	-71.19 (0.24)	6.92 (0.58)	0.66	3.99 (0.34)	-70.85 (0.33)	8.25 (0.96)	0.45
AGAL337.176−00.032	5.15 (0.32)	-68.99 (0.14)	4.98 (0.41)	0.97	4.35 (0.27)	-68.82 (0.13)	4.72 (0.41)	0.87
AGAL337.258−00.101	3.75 (0.30)	-67.76 (0.19)	5.23 (0.53)	0.67	3.22 (0.27)	-67.39 (0.23)	5.51 (0.59)	0.55
AGAL337.286+00.007	...	...	...	...	...	...	...	...
AGAL337.406−00.402	35.26 (0.36)	-40.93 (0.03)	6.77 (0.08)	4.90	30.78 (0.25)	-41.04 (0.03)	6.87 (0.07)	4.20
AGAL337.704−00.054	17.57 (0.38)	-47.71 (0.09)	8.67 (0.22)	1.90	14.28 (0.20)	-47.92 (0.06)	8.77 (0.15)	1.54
AGAL337.916−00.477	36.86 (0.38)	-39.31 (0.03)	6.24 (0.08)	5.55	32.39 (0.25)	-39.44 (0.02)	6.25 (0.06)	4.87
AGAL338.066+00.044	...	...	...	...	1.19 (0.14)	-68.60 (0.22)	3.61 (0.52)	0.31
AGAL338.786+00.476	3.90 (0.31)	-64.31 (0.28)	7.04 (0.62)	0.52	2.79 (0.26)	-64.27 (0.29)	6.35 (0.69)	0.41
AGAL338.926+00.554	36.09 (0.01)	-61.96 (0.04)	8.01 (0.07)	4.23	35.72 (0.34)	-61.82 (0.04)	8.77 (0.10)	3.83
AGAL339.623−00.122	9.49 (0.34)	-33.37 (0.10)	5.94 (0.29)	1.51	7.61 (0.18)	-33.57 (0.06)	5.80 (0.19)	1.23
AGAL340.374−00.391	4.50 (0.37)	-44.09 (0.26)	7.05 (0.81)	0.60	3.23 (0.15)	-44.36 (0.14)	5.94 (0.33)	0.51
AGAL340.746−01.001	7.30 (0.30)	-29.67 (0.08)	4.29 (0.22)	1.59	5.83 (0.14)	-29.64 (0.05)	4.10 (0.13)	1.34
AGAL340.784−00.097	5.63 (0.34)	-101.80 (0.18)	6.43 (0.51)	0.82	4.33 (0.16)	-101.60 (0.10)	5.97 (0.27)	0.68
AGAL341.217−00.212	10.46 (0.32)	-43.15 (0.08)	5.34 (0.22)	1.84	9.56 (0.16)	-43.29 (0.04)	4.91 (0.11)	1.83
AGAL342.484+00.182	5.87 (0.25)	-41.38 (0.08)	3.92 (0.22)	1.41	5.21 (0.12)	-41.44 (0.05)	4.18 (0.12)	1.17
AGAL343.128−00.062	24.01 (0.42)	-31.03 (0.07)	8.32 (0.19)	2.71	21.81 (0.23)	-31.19 (0.04)	8.17 (0.12)	2.51
AGAL343.756−00.164	13.69 (0.39)	-28.03 (0.08)	5.42 (0.19)	2.38	15.22 (0.14)	-28.01 (0.03)	5.78 (0.07)	2.48
AGAL344.227−00.569	6.62 (1.27)	-19.71 (0.25)	3.94 (0.37)	1.58	5.64 (1.23)	-19.63 (0.21)	4.01 (0.32)	1.32
AGAL345.003−00.224	28.46 (0.43)	-25.98 (0.07)	9.46 (0.17)	2.83	25.35 (0.44)	-26.19 (0.08)	9.48 (0.20)	2.51
AGAL345.488+00.314	23.51 (0.34)	-17.58 (0.04)	5.93 (0.11)	3.72	19.61 (0.17)	-17.81 (0.02)	5.88 (0.06)	3.13
AGAL345.504+00.347	17.25 (0.36)	-16.26 (0.04)	4.55 (0.13)	3.57	15.36 (0.21)	-16.41 (0.03)	4.52 (0.08)	3.19
AGAL345.718+00.817	4.65 (0.29)	-11.59 (0.13)	4.39 (0.32)	1.00	3.88 (0.14)	-11.73 (0.07)	4.08 (0.18)	0.89
AGAL351.131+00.771	1.52 (0.12)	-5.38 (0.07)	1.69 (0.16)	0.84	1.03 (0.09)	-5.37 (0.07)	1.69 (0.16)	0.57
AGAL351.161+00.697	40.55 (0.29)	-5.97 (0.02)	5.94 (0.05)	6.41	34.48 (0.27)	-6.02 (0.02)	5.84 (0.06)	5.55
AGAL351.244+00.669	28.30 (0.23)	-2.92 (0.02)	5.40 (0.05)	4.93	22.42 (0.17)	-2.98 (0.02)	5.30 (0.05)	3.99
AGAL351.571+00.762	1.20 (0.13)	-3.30 (0.11)	1.91 (0.23)	0.59	0.92 (0.13)	-3.67 (0.18)	2.64 (0.48)	0.33
AGAL351.581−00.352	9.72 (0.25)	-97.84 (0.05)	4.41 (0.15)	2.07	8.78 (0.18)	-97.98 (0.05)	4.72 (0.12)	1.75
AGAL351.774−00.537	60.01 (0.53)	-1.70 (0.04)	10.31 (0.12)	5.46	56.61 (0.63)	-1.92 (0.05)	10.50 (0.15)	5.07
AGAL353.066+00.452	2.20 (0.18)	1.38 (0.11)	2.84 (0.29)	0.73	1.34 (0.12)	1.26 (0.12)	2.67 (0.32)	0.47
AGAL353.409−00.361	21.12 (0.28)	-16.34 (0.05)	8.17 (0.12)	2.43	17.45 (0.19)	-16.50 (0.04)	7.52 (0.10)	2.17
AGAL353.417−00.079	...	...	...	...	0.28 (0.08)	-16.82 (0.20)	1.38 (0.44)	0.19
AGAL354.944−00.537	1.57 (0.17)	-5.69 (0.17)	3.09 (0.38)	0.48	1.08 (0.13)	-6.13 (0.21)	3.60 (0.55)	0.28

Notes. "N" in the table indicates that the source has not been observed.

Table A.3. Para-H_2CO 3_{03}–2_{02} and 3_{22}–2_{21} spectral parameters.

Sources	para-H_2CO 3_{03}–2_{02}				para-H_2CO 3_{22}–2_{21}			
	$\int T_{mb}dv$	V_{lsr}	FWHM	T_{mb}	$\int T_{mb}dv$	V_{lsr}	FWHM	T_{mb}
	K km s^{-1}	km s^{-1}	km s^{-1}	K	K km s^{-1}	km s^{-1}	km s^{-1}	K
AGAL008.684−00.367	5.50 (0.17)	37.95 (0.08)	5.50 (0.20)	0.94	0.92 (0.08)	38.07 (0.13)	2.75 (0.27)	0.31
AGAL008.706−00.414	0.67 (0.13)	38.47 (0.24)	2.70 (0.69)	0.23	...	...	...	...
AGAL010.444−00.017	...	...	...		...	...	...	...
AGAL010.472+00.027	12.01 (0.28)	65.77 (0.09)	8.16 (0.23)	1.38	5.51 (0.24)	65.50 (0.17)	8.08 (0.41)	0.64
AGAL010.624−00.384	25.67 (0.24)	-3.40 (0.04)	7.83 (0.09)	3.09	7.49 (0.17)	-3.22 (0.07)	6.71 (0.18)	1.05
AGAL012.804−00.199	13.97 (0.18)	35.77 (0.04)	6.78 (0.10)	1.94	4.10 (0.62)	35.44 (0.42)	5.75 (1.06)	0.67
AGAL013.178+00.059	5.22 (0.16)	49.16 (0.07)	4.93 (0.18)	1.00	1.29 (0.16)	48.80 (0.42)	6.50 (0.92)	0.19
AGAL013.658−00.599	3.96 (0.29)	47.65 (0.21)	5.91 (0.52)	0.63	...	...	...	...
AGAL014.114−00.574	3.78 (0.10)	19.67 (0.04)	3.08 (0.10)	1.15	0.41 (0.08)	19.91 (0.22)	2.01 (0.47)	0.19
AGAL014.194−00.194	5.60 (0.14)	39.72 (0.06)	5.26 (0.17)	1.00	1.18 (0.12)	39.38 (0.18)	3.67 (0.40)	0.30
AGAL014.492−00.139	1.61 (0.18)	39.88 (0.30)	5.79 (0.90)	0.26	...	...	...	...
AGAL014.632−00.577	4.32 (0.12)	18.33 (0.05)	3.80 (0.12)	1.07	0.91 (0.11)	18.70 (0.15)	2.84 (0.43)	0.30
AGAL015.029−00.669	17.49 (0.17)	19.36 (0.03)	5.41 (0.06)	3.03	4.44 (0.12)	19.39 (0.06)	4.88 (0.17)	0.86
AGAL018.606−00.074	1.86 (0.13)	45.24 (0.11)	3.16 (0.26)	0.55	...	...	...	...
AGAL018.734−00.226	5.46 (0.14)	40.73 (0.08)	6.04 (0.19)	0.85	0.98 (0.11)	40.70 (0.23)	3.96 (0.49)	0.23
AGAL018.888−00.474	5.69 (0.15)	65.62 (0.08)	6.16 (0.20)	0.87	1.06 (0.16)	66.06 (0.41)	5.15 (1.10)	0.19
AGAL019.882−00.534	11.31 (0.14)	43.83 (0.03)	4.35 (0.07)	2.43	2.74 (0.11)	44.10 (0.06)	3.35 (0.16)	0.77
AGAL022.376+00.447	2.43 (0.12)	52.44 (0.12)	5.07 (0.33)	0.45	...	...	...	...
AGAL023.206−00.377	6.77 (0.21)	77.25 (0.11)	8.06 (0.32)	0.79	1.84 (0.16)	77.58 (0.21)	5.26 (0.58)	0.33
AGAL024.629+00.172	0.68 (0.11)	114.60 (0.15)	2.18 (0.49)	0.29	...	...	...	...
AGAL028.564−00.236	0.58 (0.11)	88.24 (0.22)	2.92 (0.72)	0.19	...	...	...	...
AGAL028.861+00.066	N				N			
AGAL030.848−00.081	1.70 (0.17)	96.18 (0.29)	5.98 (0.67)	0.27	...	...	...	...
AGAL030.893+00.139	0.64 (0.25)	105.80 (0.83)	5.36 (3.61)	0.11	...	...	...	...
AGAL031.412+00.307	6.55 (0.28)	95.85 (0.12)	6.61 (0.35)	0.93	3.91 (0.14)	96.75 (0.17)	7.68 (0.39)	0.52
AGAL034.258+00.154	23.13 (0.19)	57.45 (0.02)	5.69 (0.06)	3.83	8.39 (0.21)	58.08 (0.07)	5.88 (0.17)	1.34
AGAL034.401+00.226	11.47 (0.28)	57.77 (0.07)	5.82 (0.18)	1.86	2.72 (0.21)	57.82 (0.23)	4.56 (0.56)	0.47
AGAL034.411+00.234	11.19 (0.18)	57.70 (0.04)	5.83 (0.12)	1.80	3.26 (0.19)	57.79 (0.12)	4.14 (0.32)	0.53
AGAL034.821+00.351	2.61 (0.18)	56.91 (0.13)	3.94 (0.32)	0.62	...	...	...	...
AGAL035.197−00.742	14.91 (0.15)	34.80 (0.03)	6.52 (0.08)	2.14	4.42 (0.19)	34.12 (0.09)	5.66 (0.22)	0.80
AGAL037.554+00.201	3.20 (0.14)	84.99 (0.13)	5.69 (0.30)	0.53	0.49 (0.11)	85.72 (0.17)	1.94 (0.59)	0.24
AGAL043.166+00.011	18.94 (0.93)	3.95 (0.20)	9.35 (0.27)	1.90	7.06 (1.15)	5.01 (0.28)	9.34 (0.46)	0.77
AGAL049.489−00.389	50.96 (0.35)	56.05 (0.03)	9.50 (0.07)	5.04	22.17 (0.16)	56.27 (0.08)	8.48 (0.19)	2.23
AGAL053.141+00.069	10.18 (0.17)	21.64 (0.03)	4.30 (0.09)	2.23	2.83 (0.16)	21.39 (0.08)	4.48 (0.22)	0.59
AGAL059.782+00.066	N				N			
AGAL305.192−00.006	4.05 (0.12)	-34.11 (0.06)	4.49 (0.17)	0.85	0.86 (0.09)	-34.52 (0.16)	2.52 (0.35)	0.27
AGAL305.209+00.206	18.43 (0.16)	-41.19 (0.03)	7.42 (0.08)	2.33	5.94 (0.16)	-40.94 (0.10)	6.87 (0.24)	0.71
AGAL305.562+00.014	5.87 (0.11)	-39.45 (0.03)	3.72 (0.09)	1.48	1.33 (0.11)	-39.43 (0.12)	3.42 (0.35)	0.36
AGAL305.794−00.096	0.65 (0.11)	-41.35 (0.29)	3.74 (0.88)	0.16	...	...	...	...
AGAL309.384−00.134	5.67 (0.16)	-50.94 (0.06)	4.82 (0.17)	1.10	1.56 (0.12)	-50.88 (0.16)	3.68 (0.50)	0.34
AGAL310.014+00.387	3.40 (0.12)	-40.98 (0.05)	3.27 (0.15)	0.98	1.04 (0.11)	-41.17 (0.21)	3.57 (0.56)	0.23
AGAL313.576+00.324	N				N			
AGAL316.641−00.087	N				N			
AGAL317.867−00.151	7.47 (0.17)	-40.29 (0.08)	7.53 (0.20)	0.93	1.97 (0.13)	-41.12 (0.17)	4.86 (0.42)	0.35
AGAL318.779−00.137	2.45 (0.15)	-38.83 (0.18)	6.24 (0.48)	0.37	0.96 (0.15)	-39.31 (0.49)	6.57 (1.23)	0.14
AGAL320.881−00.397	1.43 (0.13)	-45.17 (0.18)	4.05 (0.46)	0.33	...	...	...	...
AGAL326.661+00.519	4.35 (0.11)	-39.38 (0.04)	3.22 (0.09)	1.27	1.19 (0.14)	-39.31 (0.23)	3.33 (0.63)	0.24
AGAL326.987−00.032	4.62 (0.14)	-57.76 (0.07)	5.10 (0.21)	0.85	0.40 (0.05)	-57.73 (0.09)	1.61 (0.27)	0.23
AGAL327.119+00.509	2.69 (0.12)	-83.71 (0.11)	4.78 (0.27)	0.53	...	...	...	...
AGAL327.293−00.579	13.43 (0.52)	-46.51 (0.67)	4.55 (0.67)	2.77	12.79 (0.36)	-44.52 (0.03)	6.73 (0.06)	1.62
AGAL327.393+00.199	5.85 (0.12)	-88.74 (0.05)	4.78 (0.12)	1.15	1.15 (0.12)	-88.71 (0.14)	4.12 (0.32)	0.29
AGAL328.809+00.632	32.91 (0.22)	-41.75 (0.02)	6.45 (0.05)	4.80	12.46 (0.17)	-41.61 (0.04)	5.90 (0.09)	2.00
AGAL329.029−00.206	11.16 (0.20)	-43.39 (0.06)	7.65 (0.17)	1.37	3.72 (0.17)	-43.41 (0.13)	5.97 (0.34)	0.51
AGAL329.066−00.307	6.93 (0.16)	-42.11 (0.06)	5.85 (0.16)	1.11	1.62 (0.15)	-42.45 (0.20)	4.37 (0.47)	0.30
AGAL330.879−00.367	16.90 (0.19)	-62.56 (0.04)	7.39 (0.10)	2.14	6.62 (0.15)	-62.34 (0.09)	6.68 (0.21)	0.79
AGAL330.954−00.182	26.00 (0.16)	-92.33 (0.03)	9.79 (0.07)	2.49	10.84 (0.15)	-92.24 (0.08)	9.43 (0.19)	1.01
AGAL331.709+00.582	8.39 (0.16)	-66.35 (0.06)	7.11 (0.18)	1.11	2.27 (0.17)	-66.68 (0.21)	5.04 (0.56)	0.29
AGAL332.094−00.421	3.76 (0.11)	-56.89 (0.05)	3.73 (0.13)	0.95	0.97 (0.09)	-56.35 (0.32)	4.96 (0.79)	0.19

Table A.3. continued.

Sources	para-H_2CO 3_{03}–2_{02}				para-H_2CO 3_{22}–2_{21}			
	$\int T_{mb} dv$	V_{lsr}	FWHM	T_{mb}	$\int T_{mb} dv$	V_{lsr}	FWHM	T_{mb}
	K km s^{-1}	km s^{-1}	km s^{-1}	K	K km s^{-1}	km s^{-1}	km s^{-1}	K
AGAL332.826−00.549	17.25 (0.16)	-56.68 (0.03)	6.42 (0.07)	2.52	6.23 (0.14)	-57.17 (0.07)	6.13 (0.16)	0.96
AGAL333.134−00.431	26.32 (0.19)	-52.99 (0.02)	7.26 (0.06)	3.41	8.32 (0.15)	-53.26 (0.05)	6.04 (0.13)	1.21
AGAL333.284−00.387	7.60 (0.19)	-52.14 (0.06)	5.08 (0.15)	1.40	2.01 (0.18)	-52.12 (0.28)	4.67 (1.09)	0.40
AGAL333.314+00.106	5.67 (0.14)	-46.28 (0.06)	5.39 (0.17)	0.99	1.16 (0.13)	-45.83 (0.22)	4.56 (0.48)	0.23
AGAL333.604−00.212	15.04 (0.18)	-47.09 (0.04)	6.63 (0.10)	2.13	4.80 (0.14)	-47.26 (0.07)	6.04 (0.17)	0.68
AGAL333.656+00.059	1.23 (0.11)	-84.88 (0.18)	4.15 (0.47)	0.28	...	...	...	...
AGAL335.789+00.174	11.20 (0.26)	-50.27 (0.06)	6.14 (0.19)	1.71	3.35 (0.21)	-50.46 (0.13)	3.82 (0.31)	0.62
AGAL336.958−00.224	2.42 (0.17)	-71.47 (0.16)	5.60 (0.60)	0.41	...	...	...	...
AGAL337.176−00.032	3.34 (0.21)	-68.25 (0.15)	5.46 (0.46)	0.58	...	...	...	...
AGAL337.258−00.101	2.37 (0.19)	-67.82 (0.20)	5.11 (0.49)	0.44	...	...	...	...
AGAL337.286+00.007	...	...	...		...	...	...	...
AGAL337.406−00.402	23.67 (0.26)	-40.84 (0.03)	6.34 (0.09)	3.51	8.10 (0.19)	-40.65 (0.07)	5.36 (0.17)	1.39
AGAL337.704−00.054	11.38 (0.26)	-47.63 (0.09)	8.49 (0.23)	1.26	3.38 (0.19)	-47.68 (0.29)	7.10 (0.66)	0.37
AGAL337.916−00.477	25.90 (0.26)	-39.24 (0.03)	5.87 (0.07)	4.14	10.46 (0.13)	-39.28 (0.04)	5.43 (0.10)	1.62
AGAL338.066+00.044	1.10 (0.10)	-69.56 (0.18)	4.09 (0.50)	0.25	...	...	...	...
AGAL338.786+00.476	2.13 (0.14)	-64.15 (0.13)	4.11 (0.31)	0.49	...	...	...	...
AGAL338.926+00.554	22.87 (0.03)	-61.97 (0.07)	7.80 (0.13)	2.75	7.31 (0.32)	-62.04 (0.16)	6.57 (0.39)	0.95
AGAL339.623−00.122	5.06 (0.21)	-33.99 (0.09)	4.72 (0.28)	1.01	...	...	...	...
AGAL340.374−00.391	2.59 (0.18)	-44.11 (0.15)	4.93 (0.44)	0.49	...	...	...	...
AGAL340.746−01.001	5.47 (0.12)	-29.63 (0.04)	3.87 (0.10)	1.33	1.29 (0.10)	-29.59 (0.15)	3.31 (0.34)	0.29
AGAL340.784−00.097	3.24 (0.24)	-101.70 (0.23)	6.31 (0.56)	0.48	...	...	...	...
AGAL341.217−00.212	7.07 (0.18)	-43.28 (0.05)	4.26 (0.13)	1.57	1.94 (0.17)	-43.45 (0.15)	3.60 (0.35)	0.40
AGAL342.484+00.182	3.66 (0.15)	-41.47 (0.06)	3.39 (0.17)	1.01	0.69 (0.11)	-41.35 (0.25)	2.69 (0.47)	0.26
AGAL343.128−00.062	16.33 (0.26)	-30.91 (0.05)	7.43 (0.16)	2.07	5.74 (0.21)	-30.77 (0.10)	6.66 (0.27)	0.80
AGAL343.756−00.164	10.45 (0.19)	-28.05 (0.04)	4.95 (0.11)	1.99	3.36 (0.17)	-27.99 (0.11)	4.72 (0.25)	0.67
AGAL344.227−00.569	10.46 (0.22)	-21.49 (0.07)	6.77 (0.17)	1.45	3.66 (0.17)	-21.95 (0.13)	4.71 (0.32)	0.62
AGAL345.003−00.224	19.51 (0.25)	-26.53 (0.05)	8.63 (0.14)	2.12	6.15 (0.21)	-26.88 (0.10)	6.38 (0.24)	0.83
AGAL345.488+00.314	14.97 (0.20)	-17.70 (0.04)	5.61 (0.09)	2.51	4.29 (0.16)	-17.60 (0.12)	5.97 (0.29)	0.79
AGAL345.504+00.347	12.54 (0.19)	-16.64 (0.03)	4.95 (0.09)	2.38	4.21 (0.17)	-17.03 (0.11)	4.54 (0.25)	0.78
AGAL345.718+00.817	2.94 (0.12)	-11.49 (0.05)	2.84 (0.14)	0.97	0.63 (0.12)	-10.84 (0.23)	2.41 (0.61)	0.26
AGAL351.131+00.771	1.14 (0.08)	-5.38 (0.06)	1.97 (0.17)	0.54	...	...	...	...
AGAL351.161+00.697	24.94 (0.22)	-6.14 (0.02)	5.46 (0.06)	4.29	8.55 (0.16)	-6.38 (0.04)	4.72 (0.10)	1.55
AGAL351.244+00.669	15.83 (0.14)	-3.13 (0.02)	4.88 (0.05)	3.04	4.95 (0.12)	-3.15 (0.06)	4.61 (0.15)	0.96
AGAL351.571+00.762	0.54 (0.08)	-3.49 (0.14)	1.95 (0.37)	0.26	...	...	...	...
AGAL351.581−00.352	8.62 (0.15)	-97.41 (0.04)	4.92 (0.11)	1.65	7.00 (0.15)	-95.53 (0.08)	6.52 (0.17)	0.93
AGAL351.774−00.537	42.35 (0.59)	-2.18 (0.06)	9.22 (0.16)	4.32	20.03 (0.19)	-2.81 (0.11)	8.57 (0.27)	2.25
AGAL353.066+00.452	0.93 (0.14)	1.50 (0.17)	2.21 (0.41)	0.40	...	...	...	...
AGAL353.409−00.361	13.61 (0.16)	-16.34 (0.04)	6.80 (0.10)	1.88	4.54 (0.12)	-16.31 (0.08)	5.09 (0.21)	0.74
AGAL353.417−00.079	0.18 (0.03)	-17.01 (0.04)	0.67 (1.33)	0.25	...	...	...	...
AGAL354.944−00.537	1.08 (0.11)	-6.10 (0.16)	3.24 (0.42)	0.31	...	...	...	...

Notes. "N" in the table indicates that the source has not been observed.

Table A.4. Para-H_2CO 3_{21}–2_{20} and 4_{04}–3_{03} spectral parameters.

Sources	para-H_2CO 3_{21}–2_{20}				para-H_2CO 4_{04}–3_{03}			
	$\int T_{mb} dv$	V_{lsr}	FWHM	T_{mb}	$\int T_{mb} dv$	V_{lsr}	FWHM	T_{mb}
	K km s^{-1}	km s^{-1}	km s^{-1}	K	K km s^{-1}	km s^{-1}	km s^{-1}	K
AGAL008.684−00.367	1.09 (0.14)	38.76 (0.30)	4.67 (0.63)	0.22	7.71 (0.13)	38.16 (0.04)	4.80 (0.10)	1.51
AGAL008.706−00.414	0.84 (0.17)	36.84 (0.61)	6.00 (1.42)	0.13	1.02 (0.10)	38.71 (0.16)	3.41 (0.43)	0.28
AGAL010.444−00.017	...	...	...	...	1.80 (0.11)	75.66 (0.15)	4.87 (0.38)	0.35
AGAL010.472+00.027	5.64 (0.24)	65.80 (0.17)	8.08 (0.43)	0.66	25.97 (0.55)	65.91 (0.09)	9.10 (0.23)	2.68
AGAL010.624−00.384	8.80 (0.20)	-2.93 (0.08)	7.35 (0.20)	1.13	50.55 (0.93)	-3.44 (0.07)	7.61 (0.17)	6.23
AGAL012.804−00.199	4.04 (0.18)	35.37 (0.10)	4.81 (0.27)	0.79	22.72 (0.13)	35.33 (0.02)	6.81 (0.05)	3.13
AGAL013.178+00.059	1.80 (0.20)	49.04 (0.32)	6.79 (1.05)	0.25	7.09 (0.10)	49.17 (0.03)	4.89 (0.08)	1.36
AGAL013.658−00.599	...	...	...	...	5.13 (0.12)	47.93 (0.06)	5.62 (0.18)	0.86
AGAL014.114−00.574	0.89 (0.14)	19.82 (0.29)	3.93 (0.80)	0.21	5.31 (0.07)	19.93 (0.02)	3.10 (0.05)	1.61
AGAL014.194−00.194	1.29 (0.16)	39.32 (0.24)	4.00 (0.58)	0.30	6.18 (0.11)	39.60 (0.04)	4.61 (0.10)	1.26
AGAL014.492−00.139	...	...	...	...	1.69 (0.10)	39.77 (0.14)	4.94 (0.36)	0.32
AGAL014.632−00.577	1.34 (0.14)	18.30 (0.18)	3.64 (0.46)	0.34	7.86 (0.09)	18.09 (0.02)	3.14 (0.04)	2.35
AGAL015.029−00.669	4.80 (0.20)	19.28 (0.11)	5.67 (0.28)	0.80	18.75 (0.11)	18.91 (0.01)	4.53 (0.03)	3.90
AGAL018.606−00.074	...	...	...	...	3.13 (0.09)	45.21 (0.05)	4.18 (0.14)	0.70
AGAL018.734−00.226	0.91 (0.11)	40.67 (0.21)	3.43 (0.45)	0.25	6.09 (0.11)	40.52 (0.05)	6.16 (0.13)	0.93
AGAL018.888−00.474	0.90 (0.11)	66.24 (0.21)	3.47 (0.49)	0.24	5.80 (0.10)	66.36 (0.04)	5.03 (0.11)	1.08
AGAL019.882−00.534	3.21 (0.14)	43.80 (0.01)	4.53 (0.25)	0.67	18.61 (0.11)	43.79 (0.01)	4.36 (0.03)	4.01
AGAL022.376+00.447	...	...	...	...	3.40 (0.10)	52.69 (0.06)	4.23 (0.15)	0.76
AGAL023.206−00.377	2.42 (0.22)	77.51 (0.26)	6.16 (0.75)	0.37	16.51 (0.15)	77.28 (0.03)	7.28 (0.09)	2.13
AGAL024.629+00.172	...	...	...	...	1.64 (0.09)	115.00 (0.12)	4.36 (0.29)	0.35
AGAL028.564−00.236	...	...	...	...	1.48 (0.08)	86.61 (0.13)	5.42 (0.33)	0.26
AGAL028.861+00.066	N				5.84 (0.10)	103.60 (0.03)	4.37 (0.09)	1.26
AGAL030.848−00.081	...	...	...	...	2.02 (0.10)	95.87 (0.13)	5.49 (0.30)	0.35
AGAL030.893+00.139	...	...	...	...	0.82 (0.09)	106.70 (0.19)	3.62 (0.54)	0.21
AGAL031.412+00.307	4.28 (0.19)	96.92 (0.12)	6.78 (0.31)	0.54	17.46 (0.21)	96.73 (0.04)	8.02 (0.12)	2.04
AGAL034.258+00.154	9.23 (0.16)	58.13 (0.05)	6.30 (0.13)	1.38	43.62 (0.46)	57.90 (0.03)	6.23 (0.08)	6.58
AGAL034.401+00.226	2.28 (0.24)	58.11 (0.17)	4.35 (0.38)	0.59	15.28 (0.12)	58.09 (0.02)	5.38 (0.05)	2.67
AGAL034.411+00.234	2.35 (0.15)	57.78 (0.14)	5.17 (0.37)	0.59	15.36 (0.14)	57.65 (0.02)	5.39 (0.06)	2.68
AGAL034.821+00.351	...	...	...	...	2.30 (0.09)	56.86 (0.06)	3.22 (0.17)	0.67
AGAL035.197−00.742	4.81 (0.15)	34.23 (0.11)	5.37 (0.29)	0.77	19.12 (0.12)	34.11 (0.02)	5.97 (0.04)	3.01
AGAL037.554+00.201	0.90 (0.13)	84.63 (0.40)	4.92 (0.81)	0.17	4.96 (0.14)	85.24 (0.07)	5.54 (0.20)	0.84
AGAL043.166+00.011	7.68 (0.48)	3.99 (0.57)	8.72 (0.69)	0.76	45.42 (2.14)	6.02 (0.30)	12.77 (0.72)	3.35
AGAL049.489−00.389	20.12 (0.39)	56.29 (0.03)	8.73 (0.07)	2.39	81.22 (0.83)	56.03 (0.05)	9.82 (0.12)	7.77
AGAL053.141+00.069	2.80 (0.11)	21.64 (0.13)	4.60 (0.30)	0.58	13.63 (0.16)	21.61 (0.02)	4.41 (0.06)	2.90
AGAL059.782+00.066	N				5.84 (0.15)	22.29 (0.03)	2.81 (0.09)	1.94
AGAL305.192−00.006	0.73 (0.09)	-34.64 (0.20)	3.63 (0.43)	0.22	4.65 (0.09)	-34.43 (0.04)	3.97 (0.10)	1.10
AGAL305.209+00.206	5.21 (0.15)	-41.05 (0.09)	7.19 (0.23)	0.78	27.46 (0.18)	-41.04 (0.02)	7.52 (0.06)	3.43
AGAL305.562+00.014	1.31 (0.10)	-39.67 (0.14)	3.51 (0.33)	0.36	7.14 (0.09)	-39.53 (0.02)	3.44 (0.05)	1.96
AGAL305.794−00.096	...	...	...	...	0.68 (0.08)	-41.55 (0.20)	3.36 (0.48)	0.19
AGAL309.384−00.134	1.32 (0.13)	-50.90 (0.13)	3.63 (0.37)	0.40	5.50 (0.09)	-51.06 (0.03)	4.36 (0.09)	1.19
AGAL310.014+00.387	0.88 (0.11)	-40.86 (0.20)	3.72 (0.48)	0.26	4.20 (0.09)	-40.95 (0.03)	3.61 (0.10)	1.09
AGAL313.576+00.324	N				6.78 (0.10)	-46.40 (0.04)	5.03 (0.09)	1.27
AGAL316.641−00.087	N				2.68 (0.09)	-17.79 (0.08)	5.31 (0.23)	0.47
AGAL317.867−00.151	1.81 (0.13)	-40.43 (0.18)	5.31 (0.42)	0.35	8.68 (0.10)	-40.57 (0.03)	5.87 (0.08)	1.39
AGAL318.779−00.137	0.64 (0.12)	-39.78 (0.40)	4.41 (1.00)	0.14	3.54 (0.10)	-39.31 (0.06)	4.79 (0.17)	0.69
AGAL320.881−00.397	...	...	...	...	1.03 (0.08)	-45.83 (0.13)	3.20 (0.32)	0.30
AGAL326.661+00.519	0.85 (0.13)	-39.15 (0.24)	3.90 (0.64)	0.29	3.79 (0.07)	-39.53 (0.03)	2.83 (0.07)	1.26
AGAL326.987−00.032	0.91 (0.12)	-57.93 (0.16)	2.97 (0.46)	0.29	5.56 (0.11)	-57.59 (0.04)	4.82 (0.13)	1.08
AGAL327.119+00.509	...	...	...	...	3.30 (0.11)	-83.86 (0.07)	4.65 (0.18)	0.67
AGAL327.293−00.579	11.68 (0.09)	-44.22 (0.10)	7.45 (0.24)	1.61	21.65 (0.73)	-46.54 (0.47)	4.20 (0.47)	4.84
AGAL327.393+00.199	1.28 (0.08)	-88.66 (0.23)	4.45 (0.64)	0.24	5.96 (0.09)	-88.87 (0.03)	4.31 (0.08)	1.30
AGAL328.809+00.632	12.57 (0.17)	-41.62 (0.04)	5.87 (0.09)	2.00	58.68 (0.28)	-41.50 (0.02)	6.67 (0.04)	8.26
AGAL329.029−00.206	3.22 (0.15)	-43.38 (0.14)	6.32 (0.35)	0.55	10.06 (0.12)	-43.55 (0.03)	5.95 (0.09)	1.59
AGAL329.066−00.307	1.39 (0.13)	-41.75 (0.22)	5.13 (0.63)	0.30	6.57 (0.11)	-41.81 (0.03)	4.55 (0.09)	1.36
AGAL330.879−00.367	5.63 (0.16)	-62.17 (0.08)	7.45 (0.20)	0.83	23.93 (0.13)	-62.22 (0.02)	8.14 (0.06)	2.77
AGAL330.954−00.182	10.09 (0.17)	-92.19 (0.07)	9.78 (0.16)	1.04	39.72 (1.24)	-92.73 (0.14)	9.20 (0.34)	4.06
AGAL331.709+00.582	1.54 (0.13)	-66.20 (0.19)	6.00 (0.62)	0.36	8.52 (0.16)	-66.44 (0.05)	6.19 (0.15)	1.29
AGAL332.094−00.421	0.98 (0.12)	-57.02 (0.16)	3.49 (0.34)	0.26	4.73 (0.09)	-57.06 (0.03)	3.80 (0.09)	1.17

Table A.4. continued.

Sources	para-H_2CO 3_{21}–2_{20}				para-H_2CO 4_{04}–3_{03}			
	$\int T_{mb} dv$	V_{lsr}	FWHM	T_{mb}	$\int T_{mb} dv$	V_{lsr}	FWHM	T_{mb}
	K km s^{-1}	km s^{-1}	km s^{-1}	K	K km s^{-1}	km s^{-1}	km s^{-1}	K
AGAL332.826−00.549	6.40 (0.10)	-57.39 (0.05)	5.71 (0.11)	1.05	26.42 (0.15)	-57.16 (0.02)	6.13 (0.04)	4.04
AGAL333.134−00.431	7.80 (0.13)	-53.17 (0.05)	6.20 (0.14)	1.26	28.13 (0.19)	-53.29 (0.02)	6.80 (0.06)	3.88
AGAL333.284−00.387	2.01 (0.30)	-52.18 (0.17)	3.89 (0.39)	0.49	8.22 (0.09)	-52.11 (0.02)	4.42 (0.06)	1.75
AGAL333.314+00.106	1.11 (0.11)	-46.60 (0.24)	4.97 (0.82)	0.22	5.62 (0.16)	-46.38 (0.08)	5.68 (0.21)	0.93
AGAL333.604−00.212	4.34 (0.10)	-47.01 (0.09)	6.53 (0.25)	0.69	15.49 (0.18)	-47.22 (0.04)	6.77 (0.10)	2.14
AGAL333.656+00.059	...	...	...	...	1.21 (0.11)	-85.26 (0.19)	4.13 (0.45)	0.28
AGAL335.789+00.174	2.53 (0.18)	-50.44 (0.17)	5.56 (0.43)	0.57	13.62 (0.12)	-50.24 (0.02)	5.36 (0.06)	2.39
AGAL336.958−00.224	...	...	...	...	2.86 (0.11)	-71.17 (0.09)	5.37 (0.25)	0.50
AGAL337.176−00.032	...	...	...	...	3.90 (0.11)	-68.17 (0.07)	5.59 (0.21)	0.66
AGAL337.258−00.101	...	...	...	...	2.10 (0.08)	-67.94 (0.07)	3.72 (0.18)	0.53
AGAL337.286+00.007	...	...	...	...	0.51 (0.10)	-105.20 (0.44)	4.44 (1.09)	0.11
AGAL337.406−00.402	7.95 (0.21)	-40.62 (0.06)	5.31 (0.15)	1.43	38.93 (0.32)	-40.83 (0.03)	6.68 (0.07)	5.48
AGAL337.704−00.054	2.81 (0.23)	-47.18 (0.20)	7.46 (0.45)	0.43	14.26 (0.15)	-47.71 (0.04)	7.93 (0.10)	1.70
AGAL337.916−00.477	9.42 (0.14)	-39.18 (0.03)	5.79 (0.09)	1.70	39.25 (0.44)	-39.21 (0.03)	5.97 (0.08)	6.17
AGAL338.066+00.044	...	...	...	...	1.12 (0.10)	-70.83 (0.29)	6.60 (0.66)	0.16
AGAL338.786+00.476	...	...	...	...	2.03 (0.08)	-64.50 (0.07)	3.87 (0.21)	0.49
AGAL338.926+00.554	6.63 (0.34)	-61.87 (0.15)	6.98 (0.38)	0.98	25.71 (0.11)	-61.24 (0.02)	7.30 (0.04)	3.30
AGAL339.623−00.122	...	...	...	...	5.30 (0.09)	-34.35 (0.04)	4.54 (0.11)	1.10
AGAL340.374−00.391	...	...	...	...	3.24 (0.12)	-43.95 (0.09)	5.31 (0.24)	0.57
AGAL340.746−01.001	1.01 (0.09)	-29.58 (0.18)	4.50 (0.42)	0.27	5.01 (0.10)	-29.72 (0.03)	3.41 (0.08)	1.38
AGAL340.784−00.097	...	...	...	...	4.28 (0.13)	-101.60 (0.09)	6.18 (0.23)	0.65
AGAL341.217−00.212	1.53 (0.13)	-43.41 (0.21)	4.95 (0.56)	0.37	9.16 (0.10)	-43.38 (0.02)	4.30 (0.06)	2.00
AGAL342.484+00.182	0.73 (0.11)	-41.53 (0.15)	1.88 (0.36)	0.34	5.61 (0.10)	-41.42 (0.03)	3.58 (0.08)	1.48
AGAL343.128−00.062	5.66 (0.19)	-31.09 (0.12)	7.11 (0.34)	0.76	26.13 (0.30)	-31.05 (0.04)	7.28 (0.11)	3.38
AGAL343.756−00.164	3.37 (0.15)	-27.75 (0.12)	4.90 (0.31)	0.64	16.36 (0.10)	-28.07 (0.01)	4.87 (0.04)	3.16
AGAL344.227−00.569	3.11 (0.18)	-21.67 (0.12)	5.04 (0.28)	0.68	15.09 (0.16)	-21.58 (0.03)	5.85 (0.07)	2.42
AGAL345.003−00.224	5.68 (0.18)	-26.95 (0.11)	6.92 (0.28)	0.83	26.57 (0.15)	-26.91 (0.02)	7.27 (0.05)	3.43
AGAL345.488+00.314	4.99 (0.20)	-17.58 (0.11)	5.46 (0.24)	0.74	17.90 (0.11)	-17.95 (0.02)	5.35 (0.04)	3.14
AGAL345.504+00.347	3.78 (0.18)	-16.91 (0.09)	4.60 (0.22)	0.86	18.45 (0.13)	-16.85 (0.02)	4.97 (0.04)	3.49
AGAL345.718+00.817	0.66 (0.13)	-11.57 (0.29)	2.80 (0.79)	0.21	3.13 (0.08)	-11.44 (0.03)	2.47 (0.08)	1.19
AGAL351.131+00.771	...	...	...	...	0.52 (0.06)	-5.37 (0.08)	1.41 (0.19)	0.35
AGAL351.161+00.697	7.76 (0.14)	-6.23 (0.05)	5.13 (0.12)	1.57	34.26 (0.15)	-6.28 (0.01)	5.09 (0.03)	6.32
AGAL351.244+00.669	4.72 (0.12)	-3.02 (0.05)	4.53 (0.13)	1.03	16.64 (0.11)	-2.92 (0.01)	4.26 (0.03)	3.67
AGAL351.571+00.762	...	...	...	...	0.30 (0.05)	-3.33 (0.11)	1.23 (0.21)	0.23
AGAL351.581−00.352	6.46 (0.15)	-95.41 (0.07)	6.86 (0.17)	0.96	25.93 (0.61)	-95.35 (0.09)	7.72 (0.21)	3.16
AGAL351.774−00.537	20.52 (0.53)	-2.68 (0.04)	8.51 (0.10)	2.22	82.74 (0.62)	-2.56 (0.04)	10.05 (0.10)	7.74
AGAL353.066+00.452	...	...	...	...	0.78 (0.07)	1.56 (0.07)	1.71 (0.19)	0.43
AGAL353.409−00.361	4.02 (0.14)	-16.27 (0.08)	5.97 (0.20)	0.72	17.12 (0.10)	-16.21 (0.02)	5.33 (0.04)	3.01
AGAL353.417−00.079	...	...	...	...	...	...	...	...
AGAL354.944−00.537	...	...	...	...	0.78 (0.08)	-5.79 (0.17)	3.64 (0.47)	0.20

Notes. "N" in the table indicates that the source has not been observed.

Table A.5. Para-H_2CO 4_{23}–3_{22} and 4_{22}–3_{21} spectral parameters.

Sources	para-H_2CO 4_{23}–3_{22}				para-H_2CO 4_{22}–3_{21}			
	$\int T_{mb} dv$	V_{lsr}	FWHM	T_{mb}	$\int T_{mb} dv$	V_{lsr}	FWHM	T_{mb}
	K km s^{-1}	km s^{-1}	km s^{-1}	K	K km s^{-1}	km s^{-1}	km s^{-1}	K
AGAL008.684−00.367	2.21 (0.11)	38.13 (0.11)	4.54 (0.28)	0.46	2.15 (0.10)	38.08 (0.09)	4.26 (0.25)	0.48
AGAL008.706−00.414	...	...	...	...	...	...	...	...
AGAL010.444−00.017	...	...	...	...	...	...	...	...
AGAL010.472+00.027	21.41 (0.45)	65.55 (0.11)	11.02 (0.27)	1.83	18.81 (0.70)	66.42 (0.18)	9.80 (0.42)	1.80
AGAL010.624−00.384	23.78 (0.32)	-3.06 (0.05)	7.36 (0.12)	3.04	23.55 (0.37)	-3.04 (0.06)	7.36 (0.14)	3.00
AGAL012.804−00.199	9.43 (0.13)	35.02 (0.04)	6.41 (0.11)	1.38	9.56 (0.12)	35.08 (0.04)	6.27 (0.09)	1.43
AGAL013.178+00.059	2.16 (0.09)	48.94 (0.09)	4.53 (0.25)	0.45	2.20 (0.09)	49.19 (0.10)	5.04 (0.24)	0.41
AGAL013.658−00.599	2.37 (0.14)	47.30 (0.23)	7.73 (0.57)	0.29	1.99 (0.11)	47.90 (0.15)	5.80 (0.40)	0.32
AGAL014.114−00.574	1.14 (0.09)	19.69 (0.14)	3.81 (0.39)	0.28	1.27 (0.07)	20.02 (0.10)	3.69 (0.26)	0.32
AGAL014.194−00.194	2.08 (0.11)	39.76 (0.12)	5.05 (0.35)	0.39	2.16 (0.08)	39.75 (0.09)	4.91 (0.23)	0.41
AGAL014.492−00.139	...	...	...	...	...	...	...	...
AGAL014.632−00.577	2.10 (0.08)	18.21 (0.06)	3.02 (0.12)	0.66	1.97 (0.07)	18.26 (0.04)	2.68 (0.11)	0.69
AGAL015.029−00.669	5.53 (0.11)	19.02 (0.04)	4.15 (0.11)	1.25	5.75 (0.09)	19.06 (0.03)	4.43 (0.09)	1.22
AGAL018.606−00.074	0.95 (0.08)	44.96 (0.19)	4.31 (0.44)	0.21	1.01 (0.08)	45.26 (0.18)	4.77 (0.42)	0.20
AGAL018.734−00.226	2.10 (0.11)	40.67 (0.17)	6.81 (0.45)	0.29	1.95 (0.09)	40.22 (0.15)	6.53 (0.38)	0.28
AGAL018.888−00.474	1.58 (0.11)	66.24 (0.16)	5.12 (0.52)	0.29	1.84 (0.09)	66.24 (0.13)	5.66 (0.39)	0.31
AGAL019.882−00.534	7.17 (0.10)	43.72 (0.03)	4.27 (0.08)	1.58	7.11 (0.08)	43.78 (0.02)	4.15 (0.06)	1.61
AGAL022.376+00.447	1.12 (0.10)	52.28 (0.16)	4.12 (0.56)	0.26	1.26 (0.08)	52.62 (0.14)	4.59 (0.41)	0.26
AGAL023.206−00.377	8.14 (0.14)	77.31 (0.06)	8.05 (0.18)	0.95	7.41 (0.12)	77.44 (0.05)	7.15 (0.15)	0.97
AGAL024.629+00.172	...	...	...	...	0.27 (0.05)	115.30 (0.19)	1.97 (0.51)	0.13
AGAL028.564−00.236	...	...	...	...	...	...	...	...
AGAL028.861+00.066	2.26 (0.11)	103.60 (0.13)	5.20 (0.32)	0.41	2.25 (0.10)	103.40 (0.10)	4.98 (0.29)	0.42
AGAL030.848−00.081	...	...	...	...	0.48 (0.08)	95.47 (0.30)	3.82 (0.65)	0.12
AGAL030.893+00.139	...	...	...	...	...	...	...	...
AGAL031.412+00.307	13.44 (0.16)	96.30 (0.05)	8.65 (0.12)	1.46	11.53 (0.27)	97.01 (0.08)	7.25 (0.20)	1.49
AGAL034.258+00.154	31.29 (0.25)	57.98 (0.03)	7.53 (0.07)	3.90	26.00 (0.46)	58.52 (0.06)	6.78 (0.14)	3.61
AGAL034.401+00.226	4.81 (0.11)	58.11 (0.06)	5.26 (0.14)	0.86	5.00 (0.10)	58.08 (0.05)	5.28 (0.14)	0.89
AGAL034.411+00.234	7.38 (0.14)	57.58 (0.05)	6.33 (0.15)	1.10	6.72 (0.12)	57.77 (0.05)	5.42 (0.13)	1.16
AGAL034.821+00.351	0.40 (0.08)	56.81 (0.23)	2.33 (0.49)	0.16	0.49 (0.07)	56.83 (0.20)	2.63 (0.39)	0.18
AGAL035.197−00.742	8.55 (0.13)	33.43 (0.05)	6.61 (0.12)	1.21	7.69 (0.11)	33.57 (0.04)	5.76 (0.10)	1.26
AGAL037.554+00.201	1.88 (0.16)	85.01 (0.26)	6.54 (0.72)	0.27	1.99 (0.14)	85.22 (0.17)	5.55 (0.49)	0.34
AGAL043.166+00.011	25.90 (0.26)	6.51 (0.07)	13.17 (0.15)	1.84	25.07 (0.62)	6.72 (0.16)	13.00 (0.37)	1.81
AGAL049.489−00.389	51.61 (0.29)	55.62 (0.03)	9.73 (0.06)	4.99	45.43 (0.74)	56.16 (0.07)	9.00 (0.18)	4.74
AGAL053.141+00.069	4.46 (0.15)	21.54 (0.07)	4.25 (0.17)	0.99	4.85 (0.15)	21.55 (0.07)	4.69 (0.18)	0.97
AGAL059.782+00.066	2.06 (0.16)	21.81 (0.14)	3.85 (0.36)	0.50	2.00 (0.13)	22.05 (0.11)	3.45 (0.27)	0.54
AGAL305.192−00.006	1.50 (0.09)	-34.70 (0.11)	3.73 (0.28)	0.38	1.41 (0.09)	-34.64 (0.09)	3.44 (0.30)	0.39
AGAL305.209+00.206	12.54 (0.15)	-40.95 (0.04)	7.51 (0.11)	1.57	11.53 (0.14)	-40.76 (0.04)	7.19 (0.10)	1.51
AGAL305.562+00.014	1.97 (0.09)	-39.57 (0.08)	3.67 (0.21)	0.50	2.01 (0.08)	-39.45 (0.06)	3.27 (0.16)	0.58
AGAL305.794−00.096	...	...	...	...	...	...	...	...
AGAL309.384−00.134	1.64 (0.09)	-51.23 (0.12)	4.60 (0.30)	0.33	1.91 (0.08)	-51.21 (0.09)	4.49 (0.23)	0.40
AGAL310.014+00.387	1.47 (0.10)	-41.04 (0.16)	4.97 (0.43)	0.28	1.61 (0.09)	-40.65 (0.13)	4.88 (0.34)	0.31
AGAL313.576+00.324	2.20 (0.10)	-46.59 (0.13)	5.66 (0.32)	0.37	2.47 (0.09)	-46.13 (0.11)	6.04 (0.27)	0.38
AGAL316.641−00.087	1.31 (0.09)	-18.44 (0.19)	5.39 (0.47)	0.23	1.51 (0.11)	-18.40 (0.21)	6.07 (0.55)	0.23
AGAL317.867−00.151	2.77 (0.10)	-40.70 (0.08)	5.02 (0.21)	0.52	2.97 (0.09)	-40.90 (0.07)	4.93 (0.19)	0.57
AGAL318.779−00.137	0.99 (0.10)	-39.89 (0.21)	4.58 (0.63)	0.20	1.35 (0.10)	-39.44 (0.21)	6.01 (0.58)	0.21
AGAL320.881−00.397	...	...	...	...	...	...	...	...
AGAL326.661+00.519	0.84 (0.08)	-39.57 (0.13)	2.89 (0.35)	0.27	0.77 (0.07)	-39.57 (0.10)	2.45 (0.24)	0.30
AGAL326.987−00.032	1.97 (0.14)	-57.61 (0.17)	5.94 (0.60)	0.31	1.95 (0.11)	-57.68 (0.13)	5.23 (0.40)	0.35
AGAL327.119+00.509	2.18 (0.11)	-84.52 (0.20)	7.27 (0.42)	0.28	1.65 (0.10)	-84.27 (0.17)	5.37 (0.41)	0.29
AGAL327.293−00.579	33.13 (0.17)	-44.88 (0.02)	8.61 (0.05)	3.61	28.61 (0.21)	-44.33 (0.03)	7.46 (0.06)	3.61
AGAL327.393+00.199	1.70 (0.09)	-88.88 (0.11)	4.01 (0.28)	0.40	1.70 (0.09)	-88.89 (0.10)	4.21 (0.29)	0.38
AGAL328.809+00.632	28.51 (0.12)	-41.62 (0.01)	6.36 (0.03)	4.20	27.71 (0.13)	-41.53 (0.01)	6.03 (0.03)	4.32
AGAL329.029−00.206	3.82 (0.13)	-43.79 (0.11)	6.82 (0.28)	0.53	3.24 (0.10)	-43.58 (0.08)	5.69 (0.22)	0.54
AGAL329.066−00.307	1.56 (0.12)	-41.84 (0.17)	4.92 (0.49)	0.30	1.64 (0.10)	-41.87 (0.11)	3.99 (0.31)	0.39
AGAL330.879−00.367	15.81 (0.14)	-62.35 (0.04)	8.40 (0.09)	1.77	14.24 (0.17)	-61.95 (0.05)	7.96 (0.11)	1.68
AGAL330.954−00.182	24.67 (0.14)	-92.54 (0.03)	10.22 (0.07)	2.26	23.51 (0.13)	-92.42 (0.03)	10.02 (0.07)	2.20
AGAL331.709+00.582	2.72 (0.14)	-66.81 (0.13)	5.72 (0.42)	0.45	2.66 (0.13)	-66.47 (0.14)	5.72 (0.35)	0.44
AGAL332.094−00.421	1.97 (0.12)	-57.79 (0.16)	5.33 (0.40)	0.35	1.59 (0.08)	-57.01 (0.11)	4.44 (0.23)	0.34

Table A.5. continued.

Sources	para-H_2CO 4_{23}–3_{22}				para-H_2CO 4_{22}–3_{21}			
	$\int T_{mb} dv$	V_{lsr}	FWHM	T_{mb}	$\int T_{mb} dv$	V_{lsr}	FWHM	T_{mb}
	K km s^{-1}	km s^{-1}	km s^{-1}	K	K km s^{-1}	km s^{-1}	km s^{-1}	K
AGAL332.826−00.549	14.31 (0.14)	-57.68 (0.03)	6.30 (0.07)	2.13	12.98 (0.15)	-57.50 (0.03)	5.65 (0.08)	2.16
AGAL333.134−00.431	12.37 (0.12)	-53.49 (0.03)	6.72 (0.08)	1.72	11.33 (0.11)	-53.35 (0.03)	6.39 (0.08)	1.67
AGAL333.284−00.387	2.41 (0.09)	-52.23 (0.07)	3.74 (0.17)	0.60	2.48 (0.08)	-52.15 (0.06)	3.75 (0.14)	0.62
AGAL333.314+00.106	1.41 (0.16)	-46.59 (0.24)	4.25 (0.67)	0.31	1.53 (0.14)	-46.68 (0.23)	5.00 (0.55)	0.29
AGAL333.604−00.212	7.07 (0.18)	-47.14 (0.08)	6.96 (0.23)	0.95	6.47 (0.16)	-47.13 (0.07)	6.16 (0.19)	0.99
AGAL333.656+00.059	...	...	...	...	...	...	...	...
AGAL335.789+00.174	5.02 (0.11)	-50.38 (0.05)	5.39 (0.15)	0.88	4.52 (0.09)	-50.28 (0.04)	4.54 (0.11)	0.93
AGAL336.958−00.224	1.16 (0.12)	-71.19 (0.34)	6.93 (0.93)	0.16	0.96 (0.08)	-71.45 (0.19)	4.58 (0.51)	0.20
AGAL337.176−00.032	1.18 (0.12)	-68.24 (0.26)	5.72 (0.83)	0.19	0.95 (0.10)	-67.69 (0.28)	5.78 (0.79)	0.16
AGAL337.258−00.101	0.82 (0.09)	-67.93 (0.26)	4.82 (0.64)	0.16	0.53 (0.07)	-68.33 (0.23)	3.41 (0.51)	0.15
AGAL337.286+00.007	...	...	...	...	...	...	...	...
AGAL337.406−00.402	22.17 (0.13)	-40.67 (0.02)	6.98 (0.05)	2.99	20.41 (0.21)	-40.43 (0.03)	6.42 (0.08)	2.99
AGAL337.704−00.054	7.55 (0.12)	-48.00 (0.06)	8.34 (0.15)	0.85	6.79 (0.15)	-47.79 (0.08)	7.85 (0.20)	0.81
AGAL337.916−00.477	21.96 (0.14)	-39.37 (0.02)	6.28 (0.05)	3.28	21.54 (0.16)	-39.22 (0.02)	6.03 (0.06)	3.36
AGAL338.066+00.044	...	...	...	...	...	...	...	...
AGAL338.786+00.476	...	...	...	...	0.41 (0.06)	-64.45 (0.26)	3.28 (0.59)	0.12
AGAL338.926+00.554	8.51 (0.11)	-61.18 (0.04)	6.97 (0.11)	1.15	8.41 (0.11)	-61.03 (0.04)	6.78 (0.11)	1.17
AGAL339.623−00.122	2.02 (0.09)	-34.32 (0.13)	5.66 (0.31)	0.33	1.84 (0.09)	-34.66 (0.12)	5.50 (0.35)	0.31
AGAL340.374−00.391	1.19 (0.11)	-44.16 (0.23)	4.82 (0.53)	0.23	1.09 (0.11)	-43.98 (0.23)	4.96 (0.73)	0.21
AGAL340.746−01.001	1.14 (0.09)	-29.76 (0.15)	3.73 (0.35)	0.29	1.33 (0.09)	-29.71 (0.12)	3.80 (0.28)	0.33
AGAL340.784−00.097	2.23 (0.15)	-102.00 (0.24)	7.86 (0.68)	0.27	1.58 (0.11)	-102.30 (0.20)	5.53 (0.45)	0.27
AGAL341.217−00.212	3.15 (0.13)	-43.40 (0.09)	4.99 (0.28)	0.59	2.95 (0.09)	-43.41 (0.06)	4.46 (0.18)	0.62
AGAL342.484+00.182	1.83 (0.12)	-41.26 (0.13)	4.48 (0.37)	0.38	1.88 (0.09)	-41.60 (0.09)	3.83 (0.21)	0.46
AGAL343.128−00.062	13.27 (0.14)	-31.26 (0.04)	7.89 (0.10)	1.58	13.17 (0.11)	-31.02 (0.03)	7.71 (0.08)	1.61
AGAL343.756−00.164	6.64 (0.09)	-28.05 (0.03)	5.19 (0.09)	1.20	6.69 (0.09)	-28.05 (0.03)	4.90 (0.08)	1.28
AGAL344.227−00.569	8.08 (0.13)	-21.77 (0.05)	6.32 (0.12)	1.20	7.63 (0.22)	-21.56 (0.08)	5.67 (0.20)	1.26
AGAL345.003−00.224	12.95 (0.11)	-27.44 (0.03)	7.45 (0.08)	1.64	11.54 (0.16)	-27.01 (0.04)	6.64 (0.12)	1.64
AGAL345.488+00.314	6.82 (0.12)	-18.09 (0.05)	5.84 (0.13)	1.10	6.61 (0.11)	-18.02 (0.05)	5.87 (0.11)	1.06
AGAL345.504+00.347	11.62 (0.15)	-17.40 (0.04)	6.83 (0.11)	1.59	9.37 (0.16)	-17.04 (0.05)	5.73 (0.11)	1.54
AGAL345.718+00.817	0.59 (0.07)	-11.32 (0.11)	1.88 (0.28)	0.29	0.73 (0.07)	-11.50 (0.12)	2.50 (0.26)	0.28
AGAL351.131+00.771	...	...	...	...	...	...	...	...
AGAL351.161+00.697	16.43 (0.24)	-6.46 (0.04)	5.25 (0.10)	2.94	15.33 (0.11)	-6.39 (0.02)	4.96 (0.04)	2.90
AGAL351.244+00.669	6.26 (0.36)	-2.76 (0.12)	4.35 (0.31)	1.35	6.31 (0.09)	-2.85 (0.03)	4.46 (0.08)	1.33
AGAL351.571+00.762	...	...	...	...	...	...	...	...
AGAL351.581−00.352	20.20 (0.30)	-95.72 (0.06)	7.59 (0.14)	2.51	17.75 (0.71)	-95.31 (0.13)	6.63 (0.31)	2.51
AGAL351.774−00.537	60.68 (0.31)	-3.31 (0.03)	10.50 (0.07)	5.43	54.33 (0.37)	-2.95 (0.03)	9.51 (0.08)	5.36
AGAL353.066+00.452	...	...	...	...	...	...	...	...
AGAL353.409−00.361	6.13 (0.09)	-16.10 (0.04)	4.92 (0.09)	1.17	6.23 (0.08)	-16.07 (0.03)	4.86 (0.08)	1.20
AGAL353.417−00.079	...	...	...	...	...	...	...	...
AGAL354.944−00.537	...	...	...	...	...	...	...	...

Table A.6. Beam filling factors, integrated intensity ratios, para-H_2CO column densities, spatial densities, and kinetic temperatures.

Sources	η_{bf}		$I'(4_{04}-3_{03})$	N(p-H_2CO)	N(o-H_2CO)	$n(H_2)$	Kinetic temperature			
	$3_{03}-2_{02}$	$4_{04}-3_{03}$	$I'(3_{03}-2_{02})$	$4_{04}-3_{03}/3_{03}-2_{02}$			$3_{21}-2_{20}/3_{03}-2_{02}$	T_{LTE}	$4_{22}-3_{21}/4_{04}-3_{03}$	T_{LTE}
				cm^{-2}	cm^{-2}	cm^{-3}	K	K	K	K
AGAL008.684−00.367	0.452	0.594	1.07±0.04	2.8×10^{13}	7.2×10^{13}	$1.9^{+0.3}_{-0.2}\times10^{6}$	$52.7^{+9.7}_{-8.0}$	$45.7^{+6.1}_{-5.4}$	$55.4^{+4.2}_{-3.5}$	$47.8^{+2.4}_{-2.3}$
AGAL008.706−00.414	0.613	0.737	1.26±0.27	...	...	...	...	...	...	...
AGAL010.444−00.017	0.452	0.594	...	...	...	...	...	...	...	...
AGAL010.472+00.027	0.372	0.511	1.57±0.05	2.1×10^{14}	3.9×10^{14}	$2.1^{+0.4}_{-0.2}\times10^{6}$	>300	$278.8^{+110}_{-64.0}$	>300	>300
AGAL010.624−00.384	0.452	0.594	1.50±0.03	3.0×10^{14}	6.1×10^{14}	$8.1^{+0.3}_{-0.3}\times10^{6}$	$106.6^{+10.8}_{-16.6}$	$97.5^{+5.2}_{-4.8}$	$107.4^{+8.7}_{-8.3}$	$99.1^{+5.2}_{-4.9}$
AGAL012.804−00.199	0.571	0.702	1.32±0.02	8.1×10^{13}	1.6×10^{14}	$2.7^{+0.1}_{-0.2}\times10^{6}$	$86.3^{+8.3}_{-9.4}$	$72.1^{+5.5}_{-5.0}$	$98.1^{+2.6}_{-2.9}$	$81.6^{+1.9}_{-1.9}$
AGAL013.178+00.059	0.586	0.714	1.11±0.04	2.3×10^{13}	4.8×10^{13}	$1.5^{+0.2}_{-0.2}\times10^{6}$	<130	$98.7^{+28.7}_{-19.9}$	$63.8^{+4.1}_{-4.3}$	$53.4^{+2.6}_{-2.5}$
AGAL013.658−00.599	0.452	0.594	0.99±0.08	2.1×10^{13}	4.4×10^{13}	$1.1^{+0.2}_{-0.2}\times10^{6}$	...	...	$92.5^{+7.8}_{-9.7}$	$71.6^{+7.0}_{-6.2}$
AGAL014.114−00.574	0.556	0.689	1.13±0.03	1.5×10^{13}	3.1×10^{13}	$5.2^{+1.9}_{-1.1}\times10^{6}$	$65.4^{+17.5}_{-14.1}$	$55.1^{+11.6}_{-9.4}$	$45.6^{+3.8}_{-3.8}$	$41.2^{+3.8}_{-2.1}$
AGAL014.194−00.194	0.489	0.629	0.86±0.03	2.5×10^{13}	7.5×10^{13}	$9.5^{+0.9}_{-0.7}\times10^{5}$	$64.4^{+11.5}_{-9.3}$	$53.5^{+8.1}_{-6.9}$	$77.2^{+4.8}_{-4.8}$	$61.6^{+3.5}_{-3.2}$
AGAL014.492−00.139	0.600	0.726	0.87±0.11	...	...	...	...	...	...	...
AGAL014.632−00.577	0.571	0.702	1.48±0.05	2.7×10^{13}	2.7×10^{13}	$1.3^{+0.5}_{-0.3}\times10^{6}$	$98.6^{+21.5}_{-18.2}$	$80.3^{+16.5}_{-12.8}$	$49.7^{+2.4}_{-2.5}$	$43.1^{+1.4}_{-1.4}$
AGAL015.029−00.669	0.650	0.767	0.91±0.01	6.2×10^{13}	1.7×10^{14}	$1.3^{+0.1}_{-0.1}\times10^{6}$	$78.3^{+5.6}_{-5.3}$	$66.8^{+4.2}_{-3.9}$	$60.5^{+1.3}_{-1.5}$	$52.8^{+1.0}_{-1.0}$
AGAL018.606−00.074	0.507	0.645	1.32±0.10	1.1×10^{13}	2.3×10^{13}	$8.3^{+3.7}_{-4.6}\times10^{6}$	...	...	$63.5^{+12.0}_{-9.1}$	$56.0^{+5.7}_{-5.1}$
AGAL018.734−00.226	0.507	0.645	0.88±0.03	2.4×10^{13}	4.9×10^{13}	$1.0^{+0.1}_{-0.1}\times10^{6}$	$45.4^{+5.8}_{-5.5}$	$39.0^{+4.2}_{-3.9}$	$69.2^{+4.8}_{-5.0}$	$55.4^{+3.4}_{-3.2}$
AGAL018.888−00.474	0.556	0.689	0.82±0.03	2.1×10^{13}	4.5×10^{13}	$9.5^{+0.8}_{-0.8}\times10^{5}$	$43.6^{+5.2}_{-4.8}$	$37.5^{+3.8}_{-3.6}$	$68.5^{+5.1}_{-4.8}$	$55.0^{+3.6}_{-3.3}$
AGAL019.882−00.534	0.452	0.594	1.25±0.02	7.7×10^{13}	1.2×10^{14}	$2.4^{+0.1}_{-0.2}\times10^{6}$	$81.7^{+5.9}_{-8.2}$	$70.0^{+4.8}_{-4.4}$	$80.2^{+2.2}_{-2.3}$	$69.9^{+1.3}_{-1.3}$
AGAL022.376+00.447	0.433	0.575	1.06±0.06	1.4×10^{13}	2.3×10^{13}	$1.4^{+0.3}_{-0.2}\times10^{6}$	...	...	$82.2^{+12.8}_{-7.8}$	$66.5^{+7.2}_{-6.3}$
AGAL023.206−00.377	0.413	0.555	1.82±0.06	$>8.0\times10^{13}$	...	...	...	$106.5^{+28.1}_{-19.9}$	...	$92.0^{+3.4}_{-3.2}$
AGAL024.629+00.172	0.489	0.629	1.88±0.32	$>4.8\times10^{12}$	...	...	...	...	...	$30.8^{+4.4}_{-4.1}$
AGAL028.564−00.236	0.662	0.776	2.16±0.41	...	...	...	...	...	...	...
AGAL028.861+00.066	0.471	0.612	...	...	...	...	...	...	...	$70.9^{+5.2}_{-4.7}$
AGAL030.848−00.081	0.540	0.675	0.95±0.10	6.4×10^{12}	1.8×10^{13}	$1.5^{+0.6}_{-0.4}\times10^{6}$	...	...	$49.5^{+10.0}_{-8.8}$	$41.1^{+6.3}_{-5.6}$
AGAL030.893+00.139	0.571	0.702	1.04±0.41	...	...	...	...	...	...	...
AGAL031.412+00.307	0.393	0.534	1.96±0.09	$>1.2\times10^{14}$	...	...	>280	>280	>280	$370.8^{+93.5}_{-63.5}$
AGAL034.258+00.154	0.452	0.594	1.44±0.02	2.6×10^{14}	3.3×10^{14}	$2.1^{+0.1}_{-0.1}\times10^{6}$	$174.0^{+12.5}_{-14.5}$	$142.0^{+8.8}_{-8.0}$	$209.0^{+15.1}_{-11.4}$	$205.2^{+19.7}_{-16.9}$
AGAL034.401+00.226	0.556	0.689	1.07±0.03	4.7×10^{13}	9.1×10^{13}	$2.2^{+0.2}_{-0.2}\times10^{6}$	$66.5^{+8.7}_{-7.9}$	$55.4^{+5.5}_{-4.9}$	$67.0^{+2.8}_{-2.4}$	$56.9^{+1.6}_{-1.5}$
AGAL034.411+00.234	0.433	0.575	1.03±0.02	7.5×10^{13}	1.3×10^{14}	$1.0^{+0.1}_{-0.1}\times10^{6}$	$89.0^{+11.8}_{-10.4}$	$72.9^{+7.1}_{-6.3}$	$108.7^{+5.2}_{-5.1}$	$87.4^{+3.4}_{-3.2}$
AGAL034.821+00.351	0.600	0.726	0.73±0.06	8.2×10^{12}	2.7×10^{13}	$9.5^{+2.0}_{-2.1}\times10^{5}$	...	...	$45.2^{+6.5}_{-6.2}$	$37.4^{+4.7}_{-4.3}$
AGAL035.197−00.742	0.507	0.645	1.01±0.01	7.6×10^{13}	1.1×10^{14}	$1.1^{+0.1}_{-0.1}\times10^{6}$	$104.8^{+7.2}_{-7.4}$	$74.8^{+5.6}_{-5.0}$	$92.0^{+1.9}_{-2.5}$	$75.7^{+1.9}_{-1.8}$
AGAL037.554+00.201	0.471	0.612	1.19±0.06	1.8×10^{13}	3.1×10^{13}	$1.8^{+0.4}_{-0.3}\times10^{6}$	$87.4^{+27.6}_{-21.2}$	$68.9^{+17.9}_{-13.4}$	$96.0^{+14.0}_{-12.8}$	$75.5^{+9.7}_{-8.3}$
AGAL043.166+00.011	0.471	0.612	1.85±0.13	$>2.3\times10^{14}$	...	...	...	$117.6^{+75.8}_{-37.3}$	...	$153.9^{+31.4}_{-23.3}$
AGAL049.489−00.389	0.413	0.555	1.19±0.01	5.0×10^{14}	7.1×10^{14}	$1.3^{+0.1}_{-0.1}\times10^{6}$	$225.1^{+21.3}_{-17.8}$	$192.2^{+8.0}_{-7.4}$	$169.6^{+9.6}_{-8.7}$	$160.9^{+11.2}_{-10.0}$
AGAL053.141+00.069	0.452	0.594	1.02±0.02	5.7×10^{13}	1.2×10^{14}	$1.3^{+0.7}_{-0.1}\times10^{6}$	$78.8^{+6.3}_{-5.2}$	$68.1^{+6.0}_{-5.4}$	$74.2^{+3.9}_{-4.0}$	$63.2^{+2.6}_{-2.7}$
AGAL059.782+00.066	0.540	0.675	...	...	...	...	...	...	...	$60.2^{+5.6}_{-5.0}$
AGAL305.192−00.006	0.507	0.645	0.90±0.03	1.7×10^{13}	4.1×10^{13}	$1.2^{+0.1}_{-0.1}\times10^{6}$	$58.3^{+10.8}_{-6.3}$	$48.7^{+6.1}_{-5.4}$	$64.5^{+5.9}_{-5.5}$	$52.2^{+3.9}_{-3.6}$
AGAL305.209+00.206	0.471	0.612	1.15±0.01	1.2×10^{14}	2.2×10^{14}	$1.5^{+0.1}_{-0.1}\times10^{6}$	$105.1^{+7.6}_{-6.7}$	$86.3^{+4.5}_{-4.2}$	$97.4^{+2.7}_{-2.6}$	$81.3^{+2.0}_{-1.9}$
AGAL305.562+00.014	0.471	0.612	0.94±0.02	2.8×10^{13}	7.0×10^{13}	$1.4^{+0.1}_{-0.1}\times10^{6}$	$63.1^{+7.6}_{-6.8}$	$52.6^{+5.1}_{-4.6}$	$56.3^{+2.9}_{-2.8}$	$48.1^{+2.0}_{-1.9}$
AGAL305.794−00.096	0.571	0.702	0.85±0.17	...	...	...	...	...	...	...
AGAL309.384−00.134	0.507	0.645	0.76±0.02	2.4×10^{13}	7.1×10^{13}	$7.1^{+0.7}_{-0.7}\times10^{5}$	$78.0^{+9.8}_{-0.7}$	$66.9^{+8.5}_{-7.3}$	$76.7^{+4.8}_{-4.9}$	$61.2^{+3.7}_{-3.4}$
AGAL310.014+00.387	0.524	0.661	0.98±0.04	1.5×10^{13}	3.4×10^{13}	$1.1^{+0.1}_{-0.1}\times10^{6}$	$102.7^{+21.3}_{-21.9}$	$78.9^{+17.2}_{-13.2}$	$89.1^{+8.4}_{-8.4}$	$70.2^{+6.5}_{-5.8}$
AGAL313.576+00.324	0.393	0.534	...	...	...	...	...	...	...	$65.4^{+3.9}_{-3.6}$
AGAL316.641−00.087	0.413	0.555	...	...	...	...	...	...	...	$165.7^{+61.8}_{-37.7}$
AGAL317.867−00.151	0.413	0.555	0.87±0.02	4.0×10^{13}	7.9×10^{13}	$9.9^{+0.7}_{-0.6}\times10^{5}$	$78.9^{+6.6}_{-11.2}$	$63.1^{+6.4}_{-5.7}$	$74.6^{+3.7}_{-3.8}$	$60.1^{+2.6}_{-2.5}$
AGAL318.779−00.137	0.586	0.714	1.19±0.08	1.1×10^{13}	1.7×10^{13}	$1.9^{+0.5}_{-0.4}\times10^{6}$	$76.1^{+17.3}_{-23.2}$	$63.0^{+20.2}_{-14.4}$	$88.6^{+13.4}_{-13.6}$	$70.0^{+9.0}_{-7.7}$
AGAL320.881−00.397	0.471	0.612	0.56±0.07	...	...	...	...	...	...	...
AGAL326.661+00.519	0.507	0.645	0.69±0.02	1.8×10^{13}	6.9×10^{13}	$7.7^{+0.7}_{-0.7}\times10^{5}$	$74.5^{+18.1}_{-10.8}$	$66.4^{+12.8}_{-10.2}$	$43.0^{+3.4}_{-3.3}$	$36.3^{+2.5}_{-2.4}$
AGAL326.987−00.032	0.433	0.575	0.91±0.03	2.4×10^{13}	4.5×10^{13}	$1.1^{+0.1}_{-0.1}\times10^{6}$	$54.2^{+8.7}_{-7.9}$	$45.2^{+6.2}_{-5.5}$	$78.0^{+7.1}_{-6.9}$	$62.1^{+5.1}_{-4.6}$
AGAL327.119+00.509	0.471	0.612	0.94±0.05	1.6×10^{13}	2.7×10^{13}	$6.7^{+1.1}_{-0.1}\times10^{5}$	...	...	$144.8^{+23.8}_{-19.2}$	$116.0^{+25.6}_{-17.8}$
AGAL327.293−00.579	0.393	0.534	1.19±0.06	...	...	...	...	...	...	...
AGAL327.393+00.199	0.489	0.629	0.79±0.02	2.5×10^{13}	8.7×10^{13}	$9.0^{+0.9}_{-0.8}\times10^{5}$	$53.1^{+6.2}_{-5.6}$	$45.3^{+5.0}_{-4.5}$	$58.4^{+4.1}_{-3.7}$	$48.8^{+2.9}_{-2.7}$
AGAL328.809+00.632	0.433	0.575	1.34±0.01	3.2×10^{14}	4.2×10^{14}	$2.7^{+0.1}_{-0.1}\times10^{6}$	$153.7^{+6.4}_{-9.7}$	$122.4^{+4.9}_{-4.6}$	$110.9^{+1.6}_{-1.6}$	$102.0^{+1.5}_{-1.5}$
AGAL329.029−00.206	0.600	0.726	0.74±0.02	3.8×10^{13}	8.5×10^{13}	$7.2^{+0.4}_{-0.5}\times10^{5}$	$108.0^{+7.0}_{-6.7}$	$91.9^{+9.5}_{-8.2}$	$69.2^{+3.2}_{-3.2}$	$56.0^{+2.3}_{-2.2}$
AGAL329.066−00.307	0.586	0.714	0.78±0.02	2.2×10^{13}	5.2×10^{13}	$1.2^{+0.1}_{-0.1}\times10^{6}$	$64.3^{+7.5}_{-6.7}$	$54.2^{+6.3}_{-5.7}$	$51.7^{+3.4}_{-3.5}$	$42.9^{+2.5}_{-2.4}$
AGAL330.879−00.367	0.433	0.575	1.07±0.01	1.5×10^{14}	2.1×10^{14}	$7.5^{+0.4}_{-0.3}\times10^{5}$	$159.7^{+11.3}_{-10.9}$	$134.3^{+10.1}_{-9.0}$	$206.9^{+7.8}_{-5.9}$	$204.1^{+12.1}_{-10.9}$
AGAL330.954−00.182	0.393	0.534	1.12±0.04	2.6×10^{14}	3.5×10^{14}	$9.5^{+0.6}_{-0.1}\times10^{5}$	$196.3^{+18.4}_{-16.8}$	$163.7^{+9.2}_{-8.4}$	$199.1^{+19.1}_{-19.2}$	$199.0^{+30.3}_{-23.9}$
AGAL331.709+00.582	0.489	0.629	0.79±0.02	3.6×10^{13}	9.3×10^{13}	$8.3^{+0.7}_{-0.7}\times10^{5}$	$78.5^{+10.0}_{-8.3}$	$65.4^{+7.4}_{-6.5}$	$66.3^{+4.7}_{-4.7}$	$53.8^{+3.3}_{-3.1}$
AGAL332.094−00.421	0.471	0.612	0.97±0.03	1.8×10^{13}	4.0×10^{13}	$1.3^{+0.1}_{-0.1}\times10^{6}$	$76.0^{+16.7}_{-13.5}$	$61.4^{+8.1}_{-7.0}$	$73.2^{+6.1}_{-5.4}$	$59.0^{+4.0}_{-3.7}$

Table A.6. continued.

Sources	η_{bf}		$I'(4_{04}-3_{03})$	N(p-H_2CO)	N(o-H_2CO)	$n(H_2)$	Kinetic temperature			
	$3_{03}-2_{02}$	$4_{04}-3_{03}$	$I'(3_{03}-2_{02})$	$4_{04}-3_{03}/3_{03}-2_{02}$			$3_{21}-2_{20}/3_{03}-2_{02}$	T_{LTE}	$4_{22}-3_{21}/4_{04}-3_{03}$	T_{LTE}
				cm^{-2}	cm^{-2}	cm^{-3}	K	K	K	K
AGAL332.826−00.549	0.433	0.575	1.15±0.01	1.4×10^{14}	2.1×10^{14}	$1.2^{+0.1}_{-0.1}\times10^{6}$	$145.5^{+9.3}_{-7.1}$	$116.7^{+5.6}_{-5.2}$	$132.1^{+3.7}_{-3.8}$	$111.5^{+3.4}_{-3.3}$
AGAL333.134−00.431	0.524	0.661	0.85±0.01	1.4×10^{14}	3.7×10^{14}	$6.5^{+0.3}_{-0.2}\times10^{5}$	$94.9^{+6.1}_{-5.8}$	$83.4^{+2.9}_{-2.8}$	$87.8^{+1.8}_{-1.9}$	$75.9^{+1.5}_{-1.4}$
AGAL333.284−00.387	0.586	0.714	0.89±0.02	2.7×10^{13}	7.1×10^{13}	$1.2^{+0.1}_{-0.1}\times10^{6}$	$79.8^{+10.2}_{-8.7}$	$63.6^{+8.5}_{-7.3}$	$63.1^{+3.0}_{-2.7}$	$51.8^{+1.9}_{-1.8}$
AGAL333.314+00.106	0.489	0.629	0.77±0.03	2.5×10^{13}	7.1×10^{13}	$8.0^{+0.1}_{-0.1}\times10^{5}$	$52.8^{+5.7}_{-5.6}$	$47.1^{+5.9}_{-5.2}$	$57.0^{+7.1}_{-6.9}$	$46.6^{+4.7}_{-4.3}$
AGAL333.604−00.212	0.571	0.702	0.84±0.01	6.7×10^{13}	2.0×10^{14}	$6.4^{+0.3}_{-0.4}\times10^{5}$	$92.6^{+6.5}_{-5.7}$	$84.7^{+5.1}_{-4.7}$	$93.0^{+5.0}_{-4.5}$	$80.7^{+3.8}_{-3.6}$
AGAL333.656+00.059	0.571	0.702	0.80±0.10	...	...	...	...	...	...	...
AGAL335.789+00.174	0.489	0.629	0.95±0.02	5.1×10^{13}	1.1×10^{14}	$1.3^{+0.1}_{-0.1}\times10^{6}$	$96.0^{+12.8}_{-11.3}$	$76.0^{+8.9}_{-7.6}$	$69.7^{+2.7}_{-2.5}$	$57.9^{+1.5}_{-1.5}$
AGAL336.958−00.224	0.393	0.534	0.87±0.07	1.4×10^{13}	3.5×10^{13}	$9.5^{+2.1}_{-1.8}\times10^{5}$	...	...	$74.9^{+10.7}_{-9.8}$	$58.7^{+7.5}_{-6.5}$
AGAL337.176−00.032	0.556	0.689	0.94±0.06	1.2×10^{13}	2.4×10^{13}	$1.5^{+0.4}_{-0.3}\times10^{6}$	...	...	$51.1^{+6.5}_{-6.4}$	$42.2^{+4.3}_{-4.0}$
AGAL337.258−00.101	0.471	0.612	0.68±0.06	1.1×10^{13}	3.0×10^{13}	$6.3^{+1.4}_{-1.5}\times10^{5}$	...	...	$53.8^{+8.0}_{-7.6}$	$43.4^{+5.9}_{-5.2}$
AGAL337.286+00.007	0.586	0.714	...	...	...	...	...	...	...	...
AGAL337.406−00.402	0.452	0.594	1.25±0.02	2.1×10^{14}	2.7×10^{14}	$1.5^{+0.1}_{-0.1}\times10^{6}$	$111.8^{+8.7}_{-8.2}$	$97.2^{+5.4}_{-5.0}$	$151.0^{+6.3}_{-6.4}$	$131.7^{+5.0}_{-4.7}$
AGAL337.704−00.054	0.433	0.575	0.94±0.02	7.3×10^{13}	1.2×10^{14}	$7.1^{+0.6}_{-0.4}\times10^{5}$	$94.2^{+12.3}_{-11.0}$	$75.2^{+7.6}_{-6.7}$	$128.6^{+6.8}_{-6.5}$	$103.8^{+5.7}_{-5.3}$
AGAL337.916−00.477	0.413	0.555	1.13±0.02	2.4×10^{14}	3.1×10^{14}	$1.1^{+0.1}_{-0.1}\times10^{6}$	$165.4^{+12.6}_{-12.4}$	$147.3^{+7.6}_{-7.0}$	$159.6^{+5.4}_{-8.0}$	$151.0^{+6.7}_{-6.3}$
AGAL338.066+00.044	0.600	0.726	0.84±0.11	...	...	...	...	...	...	...
AGAL338.786+00.476	0.571	0.702	0.77±0.06	7.1×10^{12}	1.9×10^{13}	$1.1^{+0.3}_{-0.2}\times10^{6}$	...	...	$43.2^{+6.5}_{-6.4}$	$35.9^{+4.7}_{-4.3}$
AGAL338.926+00.554	0.600	0.726	0.93±0.00	9.0×10^{13}	2.1×10^{14}	$1.2^{+0.1}_{-0.1}\times10^{6}$	$103.0^{+6.8}_{-5.8}$	$85.1^{+7.2}_{-6.4}$	$66.9^{+1.2}_{-1.7}$	$56.9^{+1.0}_{-1.0}$
AGAL339.623−00.122	0.540	0.675	0.84±0.04	2.1×10^{13}	5.2×10^{13}	$7.7^{+0.8}_{-0.8}\times10^{5}$	...	...	$77.3^{+6.2}_{-5.6}$	$61.4^{+4.3}_{-4.0}$
AGAL340.374−00.391	0.489	0.629	0.97±0.07	1.2×10^{13}	2.2×10^{13}	$1.2^{+0.3}_{-0.2}\times10^{6}$	...	...	$74.9^{+12.5}_{-12.5}$	$58.5^{+8.9}_{-7.5}$
AGAL340.746−01.001	0.507	0.645	0.72±0.02	2.3×10^{13}	5.2×10^{13}	$7.0^{+0.5}_{-0.6}\times10^{5}$	$64.8^{+7.5}_{-6.7}$	$55.0^{+5.7}_{-5.1}$	$54.2^{+4.2}_{-4.1}$	$45.3^{+3.0}_{-2.8}$
AGAL340.784−00.097	0.413	0.555	0.98±0.08	1.9×10^{13}	3.5×10^{13}	$1.1^{+0.3}_{-0.2}\times10^{6}$	...	...	$86.0^{+10.4}_{-11.0}$	$66.6^{+7.9}_{-6.9}$
AGAL341.217−00.212	0.452	0.594	0.99±0.03	3.6×10^{13}	6.9×10^{13}	$1.4^{+0.1}_{-0.1}\times10^{6}$	$79.2^{+10.4}_{-9.0}$	$66.6^{+9.6}_{-8.1}$	$66.6^{+3.7}_{-3.0}$	$55.9^{+2.2}_{-2.1}$
AGAL342.484+00.182	0.433	0.575	1.16±0.05	2.1×10^{13}	3.7×10^{13}	$2.1^{+0.4}_{-0.3}\times10^{6}$	$48.8^{+10.9}_{-10.3}$	$43.4^{+6.9}_{-6.0}$	$70.5^{+6.6}_{-6.3}$	$58.7^{+3.8}_{-3.6}$
AGAL343.128−00.062	0.471	0.612	1.23±0.02	1.2×10^{14}	1.6×10^{14}	$1.4^{+0.1}_{-0.1}\times10^{6}$	$128.2^{+11.3}_{-11.9}$	$102.5^{+9.7}_{-8.5}$	$143.4^{+5.9}_{-5.7}$	$118.6^{+4.4}_{-4.1}$
AGAL343.756−00.164	0.413	0.555	1.17±0.02	7.4×10^{13}	1.1×10^{14}	$1.8^{+0.1}_{-0.2}\times10^{6}$	$106.9^{+12.7}_{-10.7}$	$85.9^{+9.1}_{-7.9}$	$92.1^{+3.4}_{-2.6}$	$77.9^{+1.9}_{-1.9}$
AGAL344.227−00.569	0.433	0.575	1.09±0.03	7.9×10^{13}	4.4×10^{13}	$9.8^{+0.3}_{-0.9}\times10^{5}$	$131.5^{+19.8}_{-16.4}$	$101.5^{+12.4}_{-10.5}$	$145.6^{+11.1}_{-10.5}$	$119.7^{+9.9}_{-8.7}$
AGAL345.003−00.224	0.452	0.594	1.04±0.01	1.3×10^{14}	2.0×10^{14}	$1.1^{+0.1}_{-0.1}\times10^{6}$	$105.3^{+7.5}_{-6.6}$	$83.0^{+5.5}_{-5.0}$	$102.8^{+4.1}_{-3.5}$	$86.5^{+2.5}_{-2.4}$
AGAL345.488+00.314	0.586	0.714	0.98±0.01	6.5×10^{13}	1.2×10^{14}	$1.1^{+0.1}_{-0.1}\times10^{6}$	$86.5^{+5.7}_{-5.3}$	$71.1^{+4.5}_{-4.2}$	$79.6^{+2.2}_{-2.8}$	$66.6^{+1.7}_{-1.6}$
AGAL345.504+00.347	0.524	0.661	1.17±0.02	8.3×10^{13}	1.0×10^{14}	$1.2^{+0.1}_{-0.1}\times10^{6}$	$120.3^{+8.9}_{-8.1}$	$93.3^{+8.5}_{-7.3}$	$143.8^{+7.2}_{-6.9}$	$120.9^{+5.9}_{-5.5}$
AGAL345.718+00.817	0.626	0.748	0.89±0.04	9.0×10^{12}	1.9×10^{13}	$1.7^{+0.3}_{-0.2}\times10^{6}$	$58.3^{+14.8}_{-12.0}$	$49.4^{+11.8}_{-9.5}$	$48.0^{+5.2}_{-4.9}$	$40.6^{+3.5}_{-3.3}$
AGAL351.131+00.771	0.556	0.689	0.37±0.05	...	...	...	...	...	...	...
AGAL351.161+00.697	0.524	0.661	1.09±0.01	1.5×10^{14}	2.5×10^{14}	$1.3^{+0.1}_{-0.1}\times10^{6}$	$113.8^{+8.6}_{-8.0}$	$97.4^{+4.3}_{-4.0}$	$101.9^{+2.1}_{-1.9}$	$91.4^{+1.5}_{-1.4}$
AGAL351.244+00.669	0.650	0.767	0.89±0.01	6.0×10^{13}	1.3×10^{14}	$9.2^{+1.1}_{-1.6}\times10^{5}$	$95.0^{+4.5}_{-4.5}$	$82.0^{+3.7}_{-3.5}$	$81.4^{+3.1}_{-1.1}$	$69.3^{+1.5}_{-1.5}$
AGAL351.571+00.762	0.683	0.792	0.48±0.11	...	...	...	...	...	...	...
AGAL351.581−00.352	0.452	0.594	2.29±0.07	...	...	...	>300	>300	>300	>300
AGAL351.774−00.537	0.433	0.575	1.47±0.02	6.1×10^{14}	7.1×10^{14}	$1.9^{+0.1}_{-0.2}\times10^{6}$	>300	$291.2^{+33.5}_{-27.7}$	>300	354.7
AGAL353.066+00.452	0.489	0.629	0.65±0.11	...	...	...	...	...	...	...
AGAL353.409−00.361	0.600	0.726	1.04±0.01	5.3×10^{13}	9.1×10^{13}	$1.5^{+0.2}_{-0.2}\times10^{6}$	$116.7^{+8.1}_{-7.4}$	$92.3^{+5.7}_{-5.2}$	$79.0^{+2.3}_{-2.3}$	$65.4^{+1.3}_{-1.3}$
AGAL353.417−00.079	0.626	0.748	...	...	...	...	...	...	...	...
AGAL354.944−00.537	0.600	0.726	0.60±0.09	...	...	...	...	...	...	...

Table A.7. H_2CO luminosities.

Sources	$L'_{H_2CO\ 3_{13}-2_{12}}$ K km s^{-1} pc^2	$L'_{H_2CO\ 3_{12}-2_{11}}$ K km s^{-1} pc^2	$L'_{H_2CO\ 3_{03}-2_{02}}$ K km s^{-1} pc^2	$L'_{H_2CO\ 3_{22}-2_{21}}$ K km s^{-1} pc^2	$L'_{H_2CO\ 3_{21}-2_{20}}$ K km s^{-1} pc^2	$L'_{H_2CO\ 4_{04}-3_{03}}$ K km s^{-1} pc^2	$L'_{H_2CO\ 4_{23}-3_{22}}$ K km s^{-1} pc^2	$L'_{H_2CO\ 4_{22}-3_{21}}$ K km s^{-1} pc^2
AGAL008.684−00.367	12.25	8.66	5.00	0.83	0.99	5.34	1.53	1.49
AGAL008.706−00.414	2.88	1.76	0.87	...	1.08	1.09	...	...
AGAL010.444−00.017	5.50	4.70	...	...	...	3.99	...	...
AGAL010.472+00.027	77.46	57.14	30.42	13.97	14.28	47.82	39.42	34.64
AGAL010.624−00.384	51.03	48.37	25.01	7.30	8.58	37.53	17.66	17.48
AGAL012.804−00.199	8.17	7.90	4.09	1.20	1.18	5.41	2.24	2.27
AGAL013.178+00.059	3.27	2.89	1.58	0.39	0.55	1.76	0.54	0.55
AGAL013.658−00.599	5.19	5.94	3.15	...	...	3.11	1.43	1.21
AGAL014.114−00.574	2.51	1.95	1.23	0.13	0.29	1.39	0.30	0.33
AGAL014.194−00.194	9.41	6.34	3.63	0.77	0.84	3.12	1.05	1.09
AGAL014.492−00.139	2.01	0.92	1.31	...	...	1.13	...	...
AGAL014.632−00.577	0.84	0.78	0.73	0.15	0.23	1.09	0.29	0.27
AGAL015.029−00.669	8.75	7.23	4.27	1.08	1.17	3.88	1.14	1.19
AGAL018.606−00.074	3.09	2.63	1.54	...	...	2.03	0.62	0.66
AGAL018.734−00.226	62.31	50.81	37.54	6.72	6.24	32.90	11.37	10.52
AGAL018.888−00.474	10.36	8.07	6.27	1.17	0.99	5.16	1.41	1.64
AGAL019.882−00.534	9.80	8.45	6.02	1.46	1.71	7.55	2.91	2.88
AGAL022.376+00.447	2.15	2.19	1.46	...	...	1.54	0.51	0.57
AGAL023.206−00.377	8.47	8.57	5.29	1.44	1.89	9.61	4.74	4.31
AGAL024.629+00.172	3.68	3.44	1.72	...	...	3.25	...	0.52
AGAL028.564−00.236	4.81	3.49	1.12	...	...	2.42	...	...
AGAL028.861+00.066	...	...	...	...	...	10.17	3.94	3.92
AGAL030.848−00.081	4.38	3.30	1.93	...	...	1.84	...	0.44
AGAL030.893+00.139	1.67	1.12	0.79	...	...	0.81	...	...
AGAL031.412+00.307	5.57	6.88	5.64	3.37	3.68	11.06	8.52	7.31
AGAL034.258+00.154	3.50	3.24	2.24	0.81	0.89	3.22	2.31	1.92
AGAL034.401+00.226	2.27	2.10	1.37	0.33	0.27	1.47	0.46	0.48
AGAL034.411+00.234	1.79	1.55	1.05	0.30	0.22	1.08	0.52	0.47
AGAL034.821+00.351	0.85	0.51	0.35	...	...	0.25	0.04	0.05
AGAL035.197−00.742	3.91	3.27	3.16	0.94	1.02	3.18	1.42	1.28
AGAL037.554+00.201	11.83	8.56	5.93	0.91	1.67	7.08	2.68	2.84
AGAL043.166+00.011	276.67	237.07	96.28	35.86	39.06	177.78	101.37	98.14
AGAL049.489−00.389	90.22	81.06	55.34	24.08	21.85	65.70	41.75	36.75
AGAL053.141+00.069	1.85	1.56	1.04	0.29	0.29	1.06	0.35	0.38
AGAL059.782+00.066	...	...	...	...	...	1.03	0.36	0.35
AGAL305.192−00.006	4.79	4.00	2.58	0.55	0.47	2.33	0.75	0.71
AGAL305.209+00.206	20.78	18.56	10.96	3.53	3.10	12.58	5.74	5.28
AGAL305.562+00.014	6.52	5.50	3.49	0.79	0.78	3.27	0.90	0.92
AGAL305.794−00.096	1.13	0.73	0.48	...	...	0.41	...	...
AGAL309.384−00.134	13.52	13.41	7.14	1.96	1.66	5.44	1.63	1.89
AGAL310.014+00.387	3.75	3.51	2.03	0.62	0.53	1.98	0.69	0.76
AGAL313.576+00.324	...	...	...	...	...	2.56	0.83	0.93
AGAL316.641−00.087	...	...	...	...	...	0.10	0.05	0.06
AGAL317.867−00.151	3.91	3.15	2.41	0.64	0.59	2.09	0.67	0.71
AGAL318.779−00.137	1.76	1.28	0.99	0.39	0.26	1.18	0.33	0.45
AGAL320.881−00.397	11.30	6.05	5.86	...	...	3.26	...	...
AGAL326.661+00.519	1.33	0.98	0.64	0.17	0.12	0.44	0.10	0.09
AGAL326.987−00.032	4.32	3.72	2.77	0.24	0.54	2.51	0.89	0.88
AGAL327.119+00.509	6.05	4.59	3.37	...	...	3.18	2.10	1.59
AGAL327.293−00.579	13.34	11.87	4.75	4.52	4.13	5.63	8.62	7.44
AGAL327.393+00.199	20.35	15.65	8.74	1.72	1.91	6.93	1.97	1.98
AGAL328.809+00.632	17.32	15.82	11.30	4.28	4.31	15.18	7.38	7.17
AGAL329.029−00.206	126.78	104.02	80.10	26.68	23.11	59.62	22.63	19.24
AGAL329.066−00.307	83.37	64.99	48.82	11.39	9.80	37.93	8.98	9.48
AGAL330.879−00.367	18.33	16.56	11.23	4.40	3.75	11.98	7.92	7.13
AGAL330.954−00.182	129.18	118.30	80.98	33.77	31.43	91.05	56.54	53.88
AGAL331.709+00.582	69.33	60.38	39.69	10.74	7.28	31.35	10.01	9.77
AGAL332.094−00.421	4.11	2.86	2.01	0.52	0.52	1.94	0.81	0.66

Table A.7. continued.

Sources	$L'_{H_2CO\ 3_{13}-2_{12}}$ K km s^{-1} pc^2	$L'_{H_2CO\ 3_{12}-2_{11}}$ K km s^{-1} pc^2	$L'_{H_2CO\ 3_{03}-2_{02}}$ K km s^{-1} pc^2	$L'_{H_2CO\ 3_{22}-2_{21}}$ K km s^{-1} pc^2	$L'_{H_2CO\ 3_{21}-2_{20}}$ K km s^{-1} pc^2	$L'_{H_2CO\ 4_{04}-3_{03}}$ K km s^{-1} pc^2	$L'_{H_2CO\ 4_{23}-3_{22}}$ K km s^{-1} pc^2	$L'_{H_2CO\ 4_{22}-3_{21}}$ K km s^{-1} pc^2
AGAL332.826−00.549	14.54	12.76	8.59	3.10	3.19	9.91	5.37	4.87
AGAL333.134−00.431	28.42	24.99	15.60	4.93	4.62	13.22	5.81	5.32
AGAL333.284−00.387	10.24	7.99	5.17	1.37	1.37	4.59	1.34	1.38
AGAL333.314+00.106	5.76	4.63	3.14	0.64	0.61	2.42	0.61	0.66
AGAL333.604−00.212	22.20	17.83	9.90	3.16	2.86	8.29	3.78	3.46
AGAL333.656+00.059	3.00	2.11	1.75	...	...	1.40	...	...
AGAL335.789+00.174	11.03	9.22	6.43	1.92	1.45	6.09	2.25	2.02
AGAL336.958−00.224	21.63	17.68	10.31	...	...	8.99	3.64	3.02
AGAL337.176−00.032	31.44	26.52	19.84	...	...	18.65	5.67	4.57
AGAL337.258−00.101	19.33	16.60	11.81	...	...	8.04	3.13	2.03
AGAL337.286+00.007	...	...	...	...	...	1.94	...	...
AGAL337.406−00.402	15.42	13.47	10.00	3.43	3.36	12.54	7.14	6.57
AGAL337.704−00.054	105.09	85.46	65.70	19.53	16.22	62.05	32.85	29.53
AGAL337.916−00.477	14.53	12.77	9.84	3.97	3.58	11.11	6.21	6.10
AGAL338.066+00.044	...	1.45	1.31	...	...	1.11	...	...
AGAL338.786+00.476	4.10	2.93	2.18	...	...	1.69	...	0.34
AGAL338.926+00.554	38.97	38.58	24.08	7.70	6.98	22.36	7.40	7.32
AGAL339.623−00.122	4.19	3.36	2.17	...	...	1.82	0.69	0.63
AGAL340.374−00.391	2.57	1.84	1.43	...	...	1.40	0.51	0.47
AGAL340.746−01.001	2.53	2.02	1.84	0.43	0.34	1.32	0.30	0.35
AGAL340.784−00.097	21.65	16.64	12.01	...	...	11.80	6.16	4.36
AGAL341.217−00.212	5.80	5.30	3.78	1.04	0.82	3.74	1.29	1.20
AGAL342.484+00.182	36.82	32.67	22.13	4.16	4.45	25.57	8.36	8.58
AGAL343.128−00.062	9.45	8.58	6.22	2.18	2.15	7.66	3.89	3.86
AGAL343.756−00.164	4.43	4.93	3.26	1.05	1.05	3.80	1.54	1.56
AGAL344.227−00.569	1.67	1.43	2.55	0.89	0.76	2.77	1.48	1.40
AGAL345.003−00.224	10.69	9.52	7.08	2.23	2.06	7.34	3.58	3.19
AGAL345.488+00.314	6.25	5.21	3.88	1.11	1.29	3.80	1.45	1.40
AGAL345.504+00.347	4.11	3.66	2.90	0.97	0.87	3.39	2.13	1.72
AGAL345.718+00.817	0.67	0.56	0.42	0.09	0.09	0.37	0.07	0.09
AGAL351.131+00.771	0.25	0.17	0.19	...	...	0.07	...	...
AGAL351.161+00.697	6.33	5.38	3.78	1.30	1.17	4.12	1.97	1.84
AGAL351.244+00.669	5.97	4.73	3.26	1.02	0.97	2.91	1.09	1.10
AGAL351.571+00.762	0.15	0.12	0.07	...	...	0.03	...	...
AGAL351.581−00.352	18.55	16.75	15.90	12.90	11.91	36.43	28.39	24.95
AGAL351.774−00.537	2.39	2.25	1.63	0.77	0.79	2.39	1.76	1.57
AGAL353.066+00.452	0.07	0.04	0.03	...	...	0.02	...	...
AGAL353.409−00.361	13.94	11.52	8.76	2.92	2.59	9.10	3.26	3.31
AGAL353.417−00.079	...	0.61	0.39	...	...	...	...	...
AGAL354.944−00.537	0.32	0.22	0.21	...	...	0.13	...	...